

Pre-equilibrium helion emission induced by protons

Jacques Bezuidenhout



**Dissertation presented for the degree of Doctor of Philosophy
at Stellenbosch University**

Promoter: *Prof A A Cowley*

December 2006

Declaration:

I, the undersigned, hereby declare that the work contained in this dissertations is my own work and that I have not previously in its entirety or in part submitted it at university for a degree.

Signature:

Date:

III

ABSTRACT**Pre-equilibrium helion emission induced by protons**

This thesis is devoted to a study of the $^{93}\text{Nb}(\bar{p}, ^3\text{He})$ and $^{59}\text{Co}(\bar{p}, ^3\text{He})$ reactions at incident energies of 100 MeV, 130 MeV and 160 MeV. Double differential cross sections and analysing power distributions were measured from a threshold of ~ 30 MeV up to the kinematic maximum and at scattering angles between 15° and 120° . The experimental data were compared with theoretical calculations done by combining a statistical multistep theory with a deuteron pickup mechanism in the final stage. The contribution of the first three steps towards the total double differential cross section and analysing power was assessed.

The theory described the experimental double differential cross section and analysing power data reasonably well over all incident and scattered energies and for both target nuclei. As the incident energy was increased, the characteristics of the reaction mechanism also remained consistent. Thus the results supported the underlying multistep-pickup theory. The two target nuclei demonstrated similar responses, suggesting these two share the same basic reaction mechanism.

The total double differential cross section for the reaction dropped with an increase in incident energy. At a fixed emission energy, near the maximum allowed value, the slope of the double differential cross section increased with an increase in incident energy, resulting in the dominance of forward peaked reactions at higher incident energies.

The sensitivity of analysing power to the multistep part of the reaction was valuable to the study. Forward-peaked contributions that were associated with single step direct reactions resulted in large analysing power values at small scattering angles, and values dropped to around zero at large angles. The analysing power also appeared to decrease to values approximating zero as the incident energy was increased to 160 MeV. Furthermore, this study also confirmed the dominance of higher step mechanisms at high excitation energies, irrespective of incident energy. In general the results were in agreement with the predicted properties of the assumed reaction mechanism at all incident and emission energies, which inspires confidence that the theoretical interpretation is likely to be correct.

OPSOMMING

Helion-emissie na voorewewigsreaksies met protone

Die werk in hierdie tesis behels 'n studie van die $^{93}\text{Nb}(\bar{p}, {}^3\text{He})$ en $^{59}\text{Co}(\bar{p}, {}^3\text{He})$ reaksies by invalsendigheite van 100 MeV, 130 MeV en 160 MeV. Dubbele differensiële kansvlakke en analiseervermoë is gemeet vanaf 'n drumpel van ~ 30 MeV tot by die kinematiese maksimum en by verstrooiingshoeke tussen 15° en 120° . Die eksperimentele data is vergelyk met die resultate van teoretiese berekeninge gegrond op 'n statistiese multistap teorie met 'n deutron optelreaksie tydens die finale stap. Bydraes van die eerste drie stappe tot die totale differensiële kansvlakke en analiseervermoë is in berekening gebring.

Vir beide die skyfkerne beskryf die teorie die gemete dubbele differensiële kansvlakke en analiseervermoë data redelik goed oor die volle gebied van beide invalsendigheite en ejetielenergieë. Dit bevestig dat, namate die invalsendigheite toeneem, die reaksiemeganisme steeds beskryf word deur 'n multistap optelreaksie. Verder word dit waargeneem vir beide skyfkerne wat bevestig dat die reaksiemeganisme vir albei kerne dieselfde is.

Die totale dubbele differensiële kansvlak van die reaksie neem af namate die invalsendigheite toeneem. By 'n arbitrêre ejetielenergie, gekies naby die maksimum, neem die helling van die dubbele differensiële kansvlakke toe met toename in die invalsendigheite. Dit dui op 'n toenemend voorwaarts gerigte reaksie-opbrengs by hoër invalsendigheite.

Die gevoeligheid van die analiseervermoë vir die aantal stappe in die reaksie was waardevol in hierdie studie. Voorwaarts gerigte opbrengste te assosieer met enkelstap direkte reaksies is in ooreenstemming met die groot waargenome waardes vir die analiseervermoë by klein verstrooiingshoeke, wat daarna na nul daal by groter hoeke. Namate die invalsendigheite toeneem tot 160 MeV, daal die analiseervermoë na nul. Verder bevestig die studie ook die oorheersing van die bydraes van die hoër orde stappe by hoër opwekkingsenergieë, ongeag die invalsendigheite. Oor die algemeen vergelyk die gemete resultate goed met die voorspelde eienskappe vir die gekose reaksiemeganisme by alle invalsendigheite en ejetielenergieë. Dit ondersteun die aanname dat die gekose teoretiese beskrywing van die reaksie inderdaad korrek is.

ACKNOWLEDGEMENTS

- My sincere gratitude goes towards the following people and institutions that contributed towards the success of this study:

- My supervisor, **Professor Anthony Cowley**, for his enthusiasm and the outstanding way in which he guided me in this field of study.

- The staff of iThemba LABS, in particular **Dr Siegfried Förtsch, Dr Retief Neveling and Dr Deon Steyn**, for their valuable support in conducting the experiment successfully.

- The members of Nuclear Physics Group of Stellenbosch University, especially **Professor Greg Hillhouse, Dr Brandon van der Ventel, Dr Anton Stander and JJ van Zyl**, for numerous discussions, presentations and general support during the last few years.

- The staff of the **Military Academy** for logistic support and my colleagues in the Physics Department specifically for allowing me the time to complete this study.

- Last but surely not least to my family **Melinda, Nicola, Jané and Jannich** for the encouragement, love and understanding during times that I could not pay full attention to them.

JOB 38

Daarna het die Here Job uit 'n storm geantwoord en gesê:

Kan jy die bande van die Sewe-ster knoop?

Of die toue van die Oríon losmaak?

Ken jy die wette van die hemel?

Toe het Job die Here geantwoord en gesê:

Kyk, ek is te gering. Wat kan ek U antwoord?

CONTENTS

<i>Chapter 1: INTRODUCTION.....</i>	<i>1</i>
<i>1.1 Historical Background.....</i>	<i>1</i>
<i>1.2 Pre-equilibrium Reactions.....</i>	<i>2</i>
<i>1.3 Emission of Composite Particles.....</i>	<i>2</i>
<i>1.4 The Aims of this Study.....</i>	<i>4</i>
<i>1.5 Overview of this study.....</i>	<i>4</i>
<i>Chapter 2: THEORETICAL BACKGROUND.....</i>	<i>6</i>
<i>2.1 Overview.....</i>	<i>6</i>
<i>2.2 The Distorted Wave Born Approximation.....</i>	<i>7</i>
<i>2.3 Statistical Multistep Theory.....</i>	<i>14</i>
<i>2.4 Polarisation and Analysing Power.....</i>	<i>17</i>
<i>2.5 Double Folding Model.....</i>	<i>20</i>
<i>Chapter 3: THE EXPERIMENT.....</i>	<i>24</i>
<i>3.1 Overview.....</i>	<i>24</i>
<i>3.2 Facility.....</i>	<i>24</i>
<i>3.3 Proton Beam.....</i>	<i>25</i>
<i>3.4 Scattering Chamber.....</i>	<i>26</i>
<i>3.5 Targets.....</i>	<i>29</i>
<i>3.6 Detector Telescopes.....</i>	<i>30</i>
<i>3.7 Electronics.....</i>	<i>33</i>
<i>3.8 Data Handling.....</i>	<i>38</i>
<i>3.9 Experimental Procedure.....</i>	<i>38</i>

VIII

Chapter 4: FINAL DATA ANALYSIS.....	40
4.1 Overview.....	40
4.2 Energy Calibrations.....	40
4.3 Particle Identification.....	44
4.4 Projection Spectra.....	46
4.5 Experimental Data Corrections	47
4.6 Double Differential Cross Section.....	49
4.7 Analysing Power.....	51
4.8 Systematic Errors.....	54
Chapter 5: THEORETICAL CALCULATIONS.....	57
5.1 Overview.....	57
5.2 Multistep Reaction Pickup Codes.....	57
5.3 Intermediate Double Differential Cross Values.....	60
5.4 Optical Model Parameter Sets.....	63
5.5 Density Distributions.....	65
Chapter 6: RESULTS.....	67
6.1 Overview.....	67
6.2 Phenomenological Parameterisation of Kalbach.....	67
6.3 Double Differential Cross Section and Analysing Power in terms of Multistep Theory.....	74
6.4 Features of the Double Differential Cross Section Angular Distributions.....	81
6.5 Characteristics of the Analysing Power Distributions.....	88
6.6 Summary of Results.....	97

<i>Chapter 7: SUMMARY AND CONCLUSIONS.....</i>	<i>98</i>
<i>APPENDIX A.....</i>	<i>100</i>
<i>REFERENCES.....</i>	<i>122</i>

Chapter 1: INTRODUCTION

1.1 Historical Background

When Henri Becquerel discovered radioactivity in 1896, he introduced the world to the field of nuclear physics. Soon afterwards scientists started to observe particles which were emitted by the nucleus. One of the most famous pioneers was Rutherford. He showed in 1909 that an alpha particle is nothing else than a helium nucleus, one of the most stable nuclear configurations. Based on a scattering experiment he also formulated the nuclear atomic model, by showing that the atom contained a nucleus with positive charge which carries almost all the mass of the atom. Investigations of nuclear reactions followed in which the nucleus is excited and the emitted products are observed.

Experiments exploring nuclear interactions that are induced by a beam of high energy particles are very popular. A proton beam is often employed because of the ease of proton production, polarisation and acceleration. Various nuclear reactions, mainly determined by the energy of the incident beam, can take place. At low incident energies the Coulomb force of the positive charged protons in the nucleus will repel low energy protons colliding with a nucleus elastically. An expression for the angular distribution of these elastically scattered particles was derived by Rutherford. If the energy of the incident proton is increased further it can overcome the Coulomb barrier and enter the nucleus to form a compound nucleus in an excited state. After reaching a statistical equilibrium, the nucleus can then decay by emitting particles. After formation of a compound nucleus in statistical equilibrium the reaction would have lost its memory of the incident particle and therefore the angular distribution of the ejectiles would be fairly isotropic.

If the energy of the incident proton is increased still further, the formation of a compound nucleus becomes less and less probable. Then the direct reaction mechanism becomes possible and eventually it will dominate the reaction. With direct nuclear reactions the dynamics of the incident proton will be reflected in those of the reaction products as no statistical equilibrium is reached by the compound system. Furthermore, by using a polarised incident proton beam an observable called the analysing power can be exploited to provide additional information on the interaction during the nuclear reaction.

1.2 Pre-equilibrium Reactions

It is possible for reactions to take place at a later time after the direct stage, but before statistical equilibrium is reached. This is known as the pre-equilibrium reaction mechanism. It is reasonable to assume that the pre-equilibrium reactions take place in a number of successive steps and that the reaction steps terminate when either a particle is emitted or statistical equilibrium is reached. The pre-equilibrium nuclear reactions can be divided into two subsets, namely multistep compound reaction (MSC) and multistep direct reactions (MSD). In the MSD reaction the incident particle stays in the continuum until an emission takes place and in the MSC reaction the incident particle becomes part of the nucleus by dropping lower than the separation energy. The higher-step reactions in the multistep chain would also tend to lose memory of the information of the incident particles. Measuring spin observables like analysing power will thus give an indication of the number of steps of the reaction. The more steps that are involved in the reaction, the more isotropic the angular distribution of the ejectiles will be. Naturally there is also a relationship between excitation energy of the nucleus and the number of steps in the reaction.

There are various models that describe MSD reactions, including the so-called Feshbach-Kerman-Koonin (FKK) [Fes80], Tamura-Udagawa-Lenske (TUL) [Tam82] and Nishioka-Yoshida-Weidenmüller (NYW) [Nis88] models. Koning and Akkermans [Kon93] showed that the theoretical predictions do not differ appreciably between the various quantum MSD models. They concluded that the simplest MSD model (the FKK model) is adequate for the interpretation of experimental data. Computer programs that employ the FKK model are readily available.

1.3 Emission of Composite Particles

A large number of experimental studies have been done on the multistep contributions of pre-equilibrium inclusive (p, p') reactions at incident energies of between 100 MeV and 200 MeV. See for example Förtsch *et al.* [För91], Richter *et al.* [Ric92, Ric94] and Steyn [Ste97]. In these studies the FKK theory was applied successfully. The contribution of the different steps towards the final cross section was also investigated in detail [Ric92]. The FKK theory was subsequently applied to proton induced pre-equilibrium reactions in which

composite particles are emitted. For example the (p, α) reaction at incident energies between 100 MeV and 200 MeV was successfully described by a knockout reaction formalism in combination with the FKK theory [Cow96]. Cowley *et al.* [Cow97] also successfully described the $^{93}\text{Nb}(p, ^3\text{He})$ and $^{59}\text{Co}(p, ^3\text{He})$ reactions at incident energies of 100 MeV, 160 MeV and 200 MeV by employing the FKK theory together with a deuteron pickup model.

Reaction mechanisms can be distinguished in principle by calculating the double differential cross section for each reaction mechanism and comparing it with the experimental data. It is found, however, that the double differential cross sections for the (p, α) reaction [Bon89] corresponding to pickup and knockout mechanisms are very similar. In contrast with the double differential cross section, the analysing power is more sensitive to the reaction mechanism. For instance, the analysing power measurements of the $^{58}\text{Ni}(p, \alpha)$ reaction at incident energies of 72 MeV [Bon89] showed that the reaction could be explained by a knockout and not by a pickup mechanism. This motivated Spasova *et al.* [Spa00] to investigate the analysing power of $(\bar{p}, ^3\text{He})$ reaction with ^{58}Ni , ^{90}Zr and ^{209}Bi as targets and at an incident energy of 72 MeV. Spasova *et al.* found a high sensitivity of the analysing power to the different steps in the multistep reaction and also confirmed that a deuteron pickup mechanism could account for the experimental data. The observed relationship between the analysing power and the number of steps in the reaction makes this observable very useful when the multistep components are investigated. Cowley *et al.* [Cow00] measured analysing powers in the $^{93}\text{Nb}(\bar{p}, ^3\text{He})$ and $^{59}\text{Co}(\bar{p}, ^3\text{He})$ reactions at a higher incident energy of 100 MeV. By means of the analysing power measurements, Cowley *et al.* confirmed the participation of several steps when excitation energies are high and scattering angles are large.

In contrast with experiments up to 100 MeV incident energy that indicate fairly large analysing power values at forward angles and at high emission energies of composite ejectiles, Renshaw *et al.* [Ren91] measured zero analysing power for proton induced reactions on $^{\text{nat}}\text{Ag}$ at 200 MeV at comparable kinematic conditions. This results in an incident energy range between 100 MeV and 200 MeV where the analysing power for the $(\bar{p}, ^3\text{He})$ reaction needs to be investigated further. One would thus expect the analysing power to fade away as the incident energy is increased, up to a point where it disappears

entirely at 200 MeV, irrespective of angle or emission energy. This study extends the research through additional data on the $^{93}\text{Nb}(\bar{p}, ^3\text{He})$ and $^{59}\text{Co}(\bar{p}, ^3\text{He})$ reactions at higher incident energies (130 MeV and 160 MeV) and investigates the new data together with previous experimental data at an incident energy of 100 MeV.

1.4 The Aims of this Study

The aim of this study is to investigate the energy dependence of the inclusive $(\bar{p}, ^3\text{He})$ reaction between 100 MeV and 160 MeV by comparing the experimental cross section and the analysing power distributions with the statistical multistep theory of FKK for composite-particle emission; especially at higher energies. The emphasis will therefore be placed on the multistep reaction that precedes a pickup mechanism to form a composite emitted particle.

The theoretical model in the present work is restricted to a pickup mechanism as this is expected to be not only the simplest model, but also a very reasonable formulation. No attempt is made to explore alternative mechanisms, such as knockout. As will be seen, the assumed model is very successful, which is a result that does not strongly motivate a compelling need to explore alternative mechanisms.

Two naturally occurring pure isotopes (^{93}Nb and ^{59}Co) were selected as target nuclei. These two isotopes were assumed to be representative examples of nuclei in general, and there is no strong reason to assume that the qualitative details of emission of composite particles depend on the nuclear mass of the target.

1.5 Overview of this study

In this study experimental double differential cross section and analysing power data were obtained for the $(\bar{p}, ^3\text{He})$ reaction at incident energies of 130 MeV and 160 MeV. Published experimental data for the $^{93}\text{Nb}(\bar{p}, ^3\text{He})$ and $^{59}\text{Co}(\bar{p}, ^3\text{He})$ reactions at 100 MeV were already available, therefore for comparison the same two targets were selected for this experiment. Data were acquired at angles of 15° , 20° , 25° , 30° , 35° , 40° , 50° , 60° , 80° , 100° and 120° for emission energies above 30 MeV up to the kinematic limit.

Theoretical predictions of double differential cross section and analysing power distributions over the entire range of emission energies and scattering angles were compared with experimental data. The distorted wave Born approximation (DWBA) theory [Sat83, Gle83, Sen83] of direct nuclear reactions was used for the calculation of the pickup component following a multistep nucleon-nucleon intranucleon interaction. Double differential cross section and analysing power calculations were done for the first three steps of the multistep reaction by utilising the Feshbach, Kerman and Koonin [Fes80] statistical multistep formalism. This enabled the investigation of the contributions of the different steps toward the final observed emitted ^3He particle. Various computer programs were employed to perform the theoretical calculations. The DWBA calculations for a pickup reaction were performed with the DWUCK4 computer code of Kunz and Rost [Kun93]. In this DWBA calculation the double folding model was used to determine the potential between the residual nucleus and the emitted helion. For this double folding potential the computer code of Katsuma and Sakuragi [Kat98] was used. The computer codes were incorporated in the pickup multistep code of Dimitrova [Dim96] and Demetriou [Dem96] to produce the theoretical double differential cross section and analysing power for the (\bar{p} , ^3He) reaction.

The layout of the thesis is as follows: Chapter 2 describes the theoretical models that underlie this study. In chapter 3 the experimental set-up at the iThemba LABS facility and the procedure that was needed to execute the experiment are explained. In chapter 4 all the processes that were followed to perform data reductions and energy calibrations are discussed. Chapter 5 elaborates on the methods and computer programs used to do the theoretical calculations. Results are presented and discussed in chapter 6. Finally chapter 7 gives a summary and conclusion of the study.

Chapter 2: THEORETICAL BACKGROUND

2.1 Overview

In this chapter all the theoretical models that underlie this study are discussed. As was mentioned before, the focus was on the proton multistep processes and the consequent pickup of a deuteron by a proton to form an ejectile. The reaction of interest can be symbolically expressed as follows



Multistep processes refer to a number of intranuclear proton-nucleon collisions that take place before the deuteron is picked up to form a helion. The multistep reaction diagram in *figure 2.1* is a schematic representation of one, two and three step processes.

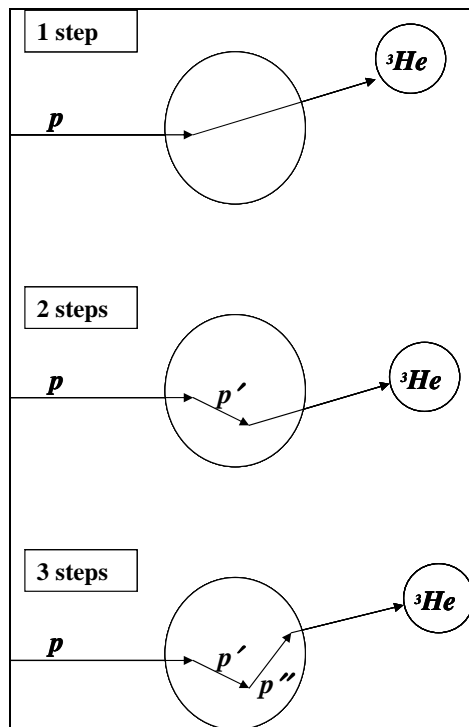


Figure 2.1: Illustration of multistep reactions.

In the first section of this chapter the formalism for the Distorted Wave Born Approximation (DWBA) model is discussed. The following section gives an overview of the statistical multistep theory of Feshbach, Kerman and Koonin (FKK). In section 2.4 the relationship between polarisation of the incident beam and analysing power are investigated. Lastly the

double folding model that was used to generate the optical potential of the exit channel is discussed.

2.2 The Distorted Wave Born Approximation

The Distorted Wave Born Approximation (DWBA) assumes that elastic scattering is the most important process in nuclear reactions and nonelastic scattering can be described as a perturbation. The original model which was developed to describe direct nuclear reactions used a plane wave approach where the motion of the incident and outgoing particles were described by plane waves. This plane wave approach implies that elastic scattering is also assumed to be small. Cross sections were however regularly overestimated with this model. It was soon realised that distortion needed to be taken into account and in this way cross section angular distribution data could be reproduced more accurately, both in shape and magnitude. The distorted waves were generated by solving the Schrödinger equation with an optical potential which, apart from a real part, also includes an imaginary part that accounts for absorption.

In this study the reaction mechanism for the final formation of the ejectile was chosen to be a pickup. This means that an incident proton, either directly or after a number of collisions, picks up a neutron-proton pair. The result is a helion (^3He) particle that exits. In the theoretical formalism the bound neutron-proton pair can be reduced to a quasi bound deuteron [Sen83]. This simplifies the formalism to a proton picking up a bound deuteron and a helion exiting the nucleus as product. The deuteron pickup reaction is graphically

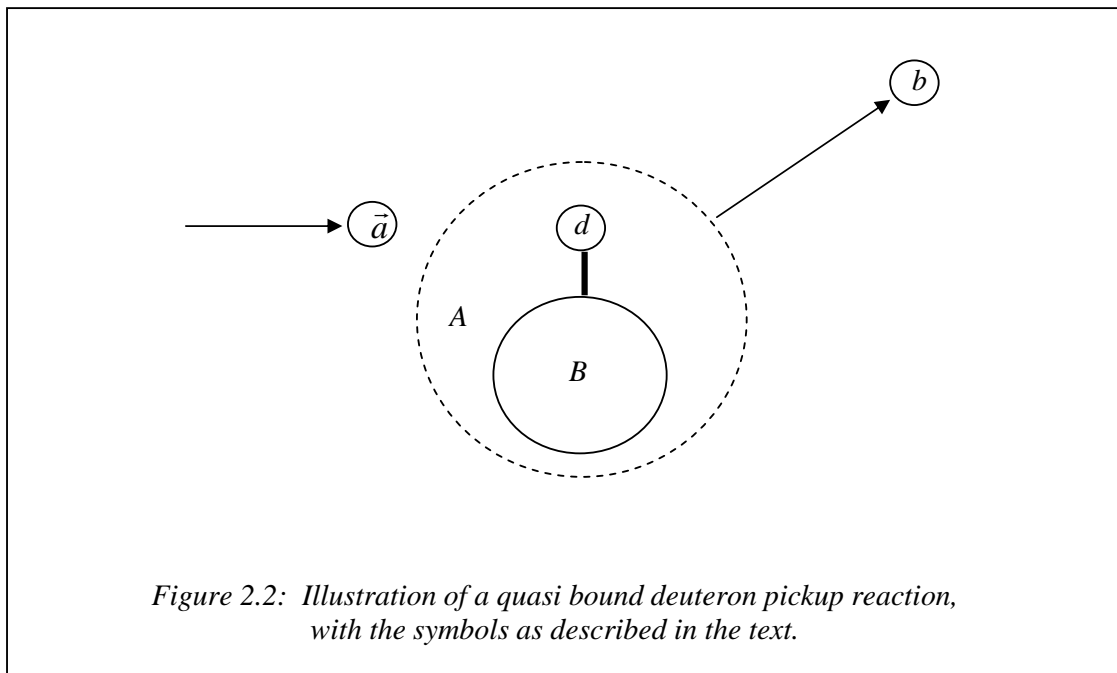
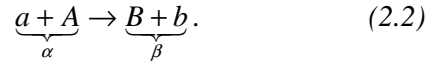


Figure 2.2: Illustration of a quasi bound deuteron pickup reaction, with the symbols as described in the text.

illustrated in *figure 2.2*. In the figure the target nucleus A is indicated as a residual nucleus B plus a quasi bound deuteron d . The incident polarised proton \vec{a} picks up the deuteron forming the exiting helion b .

The formalism used to describe nuclear reactions is to express it in terms of its channels [Sat83, Gle83]. The reaction is treated as a two channel event, a prior (entrance) channel α and the post (exit) channel β , with



The DWBA formalism is based on a transition amplitude or transition matrix between these two channels. This transition amplitude can be expressed as [Sat83]

$$T_{\alpha\beta} = \langle \chi^-(\vec{k}_\beta) \psi_\beta | W | \chi^+(\vec{k}_\alpha) \psi_\alpha \rangle, \quad (2.3)$$

where W is the interacting potential that couples the prior to the post channels. The ψ 's represents internal state wave functions of the two channels and χ^\pm are the distorted waves for the incoming and outgoing waves. The distorted wave can be expressed in terms of the momentum vector \vec{k} and the position vector \vec{r} and is given by [Pea86] as

$$\chi_\beta^+(\vec{k}_\beta, \vec{r}_\beta) = e^{i\vec{k}_\beta \cdot \vec{r}_\beta} + f_\beta^0(\theta) \frac{1}{r_\beta} e^{ik_\beta r_\beta}. \quad (2.4)$$

The distorted wave consists of an incident plane wave and a scattered spherical wave. The function $f_\beta^0(\theta)$ is the scattering amplitude which is caused by an optical potential. The distorted wave function $\chi_\beta^-(\vec{k}_\beta, \vec{r}_\beta)$ has an asymptotic form similar to *equation 2.4*, with incoming spherical waves. $\chi_\beta^-(\vec{k}_\beta, \vec{r}_\beta)$ is a time-reversal of $\chi_\beta^+(\vec{k}_\beta, \vec{r}_\beta)$, thus the following relationship exists [Sat83]

$$\chi_\beta^-(\vec{k}_\beta, \vec{r}_\beta) = \chi_\beta^{+*}(-\vec{k}_\beta, \vec{r}_\beta). \quad (2.5)$$

In practice the distorted waves (*equation 2.4* and *equation 2.5*) can be obtained by solving the Schrödinger equation with a phenomenological complex optical potential. The general form of this optical potential $U(r)$ can be expressed as a sum of the Coulomb potential $U_{Coulomb}$, the central potential $U_{central}$ and the spin-orbit potential $U_{spin-orbit}$ given by

$$\begin{aligned} U(r) &= U_{Coulomb} + U_{central} + U_{spin-orbit} \\ &= U_{Coulomb} + (-U_R - iU_I)_{central} + (U'_R + iU'_I)_{spin-orbit}. \end{aligned} \quad (2.6)$$

The real parts U_R and U'_R of the optical potential describe the elastic scattering channel and imaginary parts U_I and U'_I are included to account for the absorbed part of the flux. The imaginary part U_I does not necessarily have to have the same form as the real part U_R of the potential. The shape of the radial part or the so-called 'form factor' of the optical potential may, for example, be taken as in the Woods-Saxon form given by [Sat83]

$$f(r) = \frac{1}{1 + e^{\left(\frac{r-R}{a}\right)}}, \quad (2.7)$$

where $R = R_0 A^{1/3}$ is the radius of the nucleus.

The total interacting potential W is a combination of the optical potential $U(r)$ and interaction potentials $V(x, \bar{r})$ between nuclei A and B in channels β and α [Gle83, Sat83]. The interaction potential can be expressed as

$$W = V_\alpha - U_\alpha = V_\beta - U_\beta. \quad (2.8)$$

It depends on the internal variables x of nuclei A and B and the separation \bar{r} . The optical potential only depends on the channel radius r .

Rewriting the different functions in the transition matrix provides the following expression

$$T_{\alpha\beta} = \iint d\vec{r}_\beta d\vec{r}_\alpha \chi_\beta^-(\vec{k}_\beta, \vec{r}_\beta)^* (\psi_\beta | W | \psi_\alpha) \chi_\alpha^+(\vec{k}_\alpha, \vec{r}_\alpha). \quad (2.9)$$

This separates the nuclear structure matrix from the distorted wave functions. The nuclear structure is contained in the round brackets and it implies integration, where the integration runs over all nucleon variables besides \vec{r}_α and \vec{r}_β . The transition matrix can also be written as [Sat83]

$$T_{\alpha\beta} = \iint d\vec{r}_\beta d\vec{r}_\alpha \chi_\beta^-(\vec{k}_\beta, \vec{r}_\beta)^* I_{\beta\alpha}(\vec{r}_\beta, \vec{r}_\alpha) \chi_\alpha^+(\vec{k}_\alpha, \vec{r}_\alpha), \quad (2.10)$$

where $I_{\beta\alpha}$ represents the interacting part of the kernel $K_{\beta\alpha}$ that causes the transition from the prior to the post distorted wave states.

The transition amplitude needs to be extended to include the spin of the various elements in the channels. To include the spin, the distorted waves are transformed to matrices in the projections of the nuclear spins by [Sat83]

$$\chi^+ \psi_\alpha \rightarrow \sum \chi_{\alpha', \alpha}^+ \psi_{\alpha'}. \quad (2.11)$$

The transition amplitude then becomes

$$T_{\alpha\beta} = \sum_{\beta'\alpha'} \iint d\vec{r}_\beta d\vec{r}_\alpha \chi_{\beta'\beta}^-(\vec{k}_\beta, \vec{r}_\beta)^* (\psi_{\beta'} | W | \psi_{\alpha'}) \chi_{\alpha'\alpha}^+(\vec{k}_\alpha, \vec{r}_\alpha). \quad (2.12)$$

The transition amplitude can again (similar to *equation 2.10*) be rewritten in terms of the radial parts or form factors and then gives [Sat83]

$$T_{\alpha\beta} = \sum_{\beta'\alpha'} \iint d\vec{r}_\beta d\vec{r}_\alpha \chi_{\beta'\beta}^-(\vec{k}_\beta, \vec{r}_\beta)^* I_{\beta'\alpha'}(\vec{r}_\beta, \vec{r}_\alpha) \chi_{\alpha'\alpha}^+(\vec{k}_\alpha, \vec{r}_\alpha). \quad (2.13)$$

The form factors or radial parts of $I_{\beta'\alpha'}(\vec{r}_\beta, \vec{r}_\alpha)$ remain a six dimensional integral over \vec{r}_α and \vec{r}_β . By taking these vectors as parallel ($\vec{r}_\alpha \parallel \vec{r}_\beta$) or $\vec{r}_\beta = \lambda \vec{r}_\alpha$, the integral reduces to a three dimensional integral. This is called the zero range approximation and results in

$$I_{\beta\alpha}(\vec{r}_\beta, \vec{r}_\alpha) \rightarrow I_{\beta\alpha}^{ZR}(\vec{r}_\beta, \vec{r}_\alpha) = F_{\beta\alpha}(\vec{r}_\alpha) \delta(\vec{r}_\beta - \lambda \vec{r}_\alpha). \quad (2.14)$$

In a more general description, the kernel $I_{\beta'\alpha'}$ would contain all the information on the nuclear structure, angular momentum, parity and even the type of reaction that takes place. If the nuclear spins I and their z-components M are included, the kernel can be written as

$$I_{\beta I_B M_B, I_b M_b; \alpha I_A M_A}(\vec{r}_\beta, \vec{r}_\alpha) = J_{\beta\alpha} \int d\xi \psi_{I_B M_B}(x_B)^* \psi_{I_b M_b}(x_b)^* W \psi_{I_A M_A}(x_A) \psi_{I_a M_a}(x_a). \quad (2.15)$$

The respective wave functions are represented by ψ and the Jacobian $J_{\beta\alpha}$ transforms the internal coordinates (x_β) to $(\xi_\beta, \vec{r}_\alpha)$. The angular momentum transfer during a reaction can be written as

$$\mathbf{I}_B - \mathbf{I}_A = \mathbf{J}_{AB}, \quad \mathbf{I}_b - \mathbf{I}_a = \mathbf{J}_{ab}, \quad \mathbf{J}_{ba} + \mathbf{J}_{BA} = \mathbf{I}, \quad (2.16)$$

where \mathbf{J}_{AB} and \mathbf{J}_{ba} denote the spin transfers. According to Satchler [Sat83] the combination of the wave functions will give

$$\psi_{I_B M_B}(x_B)^* \psi_{I_A M_A}(x_A) = \sum_{J_{BA}} \langle I_B I_A M_B, -M_A | J_{BA} M_{BA} \rangle (-)^{I_A - M_A} \Phi_{I_B I_A J_{BA}}^{M_{BA}}(x_B, x_A)^*, \quad (2.17)$$

with $M_{BA} = M_B - M_A$. A function that corresponds to the resultant angular momentum l can then be given as

$$\Phi_{I_B I_A J_{BA}}^{M_{BA}}(x_B, x_A)^* \Phi_{I_b I_a J_{ba}}^{M_{ba}}(x_b, x_a)^* = \sum_l \langle J_{ba} J_{BA} M_{ba} M_{BA} | l m \rangle \Phi_{(I_b I_a) J_{ba} (I_B I_A) J_{AB}, l}^m(x_\beta, x_\alpha)^*, \quad (2.18)$$

with $m = M_{BA} - M_{ba} = M_B + M_b - M_A - M_a$. By applying *equation 2.18* to the kernel in *equation 2.15* it becomes

$$\begin{aligned}
I_{\beta I_B M_B, I_b M_b; \alpha I_A M_A, I_a M_a}(\vec{r}_\beta, \vec{r}_\alpha) &= \sum_{J_{ba} J_{BA}} \langle I_b I_a M_b, -M_a | J_{ba} M_{ba} \rangle \\
&\times \langle I_B I_A M_B, -M_A | J_{BA} M_{BA} \rangle \langle J_{ba} J_{BA} M_{ba} M_{BA} | lm \rangle \quad (2.19) \\
&\times (-)^{I_A - M_A + I_a - M_a} G_{IJ_{ba} J_{BA}}^m(\vec{r}_\beta, \vec{r}_\alpha),
\end{aligned}$$

where the functions $G_{IJ_{ba} J_{BA}}^m(\vec{r}_\beta, \vec{r}_\alpha)$ are called the multipole components. Applying the zero range form to *equation 2.19* (similar to *equation 2.14*) one obtains

$$G_{IJ_{ba} J_{BA}}^{ZR, m}(\vec{r}_\beta, \vec{r}_\alpha) = f_{IJ_{ba} J_{BA}}^{ZR}(\vec{r}_\alpha) [i^l Y_l^m(\hat{r}_\alpha)]^* \delta(\vec{r}_\beta - \lambda \vec{r}_\alpha), \quad (2.20)$$

where Y_l^m are the conjugates of spherical harmonics. The quantity l also gives the parity change with

$$\pi_{\beta\alpha} = \pi_B \pi_b \pi_A \pi_a = (-)^l. \quad (2.21)$$

In a reaction the intrinsic spin of the incident particles interacts with the angular momentum of the target nucleus. This is known as the spin-orbit interaction or coupling [Pea86]. If the incident beam consists of polarised particles this interaction plays an especially fundamental role in nuclear reactions [Kra88]. This will influence the transition amplitude and a general expression for the transition amplitude with spin-orbit coupling can then be written as [Sat83]

$$\begin{aligned}
T_{M_B M_b M_A M_a}^{DW}(\vec{k}_\beta, \vec{k}_\alpha) &= \sum_{M'_b M'_a} \int d\vec{r}_\beta \int d\vec{r}_\alpha \chi_{M'_b M_b}^-(\vec{k}_\beta, \vec{r}_\beta)^* \\
&\times I_{\beta I_B M_B, I_b M'_b; \alpha I_A M_A, I_a M'_a}(\vec{r}_\beta, \vec{r}_\alpha) \chi_{M'_a M_a}^+(\vec{k}_\alpha, \vec{r}_\alpha), \quad (2.22)
\end{aligned}$$

where the distorted waves become matrices in the space of the spins. With application of *equation 2.19* the transition amplitude now becomes

$$T_{M_B M_b M_A M_a}^{DW}(\vec{k}_\beta, \vec{k}_\alpha) = \sum_{J_{BA}} \langle I_B I_A M_B, -M_A | J_{BA} M_{BA} \rangle (-)^{I_A - M_A} \sum_{J_{ba} l} t_{IJ_{ba} J_{BA}}^{m M_b M_a}(\theta, \phi) \quad (2.23)$$

and the reduced amplitude is given by

$$\begin{aligned}
t_{IJ_{ba} J_{BA}}^{m M_b M_a}(\theta, \phi) &= \sum_{M'_b M'_a} \langle I_b I_a M'_b, -M'_a | J_{ba} M'_{ba} \rangle \langle J_{ba} J_{BA} M'_{ba} M_{BA} | lm' \rangle \\
&\times (-)^{I_a - M'_a} \int d\vec{r}_\beta \int d\vec{r}_\alpha \chi_{M'_b M_b}^-(\vec{k}_\beta, \vec{r}_\beta)^* G_{IJ_{ba} J_{BA}}^{m'}(\vec{r}_\beta, \vec{r}_\alpha) \chi_{M'_a M_a}^+(\vec{k}_\alpha, \vec{r}_\alpha). \quad (2.24)
\end{aligned}$$

The transfer of isospin must also be incorporated. This process is analogous to angular momentum transfer, with the isospin transfer expressed as

$$\mathbf{t} = \mathbf{T}_B - \mathbf{T}_A = \mathbf{T}_b - \mathbf{T}_a. \quad (2.25)$$

The argument follows similarly to the angular momentum and the kernel then turns out to be [Sat83]

$$\begin{aligned}
 I_{\beta I_B M_B, I_b M_b; \alpha I_A M_A, I_a M_a}^{T_B N_B, T_b N_b; T_A N_A, T_a N_a}(\vec{r}_\beta, \vec{r}_\alpha) &= \sum_{tJ_{ba}J_{BA}} \hat{t}^{-1} (-)^{T_A - N_A + T_a - N_a + t - n} \\
 &\times \langle T_B T_A N_B, -N_A | tn \rangle \langle T_b T_a N_b, -N_a | t, -n \rangle \\
 &\times \langle I_B I_A M_B, -M_A | J_{BA} M_{BA} \rangle \langle I_b I_a M_b, -M_a | J_{ba} M_{ba} \rangle \\
 &\times \langle J_{ba} J_{BA} M_{ba} M_{BA} | lm \rangle (-)^{I_A - M_A + I_a - M_a} G_{I_{ba} J_{BA}, t}^{m, n}(\vec{r}_\beta, \vec{r}_\alpha).
 \end{aligned} \tag{2.26}$$

Substituting the kernel into the transition amplitude, *equation 2.23* gives

$$\begin{aligned}
 T_{M_B M_b M_A M_a}^{DW; N_B N_b, N_A N_a}(\vec{k}_\beta, \vec{k}_\alpha) &= \sum_{J_{BA} t} \hat{t}^{-1} \langle T_B T_A N_B, -N_A | tn \rangle \\
 &\times \langle T_b T_a N_b, -N_a | t, -n \rangle (-)^{T_A - N_A + T_a - N_a + t - n} \\
 &\times \langle I_B I_A M_B, -M_A | J_{BA} M_{BA} \rangle (-)^{I_A - M_A} \sum_{J_{ba} t} t_{I_{ba} J_{BA}}^{m M_b M_a}(\theta, \phi),
 \end{aligned} \tag{2.27}$$

where

$$n = N_B - N_A = N_a - N_b \tag{2.28}$$

and with

$$N_i = 1/2(A_i - 2Z_i). \tag{2.29}$$

The reduced amplitude $t_{I_{ba} J_{BA}}^{m M_b M_a}(\theta, \phi)$ is given by *equation 2.24*.

The differential cross section can then be expressed as [Sat83]

$$\frac{d\sigma_{\beta\alpha}}{d\Omega} = \frac{\mu_\alpha \mu_\beta}{(2\pi\hbar^2)^2} \frac{k_\beta}{k_\alpha} \frac{1}{(2I_A + 1)(2I_a + 1)} \sigma_{\beta\alpha}(\theta). \tag{2.30}$$

By applying *equation 2.23* the reduced cross section becomes

$$\sigma_{\beta\alpha}(\theta) = \sum_{J_{BA}} \sigma_{J_{BA}}(\theta), \tag{2.31}$$

where

$$\begin{aligned}
 \sigma_{J_{BA}}(\theta) &= \sum_{m M_b M_a} \left| \sum_{tJ_{ba} t} \langle T_B T_A N_B, -N_A | tn \rangle \langle T_b T_a N_b, -N_a | t, -n \rangle \right. \\
 &\quad \left. \times \hat{t}^{-1} (-)^{T_A - N_A + T_a - N_a + t - n} t_{I_{ba} J_{BA}, t}^{m M_b M_a, n}(\theta, \phi) \right|^2
 \end{aligned} \tag{2.32}$$

with the reduced amplitude given by *equation 2.24*.

It is clear from this formalism that the reduced cross section $\sigma_{\beta\alpha}(\theta)$ can be expressed in the following general form as

$$\sigma_{\beta\alpha}(\theta) = \frac{d\sigma}{d\Omega} = \sum_{LSJT} \sum_M \left| \sum_N G_{NLSJT} B_{NL}^M(\vec{k}_\alpha, \vec{k}_\beta) \right|^2. \quad (2.33)$$

The factor B_{NL}^M contains all the distorted wave amplitudes as well as the detail of the interacting potential. The nuclear structure is determined by the wave functions of the initial and final states and is all contained in the factor G_{NLSJT} . The DWUCK4 code calculates the latter part with

$$\frac{d\sigma}{d\Omega}^{DWUCK} = \sum_M \left| \sum_N G_{NLSJT} B_{NL}^M(\vec{k}_\alpha, \vec{k}_\beta) \right|^2. \quad (2.34)$$

According to Glendenning [Gle65] the differential cross section of two-nucleon pickup reactions can be expressed similarly to *equation 2.30* as

$$\frac{d\sigma}{d\Omega}^{DWBA} = \frac{\mu_\alpha \mu_\beta}{(2\pi\hbar^2)^2} \frac{k_\beta}{k_\alpha} \frac{(2I_b + 1)}{(2I_a + 1)} \Omega_d^2 \sum_{LSJT} \langle T_\beta T_{\beta_z} T T_z | T_\alpha T_{\alpha_z} \rangle^2 b_{ST}^2 \sum_M \left| \sum_N G_{NLSJT} B_{NL}^M(\vec{k}_\alpha, \vec{k}_\beta) \right|^2, \quad (2.35)$$

where b_{ST}^2 is the overlap factor involving the spin-isospin functions of the light nuclei and Ω_d^2 is the overlap between the deuteron and the wave function of the exiting particle. For scattered helions this factor is 1.

Sens and de Meijer [Sen83] derived an expression for the differential cross section where all the possible deuteron states were included which is given by

$$\frac{d\sigma}{d\Omega_{(p, {}^3\text{He})}}^{DWBA} = \aleph \sum_{\{n_k\}} G^2(\{n_k\}) \frac{2I_b + 1}{2I_a + 1} \sum_{S,T=0,1} D_{ST}^2 b_{ST}^2 \langle T_\beta T_{\beta_z} T T_z | T_\alpha T_{\alpha_z} \rangle^2 \sum_M \left| \sum_N G_{NLSJT} B_{NL}^M(\vec{k}_\alpha, \vec{k}_\beta) \right|^2 \quad (2.36)$$

where \aleph is a normalisation constant and $G^2(\{n_k\})$ is the spectroscopic factor for a proton and a neutron to form a deuteron bound state with quantum numbers (N, L, J) , and S and T are the transferred spin and isospin, respectively, with the selection rule $S + T = 1$. The constant b_{ST}^2 is also referred to as the spectroscopic factor for light particles a and b (b_{ST}^2 is $\frac{1}{2}$ for the $(\bar{p}, {}^3\text{He})$ reaction) and D_{ST}^2 arises from the spin-isospin exchange term with D_{10}^2 and D_{01}^2 being 0.3 and 0.72 respectively [Nan74].

The expression for the double differential cross section over a continuum of states with excitation energies E then becomes [Spa00]

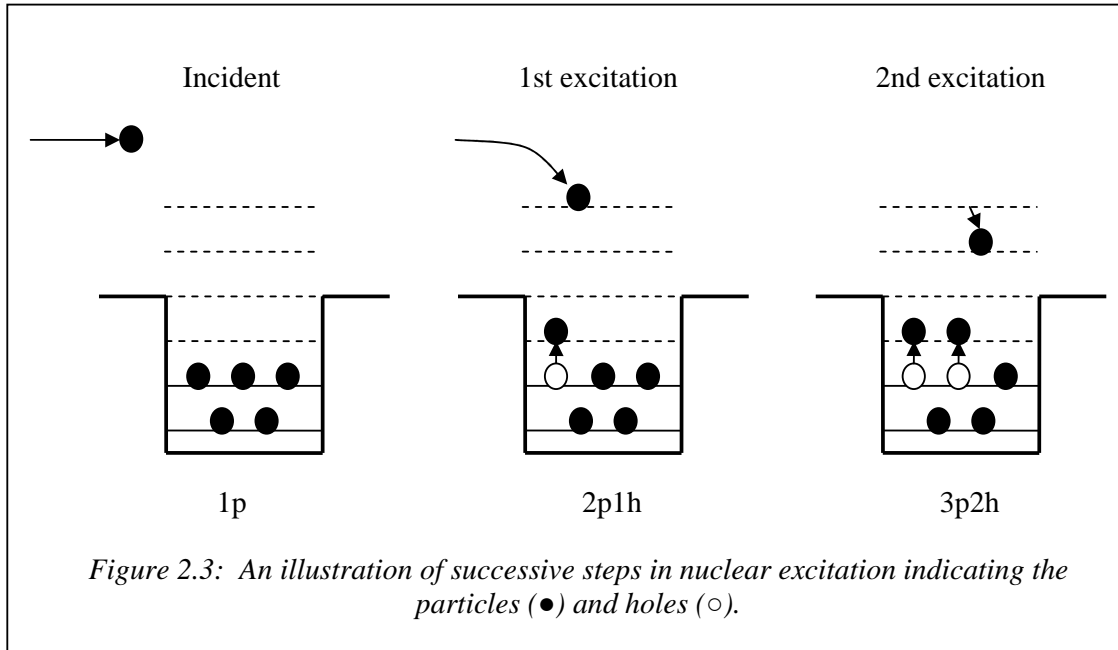
$$\left(\frac{d^2\sigma}{d\Omega dE}\right)^{one-step} = \sum_{N,L,J} \frac{2J+1}{\Delta E} \left(\frac{d\sigma}{d\Omega}\right)^{DWBA} \quad (2.37)$$

where the summation is over the target states with single-particle energies within a small energy window $(E-\Delta E/2, E+\Delta E/2)$.

2.3 Statistical Multistep Theory

Under certain conditions, as explained in the Introduction, depending on the value of the incident energy, nuclear reactions can be described by either the compound nucleus reaction theory or the direct nuclear reaction theory. However there are some nuclear reactions that can not be sufficiently described by either of these two formalisms. Such reactions appear to take place after the direct reaction stage, but before a compound nucleus is formed (in other words before statistical equilibrium is reached by the nucleus). These reactions are referred to as pre-equilibrium reactions, and it is reasonable to assume that these reactions take place in a number of successive steps. The reaction steps are terminated when a nucleon is emitted or statistical equilibrium is reached.

A simple model to understand the pre-equilibrium reactions is the particle-hole concept. The reaction steps of pre-equilibrium reactions are collisions or interactions that take place between the incident particle and the target nucleus and the initial interaction creates a particle-hole pair by exciting one of the nucleons in the target nucleus. This state is known as the 2-particle 1-hole state (2p1h). In the second step another nucleon is excited and a particle-hole pair is formed corresponding to a 3-particle 2-hole state (3p2h). These steps are illustrated in *figure 2.3*.



After any number of steps a nucleon can have enough energy to escape from the nucleus and thus terminate the interaction. Pre-equilibrium reactions can be divided into two categories. The first is the multistep compound reaction which implies that all the nucleons are bound after the initial reaction. The second is the multistep direct reactions which mean that the incident nucleon stays in the continuum. In the multistep reaction shown in *figure 2.3* the nucleon stays in the continuum thus illustrating a multistep direct reaction.

A general expression for the cross section of pre-equilibrium reactions can be written as [Hod97]

$$\sigma_{PEE} = \sigma_c P_1 + \sigma_c \lambda_{12} P_2 + \sigma_c \lambda_{12} \lambda_{23} P_3 + \dots, \quad (2.38)$$

where σ_c is the cross section for the formation of a composite nucleus, P_n is the probability for emission from the n^{th} stage and $\lambda_{n,n+1}$ is the probability for transition from the n^{th} to the $(n+1)^{\text{th}}$ stage.

As was explained in the Introduction, there are a number of equivalent pre-equilibrium statistical multistep formalisms available, and for convenience we chose the theory of Feshbach, Kerman and Koonin (FKK) [Fes80] for the analysis of our experimental data. In the FKK theory the total double differential cross section is the sum of the double differential

cross sections of a single-step and all the other steps in the multistep process [Fes80, Bon81]. In a notation appropriate to the $(p, {}^3\text{He})$ reaction this can be expressed as [Cow91]

$$\left(\frac{d^2\sigma}{dUd\Omega}\right)_{(p, {}^3\text{He})}^{MSD} = \left(\frac{d^2\sigma}{dUd\Omega}\right)_{(p, {}^3\text{He})}^{\text{single-step}} + \left(\frac{d^2\sigma}{dUd\Omega}\right)_{(p, {}^3\text{He})}^{\text{multistep}}, \quad (2.39)$$

where U represents the excitation energy of the residual nucleus. The statistical double differential multistep cross section is then given by

$$\begin{aligned} \left(\frac{d^2\sigma(\bar{k}_f, \bar{k}_i)}{dUd\Omega}\right)_{(p, {}^3\text{He})}^{\text{multistep}} &= \sum_{n=2}^{n_{\max}} \sum_{m=n-1}^{n+1} \int \frac{d\bar{k}_1}{(2\pi)^3} \int \frac{d\bar{k}_2}{(2\pi)^3} \cdots \int \frac{d\bar{k}_n}{(2\pi)^3} \\ &\times \left(\frac{d^2W_{m,n}(\bar{k}_f, \bar{k}_n)}{dU_f d\Omega_f}\right) \times \left(\frac{d^2W_{n,n-1}(\bar{k}_n, \bar{k}_{n-1})}{dU_n d\Omega_n}\right) \times \cdots \\ &\times \left(\frac{d^2W_{2,1}(\bar{k}_2, \bar{k}_1)}{dU_2 d\Omega_2}\right) \times \left(\frac{d^2\sigma(\bar{k}_1, \bar{k}_i)}{dU_1 d\Omega_1}\right)_{(p, p')}^{\text{single-step}}, \end{aligned} \quad (2.40)$$

where $\bar{k}_i, \bar{k}_n, \bar{k}_f$ are the momentum of the initial, n^{th} and final step respectively. The n indicates the reaction step, n_{\max} represents the maximum number of reaction steps and m is the exit mode. In each of the summations the momentum \bar{k}_f of the final step represents the momentum of the emitted helion particle.

The contribution of the first step to the double differential cross section reduces to [Bon81]

$$\left(\frac{d^2\sigma(\bar{k}_1, \bar{k}_i)}{dU_1 d\Omega_1}\right)_{(p, p')}^{\text{single-step}} = \sum_L (2L+1) R_2(L) \rho_2(U) \left\langle \left(\frac{d\sigma}{d\Omega}\right)_{DW} \right\rangle_L, \quad (2.41)$$

where $\left\langle \left(\frac{d\sigma}{d\Omega}\right)_{DW} \right\rangle_L$ is the DWBA differential cross section averaged over all the possible particle-hole states with L angular momentum transfer and $\rho_2(U)$ represents the particle-hole state density after the first collision of the incident proton. A general expression for the spin distribution function $R_N(L)$ of the residual nucleus is given as [Bon81, Cow91]

$$R_N(L) = \frac{2L+1}{\sigma^3 \sqrt{\pi N^3}} \exp\left[-\frac{(L + \frac{1}{2})^2}{N\sigma^2}\right], \quad (2.42)$$

where σ is a spin cut-off parameter and N is a sum of the number of particles p and holes h in the residual nucleus ($N = p + h$).

The differential transition probability to go from stage $(n-1)$ to n is derived through the DWBA as is given by [Bon81, Cow91]

$$\left(\frac{d^2 W_{n,n-1}(\vec{k}_n, \vec{k}_{n-1})}{dU_n d\Omega_n} \right) = 2\pi^2 \rho_c(\vec{k}_n) \rho_N(U_n) \left\langle \left| v_{n,n-1}(\vec{k}_n, \vec{k}_{n-1}) \right|^2 \right\rangle, \quad (2.43)$$

where

$$v_{a,b}(\vec{k}_i, \vec{k}_f) = \int \chi_a^-(r_a) \langle \psi_f | V(\vec{r}_a, \vec{r}_b) | \psi_i \rangle \chi_b^+(\vec{r}_b) d\vec{r}_a d\vec{r}_b. \quad (2.44)$$

The distorted wave functions and interaction optical potential of the matrix element is similar to those in section 2.2. The level density $\rho_N(U_n)$ is the density of particle-hole configurations in the n^{th} stage evaluated at energy U and is given by the Ericson formula [Bon81, Ric92]

$$\rho_N(U_n) = \frac{g(gU_n)^{N-1}}{p!h!(N-1)!}, \quad (2.45)$$

with g , the single-particle states in the equal spacing model, being proportional to the mass number A . The density of the states of the particle in the continuum $\rho_c(\vec{k}_n)$ with momentum \vec{k}_n is given by [May92]

$$\rho_c(\vec{k}_n) = \frac{mk_n}{(2\pi)^3 \hbar^2}. \quad (2.46)$$

Bonetti *et al.* [Bon81] assumed that the different angular momenta L contribute incoherently; consequently the average value of the squared matrix element can be written as

$$\left\langle \left| v(\vec{k}_i, \vec{k}_f) \right|^2 \right\rangle = \sum_L (2L+1) \left\langle \left| v_L(\vec{k}_i, \vec{k}_f) \right|^2 \right\rangle R(L), \quad (2.47)$$

where $R(L)$ is the general spin distribution function of the residual nucleus.

2.4 Polarisation and Analysing Power

By polarising the incident beam the spin interactions during a nuclear reaction can conveniently be investigated. The analysing power is an useful observable for this purpose, and it can enhance our understanding of the reaction mechanisms, especially the multistep reaction mechanisms. Consequently, in this study the analysing power served to identify the

contributions of the different steps towards the final values. The polarisation and analysing power can be related through the formulation which follows.

The polarization of a beam is defined as [Hil90]

$$\vec{P} = \text{Tr}(\rho \vec{\sigma}) / \text{Tr} \rho, \quad (2.48)$$

where $\vec{\sigma}$ are the Pauli spin operators and ρ represents a statistical density matrix. The relationship between the density matrixes for the incident channel ρ_{inc} , the density matrixes for the scattered channel ρ_{scatt} , the scattering amplitude matrix T and the cross section σ can be given by the following equations [Sat83];

$$\rho_{scatt} = T \rho_{inc} T^\dagger \quad (2.49)$$

and

$$\frac{d\sigma}{d\Omega} = \frac{\text{Tr} \rho_{scatt}}{\text{Tr} \rho_{inc}} = \sigma(\theta). \quad (2.50)$$

Substituting *equation 2.48* in the equation for the differential cross section (*equation 2.50*) results in [Hil90]

$$\begin{aligned} \sigma(\theta) = & 1/4 \text{Tr}(TT^\dagger) + 1/4 \vec{P}_1^{inc} \text{Tr}(T \vec{\sigma}_1 T^\dagger) + 1/4 \vec{P}_2^{inc} \text{Tr}(T \vec{\sigma}_2 T^\dagger) \\ & + 1/4 \sum_{\alpha, \beta} \overline{\langle \sigma_{1\alpha} \sigma_{2\beta} \rangle} \text{Tr}(T \vec{\sigma}_{1\alpha} \vec{\sigma}_{2\beta} T^\dagger), \end{aligned} \quad (2.51)$$

where $\vec{P}_1^{inc}, \vec{P}_2^{inc}$ denote the polarisation in the two-nucleon ensemble in the initial state. The α and β imply summation over all the x-, y-, z- components of the entrance and exit channels. Taking the target nucleons as unpolarised and the incident nucleons as polarised, the polarisation results in

$$\vec{P}_2^{inc} = 0 \quad (2.52)$$

and

$$\overline{\langle \sigma_{1\alpha} \sigma_{2\beta} \rangle} = 0. \quad (2.53)$$

Substituting this into *equation 2.51* then gives

$$\begin{aligned} \sigma(\theta) = & 1/4 \text{Tr}(TT^\dagger) + 1/4 \vec{P}_1^{inc} \text{Tr}(T \vec{\sigma}_1 T^\dagger) \\ = & \sigma_0(\theta)(1 + \vec{P}_1^{inc} \cdot \vec{a}), \end{aligned} \quad (2.54)$$

where $\sigma_0(\theta) = 1/4 \text{Tr}(TT^\dagger)$ and \vec{a} is given by

$$\vec{a} = \frac{\text{Tr}(T \vec{\sigma}_1 T^\dagger)}{\text{Tr}(TT^\dagger)}. \quad (2.55)$$

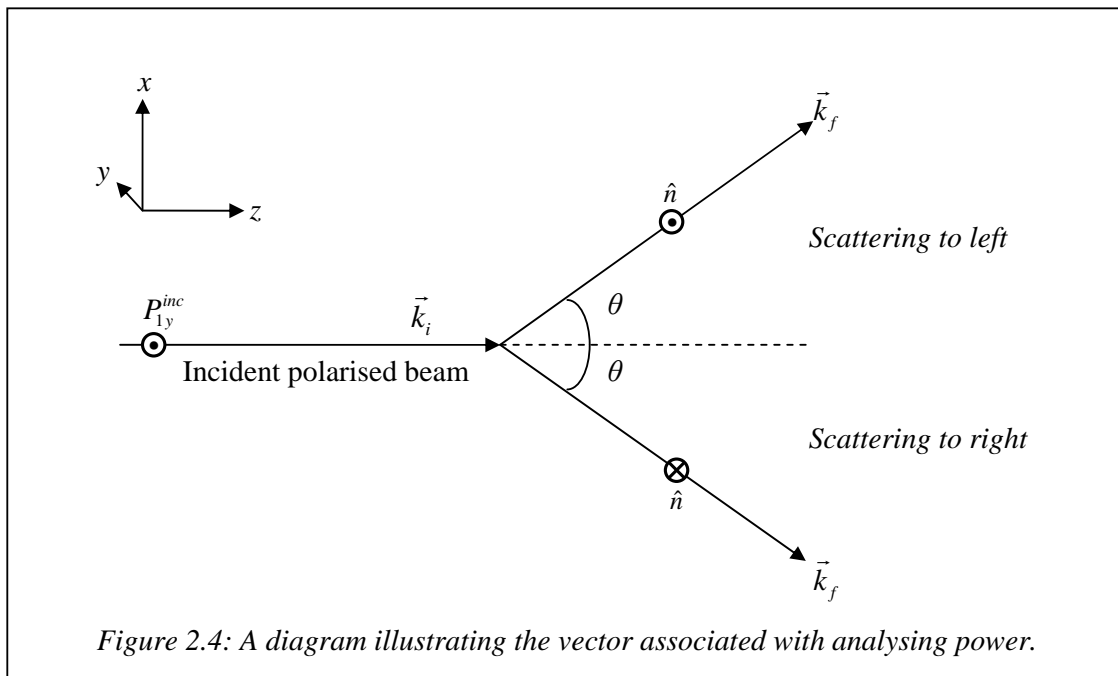
Expressing \vec{a} in terms of a unit vector \hat{n} gives

$$\vec{a} = a\hat{n}. \quad (2.56)$$

The unit vector \hat{n} is defined as [Hub61]

$$\hat{n} = \frac{(\vec{k}_i \times \vec{k}_f)}{|\vec{k}_f \times \vec{k}_i|}, \quad (2.57)$$

with \vec{k}_i and \vec{k}_f the momentum in the initial and final channels, respectively. The unit vector \hat{n} can thus be positive or negative, depending on the direction of the scattered particle. If the ejectile is scattered to the right of the incident beam the unit vector will be positive and the opposite is true for scattering to the left (see *figure 2.4*).



Consider P_{1y}^{inc} perpendicular to the scattering plane in the direction of the reader; this is generally defined as the up or positive y-axis direction [Bar71]. The cross section can be expressed for a scattering angle θ symmetrically to the right or left of the incident beam. The cross section right σ_R and the cross section left σ_L can then be expressed with the help of *equation 2.54* as

$$\sigma_R(\theta) = \sigma_0(\theta)(1 - aP_{1y}^{inc}) \quad (2.58)$$

and

$$\sigma_L(\theta) = \sigma_0(\theta)(1 + aP_{1y}^{inc}). \quad (2.59)$$

Combining these two equations produces

$$\frac{\sigma_L(\theta) - \sigma_R(\theta)}{\sigma_L(\theta) + \sigma_R(\theta)} = aP_{1y}^{inc} = A_y P_{1y}^{inc} = a\bar{P}_1^{inc} \cdot \hat{n}. \quad (2.60)$$

For a fully polarised incident beam the analysing power A_y can then be defined as

$$A_y = \frac{\sigma_L - \sigma_R}{\sigma_L + \sigma_R}. \quad (2.61)$$

In *figure 2.4* the incident beam is implied to be fully polarised but in practice during experimental runs it is only partially polarised. This beam polarisation would be included in *equation 2.61* and is usually expressed in percentage. The analysing power for each step in a multistep reaction can then be expressed as

$$A_i = \frac{\sigma_L^{i-step} - \sigma_R^{i-step}}{\sigma_L^{i-step} + \sigma_R^{i-step}}. \quad (2.62)$$

The final analysing power and double differential cross section for all the steps is then given as [Spa00]

$$A_y = \frac{A_1 \sigma^{one-step} + A_2 \sigma^{two-step} + \dots}{\sigma^{one-step} + \sigma^{two-step} + \dots} \quad (2.63)$$

with

$$\sigma_{L,R} = \left(\frac{d^2 \sigma}{d\Omega dE} \right)_{L,R} = \left(\frac{d^2 \sigma}{d\Omega dE} \right)_{L,R}^{one-step} + \left(\frac{d^2 \sigma}{d\Omega dE} \right)_{L,R}^{two-step} + \dots \quad (2.64)$$

2.5 Double Folding Model

In an elastic scattering interaction between a particle and a nucleus the wave function is obtained by solving the Schrödinger equation with an optical potential. In this study global optical parameter sets were used for the entrance channel in the theoretical calculations. As will be pointed out in *Chapter 5* theoretical calculations exhibited an unreasonably high sensitivity to the selection of a set of optical potential parameters for the exit channel. This sensitivity necessitated a different approach when determining the optical potential parameters for the potential of the exit channel. The double folding model that originates from the effective nucleon-nucleon interaction was subsequently employed for the present purpose.

If the energy of the projectile is adequately high (greater than 100 MeV) the effective nucleon-nucleon interaction can be approximated by a free nucleon-nucleon interaction; also

known as the impulse approximation. The nucleon–nucleon interaction generally depends on the distance between the nucleons, the spin of the nucleons and the velocity of the nucleons relative to one another [Kra88].

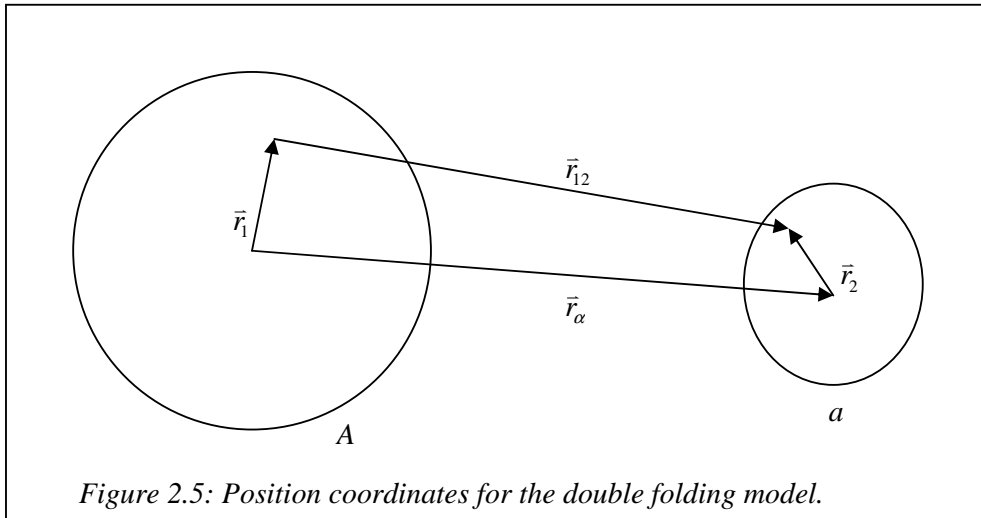
In the impulse approximation the nucleon-nucleon scattering amplitude can be represented by a t . The optical potential can then be obtained by averaging over all the t 's of all the possible distributions of nucleons in the colliding nuclei a and A . The equation for the optical potential can be written as (similar to *equation 2.3*)

$$U = \left\langle \psi_\alpha \left| \sum_{ij} t_{ij} \right| \psi_\alpha \right\rangle, \quad (2.65)$$

with i and j representing nucleons in a and A respectively. By introducing the local approximation $t_{ij} \rightarrow t(\vec{r}_{ij})$, the optical potential can be expressed as [Sat83]

$$U(r_\alpha) = \iint \rho_a(\vec{r}_i) \rho_A(\vec{r}_j) t(\vec{r}_{ij}) d\vec{r}_i d\vec{r}_j, \quad (2.66)$$

where ρ_a and ρ_A are the density distributions in the ground state of nuclei a and A respectively. The position coordinates are illustrated in *figure 2.5* with $r_{12} = |\vec{r}_\alpha - \vec{r}_2 + \vec{r}_1|$.



It should be noted that folding models are applied in a natural way to Coulomb force interactions where charge density plays an important role. The strong relationship between nucleon density in the nucleus and the nuclear potential provides good motivation also for calculating the nuclear potential for a projectile nucleus colliding with a target nucleus as a nucleon-nucleon interaction folded over the individual densities of the projectile and the

target. The folding model potential thus provides an alternative to an analytical potential, notably with a stronger intuitive foundation.

Similar to *equation 2.66* the double folded microscopic optical potential for ${}^3\text{He}$ can be expressed in terms of an effective nucleon-nucleon interaction $v_{\text{eff}}(E, \rho_{3\text{He}}, \rho_A, \bar{r}_{12})$ as [Sat79]

$$V_{DF}(r_\alpha) = \iint \rho_{3\text{He}}(\bar{r}_2) \rho_A(\bar{r}_1) v_{\text{eff}}(E, \rho_{3\text{He}}, \rho_A, \bar{r}_{12}) d\bar{r}_1 d\bar{r}_2, \quad (2.67)$$

where $r_{12} = |\bar{r}_\alpha - \bar{r}_2 + \bar{r}_1|$ and ground state density distributions $\rho_{3\text{He}}$ and ρ_A represent the distribution for the ${}^3\text{He}$ particle and the target nucleus respectively. The energy E represents the relative energy between the two nuclei (A and ${}^3\text{He}$) specified in the double folding potential.

Bertsch *et al.* [Ber77] expressed the effective nucleon-nucleon interaction as the sum of three Yukawa terms and named it the M3Y potential. Cook *et al.* [Coo81, Coo87] subsequently employed the M3Y effective potential in the double folding model for ${}^3\text{He}$ elastic scattering reactions. The effective interaction can be written [Coo87] as

$$v_{ST}(\bar{r}_{12}) = v_{00}^C(\bar{r}_{12}) + v_{01}^C(\bar{r}_{12}) + [v_0^{ls}(\bar{r}_{12}) + v_1^{ls}(\bar{r}_{12})] \bar{L} \cdot \bar{S}, \quad (2.68)$$

where S and T are the transferred spin and isospin respectively, with the selection rule $S + T = 1$. The central terms of the interaction are given as

$$v_{00}^C(\bar{r}_{12}) = 7999 \frac{e^{-4\bar{r}_{12}}}{4\bar{r}_{12}} - 2134 \frac{e^{-2.5\bar{r}_{12}}}{2.5\bar{r}_{12}} - 409\delta(\bar{r}_{12}) \quad (2.69)$$

and

$$v_{01}^C(\bar{r}_{12}) = -4886 \frac{e^{-4\bar{r}_{12}}}{4\bar{r}_{12}} + 1176 \frac{e^{-2.5\bar{r}_{12}}}{2.5\bar{r}_{12}} + 293\delta(\bar{r}_{12}), \quad (2.70)$$

while the spin-orbit terms of the interaction is given as

$$v_0^{ls}(\bar{r}_{12}) = -4008 \frac{e^{-4\bar{r}_{12}}}{4\bar{r}_{12}} - 930 \frac{e^{-2.5\bar{r}_{12}}}{2.5\bar{r}_{12}} \quad (2.71)$$

and

$$v_1^{ls}(\bar{r}_{12}) = -1336 \frac{e^{-4\bar{r}_{12}}}{4\bar{r}_{12}} - 310 \frac{e^{-2.5\bar{r}_{12}}}{2.5\bar{r}_{12}}. \quad (2.72)$$

Only the $v_{00}^C(\bar{r}_{12})$ and $v_0^{ls}(\bar{r}_{12})$ terms were used in the calculations as the contribution of the other terms toward the double differential cross section is negligible [Coo81, Sat79].

Kobos *et al.* [Kob82, Kob84] added a density dependence to the M3Y effective potential by including a density function $g(\rho_{^3\text{He}}, \rho_A, E)$ to the central term. This potential, which is then referred to as the DDM3Y potential, was applied successfully to elastic and inelastic alpha particle scattering. The DDM3Y effective nucleon-nucleon potential as expressed by Kobos *et al.* [Kob82] was used in the double folding model in that investigation

$$v_{00}^C(\rho_{^3\text{He}}, \rho_A, \bar{r}_{12}, E) = f(\bar{r}_{12}, E) \cdot g(\rho_{^3\text{He}}, \rho_A, E), \quad (2.73)$$

with

$$f(\bar{r}_{12}, E) = 7999 \frac{e^{-4\bar{r}_{12}}}{4\bar{r}_{12}} - 2134 \frac{e^{-2.5\bar{r}_{12}}}{2.5\bar{r}_{12}} - 276(1 - 0.005 \cdot E) \delta(\bar{r}_{12}) \quad (2.74)$$

and

$$g(\rho_{^3\text{He}}, \rho_A, E) = C(E) \cdot (1 + \alpha(E)) e^{\beta(E)\rho}. \quad (2.75)$$

$C(E)$, $\alpha(E)$ and $\beta(E)$ are energy dependent coefficients and the density ρ is given by

$$\rho = \rho_{^3\text{He}} + \rho_A. \quad (2.76)$$

The ground state density distributions for the helion $\rho_{^3\text{He}}$ and the target nucleus ρ_A are normalised through [Sat83]

$$\int \rho_A(\bar{r}) d\bar{r} = n_A \quad (2.77)$$

and

$$\int \rho_{^3\text{He}}(\bar{r}) d\bar{r} = n_{^3\text{He}}, \quad (2.78)$$

where $n_{^3\text{He}}$ and n_A are the number of nucleons in the helion and the target nuclei respectively.

The double folded model potential produces only a real part. To account for absorption of flux an imaginary part has to be included in the potential and this is usually done by a phenomenological procedure. The inclusion of such an imaginary part is discussed in *Chapter 5*.

Chapter 3: THE EXPERIMENT

3.1 Overview

The experimental setup and experimental methods used during data acquisition are discussed in this chapter. The setup is similar to the one used in the study by Cowley *et al.* [Cow00] at iThemba Laboratory for Accelerator Based Science (LABS). The techniques used in this experiment are also regularly employed in experimental nuclear physics and no new methods needed to be developed.

The layout of the chapter is as follows: In the first section some information on the iThemba LABS facility is given. The next three sections discuss the proton beam, the scattering chamber and the targets. Section 3.6 discusses the detectors that were used during the experiment. In section 3.7 an overview is given of all the electronics required for signal processing. Section 3.8 describes the computer hardware and software employed for the handling of data, and finally the experimental procedure is described in section 3.9.

3.2 Facility

The experiment was performed at iThemba LABS at Faure in the Western Cape, South Africa. This is a multidisciplinary facility providing in the needs of three user communities, being basic nuclear physics research, radiotherapy and a radio-isotope production service. A layout of iThemba LABS is shown in *figure 3.1*. During the week radiotherapy and radio-isotope production share the use (see *figure 3.1* beam line I and vaults TL, TC and TR). The facility is only available for nuclear physics research on weekends. The experiment was conducted over a period of five weekends.

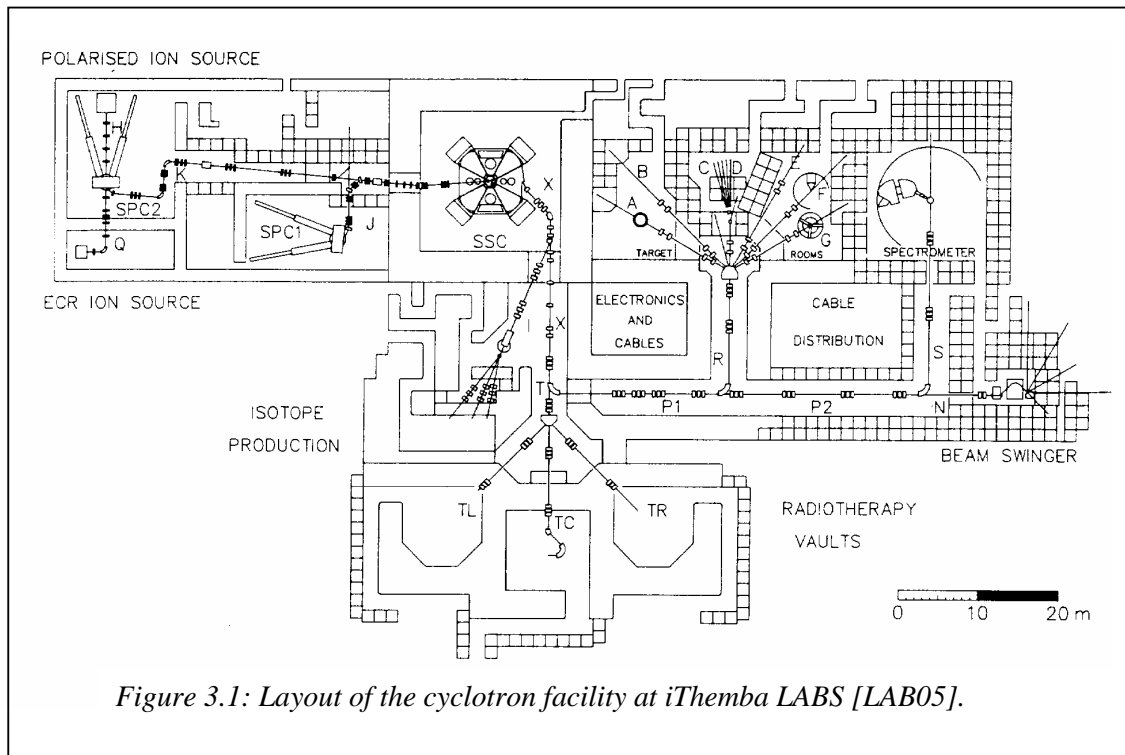


Figure 3.1: Layout of the cyclotron facility at iThemba LABS [LAB05].

3.3 Proton Beam

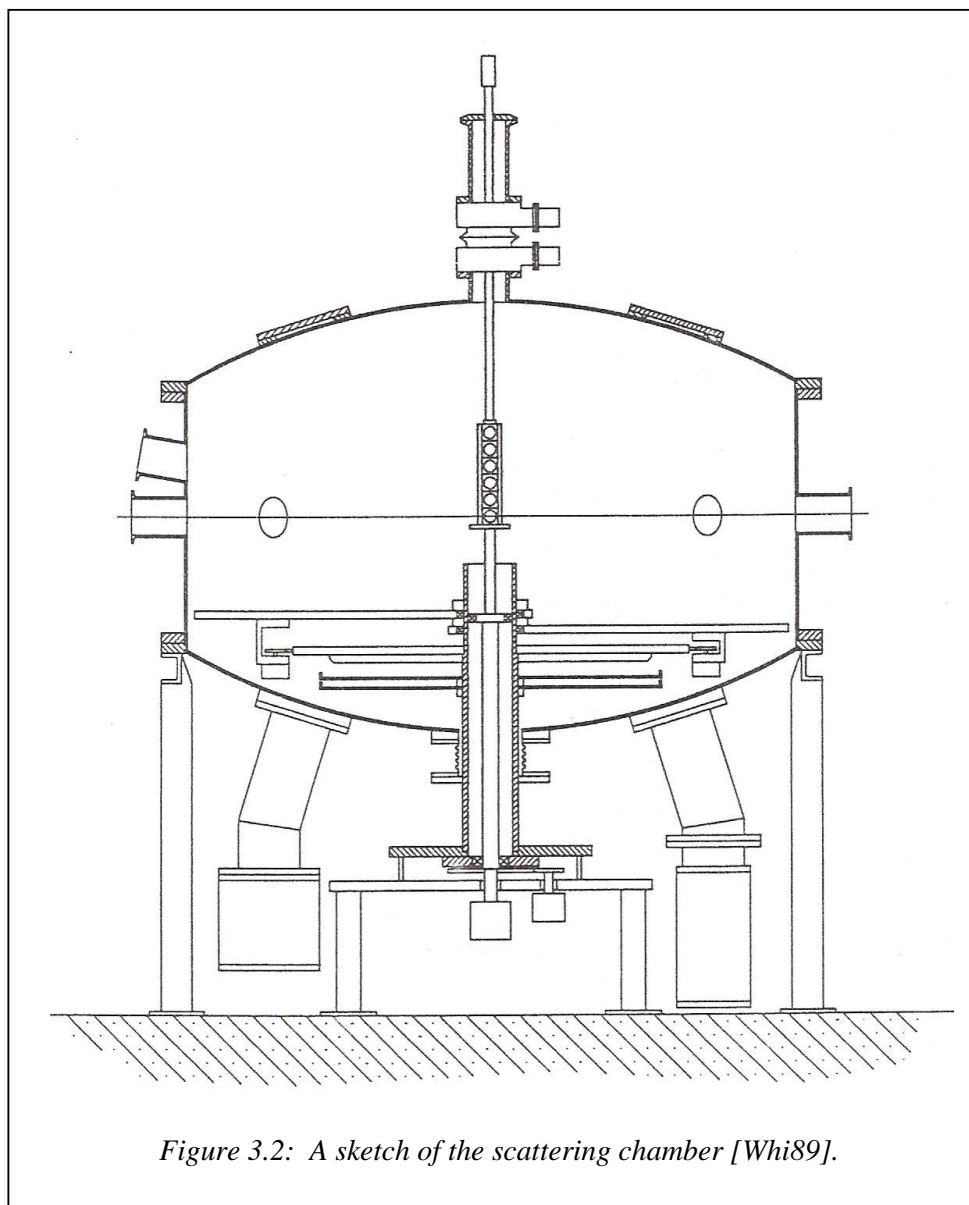
A beam of polarised protons was used to bombard two different targets. Polarised protons were obtained from an ion source, fed by hydrogen gas. The beam was polarised normal to the momentum of the beam in either the up or down direction. During each run the polarisation was automatically alternated at intervals of 10 s between these two orientations. Beam polarisation values of between 64 % and 82 % were obtained for both the up and down polarisation. In the first stage the polarised protons were accelerated to between 5 MeV and 8 MeV in the second Solid Pole Injector (SPC2). The polarised beam was then transported along beam lines to the Separated Sector Cyclotron (SSC), where the beam was further accelerated to an energy of either 130 MeV or 160 MeV, depending on the beam energy needed for the experiment with the selected targets.

From the SSC the polarised beam was transported via the high-energy beam lines and delivered to the scattering chamber in the A vault. Quadrupole magnets were used to focus the beam, while dipole magnets energy defined the beam. In the centre of the scattering

chamber the polarised beam then collided with a pre-selected target positioned on a target ladder.

3.4 Scattering Chamber

The scattering chamber is a steel cylinder with several ports. The diameter of the scattering chamber is 1.5 m and the height varies between 1 m and 2 m. A sketch of the scattering chamber is given in *figure 3.2*.



The ports of the scattering chamber are used as feed-through for electric cables as well as for the incident and out-going beams. The incident beam hits the target in the target ladder at the centre of the chamber and the fraction of the beam that does not undergo a nuclear reaction with the target exits the chamber through a port and is absorbed in the beam stop. Two detector arms on which the different detectors were mounted are also fitted in the scattering chamber. A plan view of the inside of the scattering chamber, which shows the layout of the

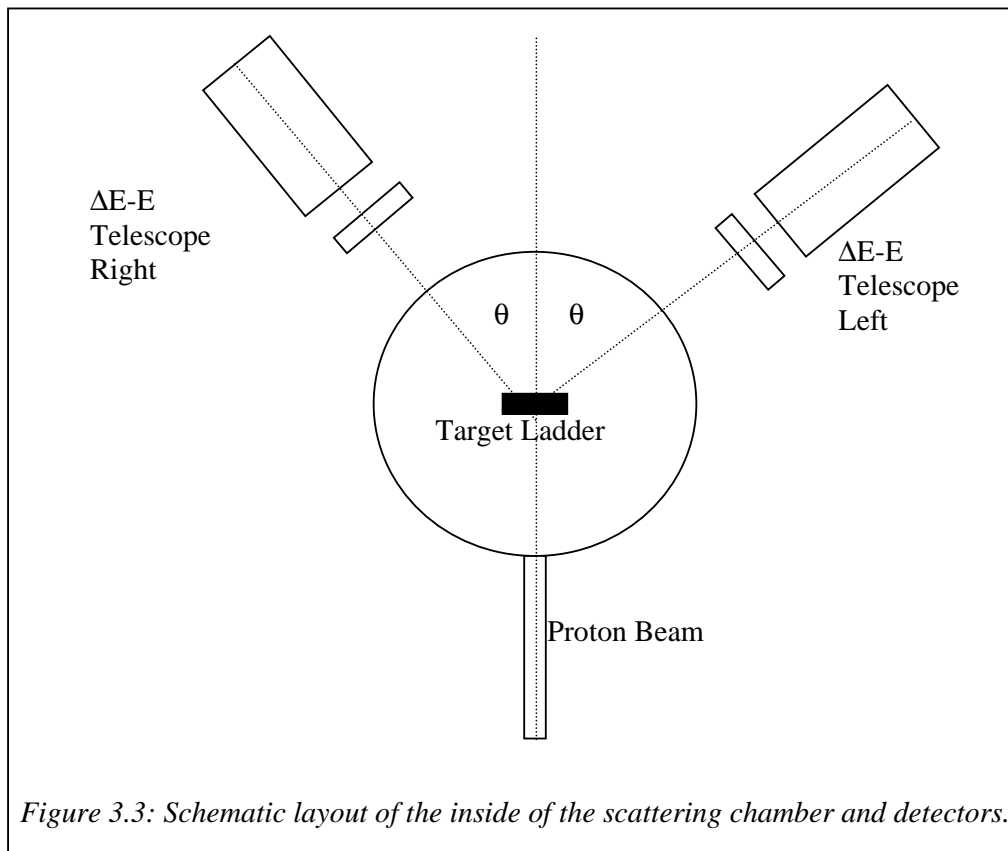


Figure 3.3: Schematic layout of the inside of the scattering chamber and detectors.

target ladder and detectors, is displayed in *figure 3.3*. The target ladder and arms on which the detectors were mounted could be driven by electric motors, in order to alter the experimental arrangement without opening the scattering chamber. The targets in the target ladder are mounted vertically above one another. The targets in the ladder can then be selected by driving the ladder up and down through the beam line position. The target ladder can also rotate around its central axis. As was already mentioned, the two detector telescopes in the scattering chamber are also mounted on movable arms. This allows the angle between each detector telescope and the incoming beam to be independently selected. All the

movements of the target ladder and the detector arms could be controlled from either inside the vault or from the data room.

Pre-amplifiers were placed in the scattering chamber and these were connected to the data room via cables exiting through the ports. Cables for the high voltage of the detectors also entered the scattering chamber through the ports, making it possible to adjust the operation potential of the detector from the data room. A photo of the target ladder and detector set-up is shown in *figure 3.4* and the pre-amplifiers placed on the telescope arms are visible.

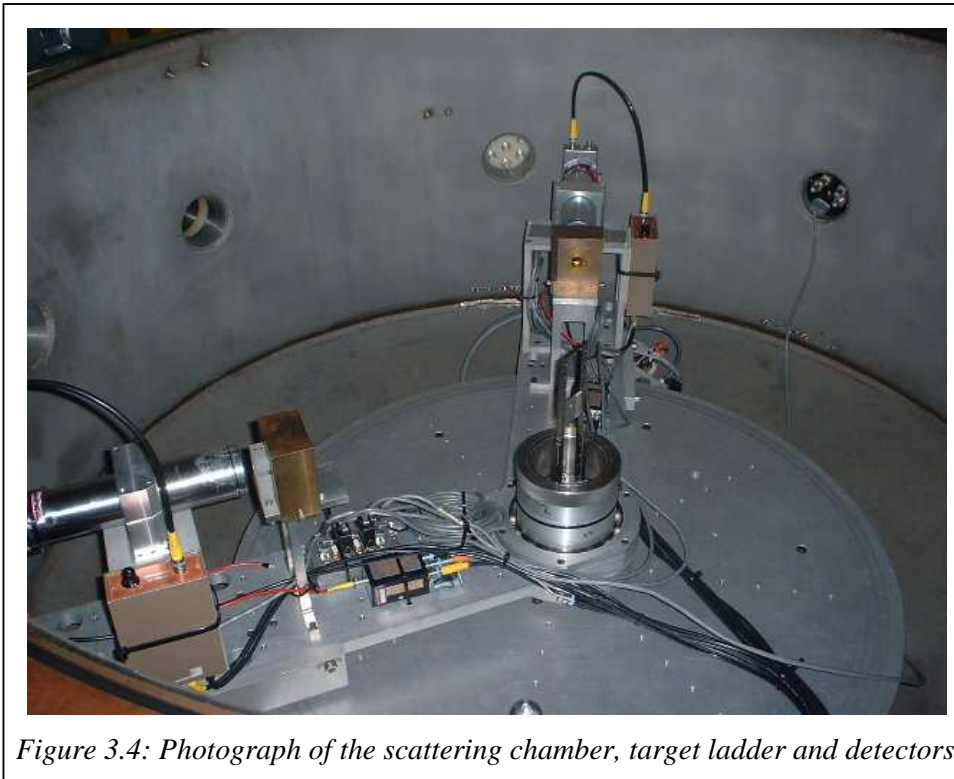


Figure 3.4: Photograph of the scattering chamber, target ladder and detectors.

One of the ports was used as a window through which a closed circuit video camera viewed the target position. The camera was used to visually tune the beam to be on the centre of the target position with the help of a scintillating target. In this experiment a ruby target (Al_2O_3) was used for this purpose.

The whole chamber and the beam line had to be maintained at a vacuum of $\cong 10^{-5}$ mbar. This was achieved by pumping down the scattering chamber in three stages before the commencement of the experiment. First a mechanical rotor pump was used to obtain a

vacuum of $\cong 1$ mbar. When this vacuum was reached a turbo molecular pump was engaged to obtain a vacuum of $\cong 10^{-3}$ mbar. Lastly a cryogenic pump was initiated in combination with the turbo molecular pump to maintain the scattering chamber at the required vacuum of $\cong 10^{-5}$ mbar.

3.5 Targets

The target ladder has an array of six slots in which the targets were fitted. Two arrays of targets were used in the experiment; one containing the cobalt targets and the other containing the niobium targets. The cobalt array consisted of two empty positions, a ruby, a thick ($10\ \mu\text{m}$) ^{59}Co disk ($8.90 \pm 0.62\ \text{mg}/\text{cm}^2$) and ^{12}C target. The niobium array consisted of two empty positions, a ruby, a thick ($10\ \mu\text{m}$) ^{93}Nb disk ($8.57 \pm 0.52\ \text{mg}/\text{cm}^2$), ^{12}C and a thin ($3\ \mu\text{m}$) ^{93}Nb disk ($2.57 \pm 0.17\ \text{mg}/\text{cm}^2$). The uncertainty in the target thicknesses is therefore less than 7%.

The beam was aligned and adjusted with the aid of the ruby crystal in a target position. The ruby target has a 3 mm hole in the centre and this allows the focused beam to pass through. Visible light is produced if the beam collides with the ruby around the hole. This light is observed with closed circuit television from the data room and the beam is then adjusted to the centre of the ruby. The beam can thus be focused to a position in the centre of the target position to an error of less than 3 mm.

The empty-frame positions in the target ladder were used to check to what extent incident projectiles are constrained to be within the main envelope of the beam. A negligible count rate in the detectors from an empty target position indicated that the definition of the beam is of high-quality. A readout of each of the two detector arm angles is available in the data room. As the normal readout may have a slight error with respect to the true angle relative to the beam, this offset needs to be determined by comparing the count rates to the left and to the right of the incident beam for each detector arm. These offset errors need to be known. The offset errors are commonly known as the beam offset for each arm. The ^{12}C target was used for the determination of the beam offsets, the calibration of the sodium iodide [NaI(Tl)] scintillation crystal detectors and in polarisation runs during the weekends of the experiment. The actual procedure will be discussed later.

3.6 Detector Telescopes

In this experiment two ΔE - E detector telescopes were used to measure the energy of the emitted particles and also identify the different emitted particles. Each of the two ΔE - E telescopes consisted of a silicon (Si) detector (associated with an energy loss ΔE) and a sodium iodide [NaI(Tl)] crystal (associated with the remaining energy E). The ΔE - E telescopes and their pre-amplifiers are clearly visible on the metal movable arms in the photograph of the scattering chamber, *figure 3.4*. The two arms with the detector telescopes were normally kept at equal angles on opposite sides of the incident beam for the data production runs. This arrangement of the two ΔE - E telescope arms decreased systematic errors in the analysing power measurements (see the discussion in section 2.4 on analysing power and polarisation).

A photograph of a ΔE - E detector telescope is shown in *figure 3.5*. In the photograph the particles enter from the right, passing through a brass collimator, a Si detector (not yet fitted in the white Teflon block) and a NaI(Tl) detector (the metal tube). A thin sheet of kapton (8 μm thick) was placed in front of the brass collimator to shield the Si detector from low energy electrons that are emitted from the target due to atomic collisions of protons.

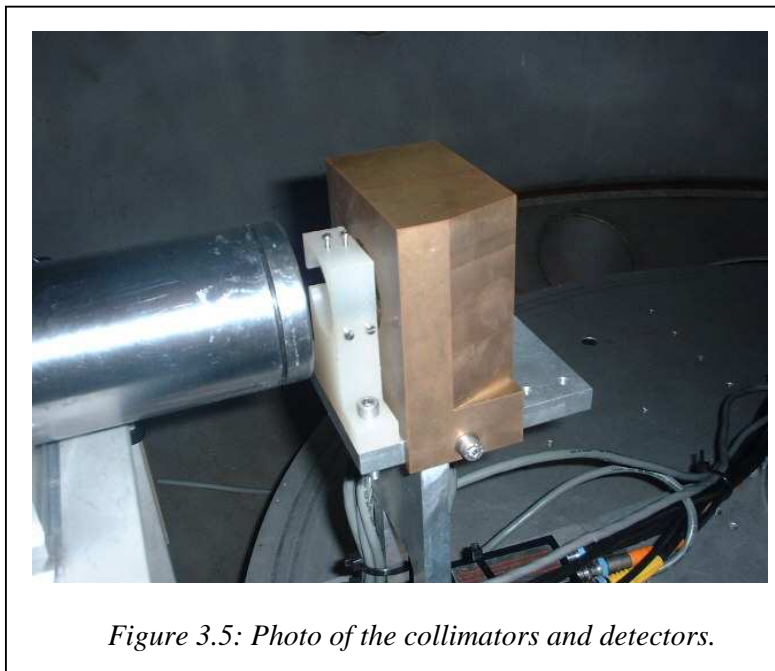


Figure 3.5: Photo of the collimators and detectors.

The dimension of the brass collimators (66 mm wide, 43 mm long and with a 17 mm diameter hole in the centre) determined the solid angles of each of the detector telescopes. Collimators with similar dimensions were chosen, resulting in solid angles of 1.103 ± 0.018 msr and 1.105 ± 0.017 msr for the lower and upper arms respectively. A Teflon frame (a small white block in the photo, *figure 3.5*) was mounted behind to the brass collimator on each telescope arm to house the Si detector.

The thicknesses of the Si and NaI(Tl) detectors were chosen to optimise the detection of helion particles. Calculations with the kinematic code KINMAT showed that an appropriate thickness of the Si detectors was 0.5 mm. The available NaI(Tl) detectors had a thickness of 125 mm and this means that all the reaction products were stopped by the NaI(Tl) detectors in this experiment. As NaI is hygroscopic the detectors were canned and had entrance windows of Havar (7 μm thick) to protect the scintillation crystals. A small amount of the energy of the observed particle is lost in the Havar entrance window, typically $\cong 0.03$ MeV for protons.

Compared to the energy deposited in the NaI(Tl) detectors, small amounts of energy were lost in the Si detectors. The energy loss of the helion particles in the Si and NaI(Tl) detectors as calculated with KINMAT is compared in *figure 3.6*. In *figure 3.7* the energy loss of alphas, helions, tritons, deuterons and protons in the Si detector is plotted as a function of the loss of energy in NaI(Tl) detector.

Light emitting diodes (LED), controlled by a pulser system, were embedded in the NaI(Tl) crystals. The NaI(Tl) detectors were calibrated with elastic and inelastic scattering of protons from the ^{12}C target, at the beginning of each weekend, and the pulser peak was then used as a reference point to monitor gain drifts. The pulser peak appeared in the measured energy spectrum and from there gain drift could be measured and corrected for. The gain drift corrections are discussed further in *section 4.5.1*.

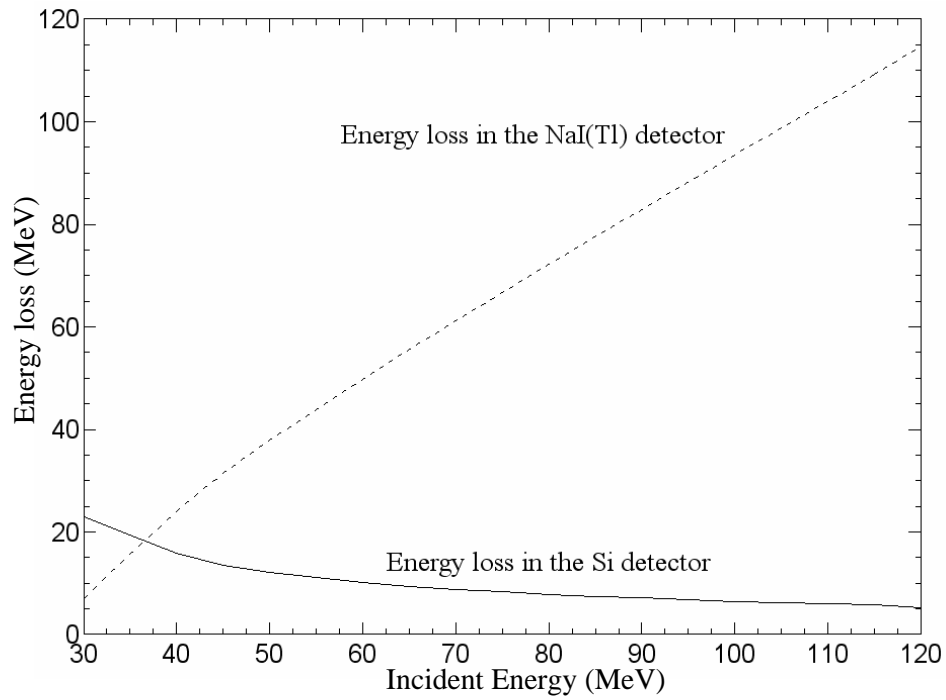


Figure 3.6: Energy loss of helions in the Si (Solid line) and NaI(Tl) (dash line) detectors as a function of the total incident energy.

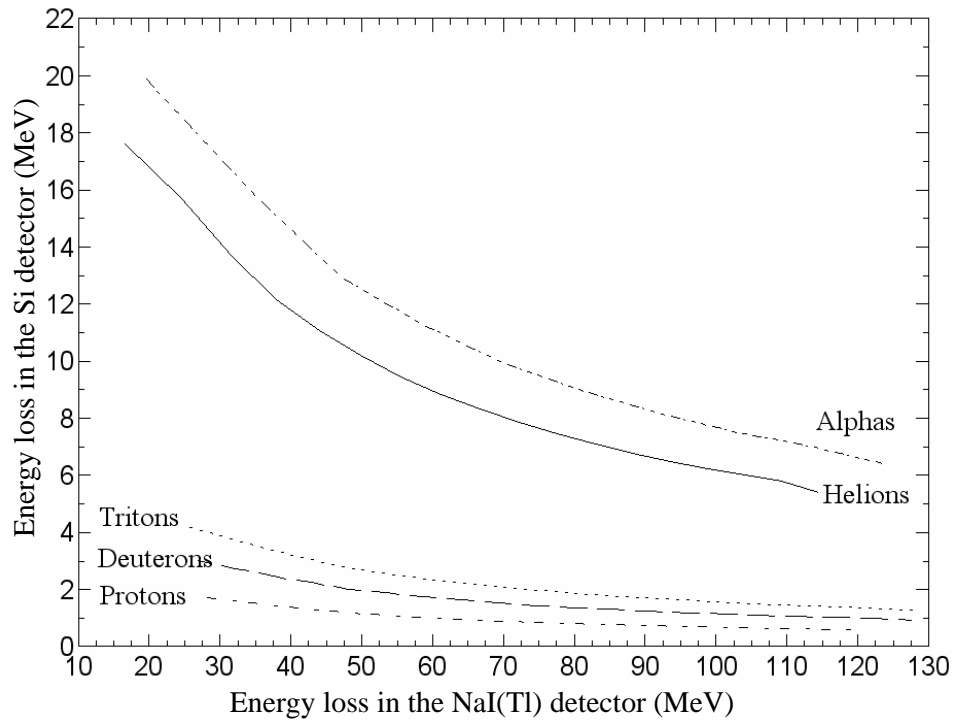


Figure 3.7: Energy loss of alphas, helions, tritons, deuterons and protons in the Si detector as a function of the energy loss in the NaI(Tl) detector.

3.7 Electronics

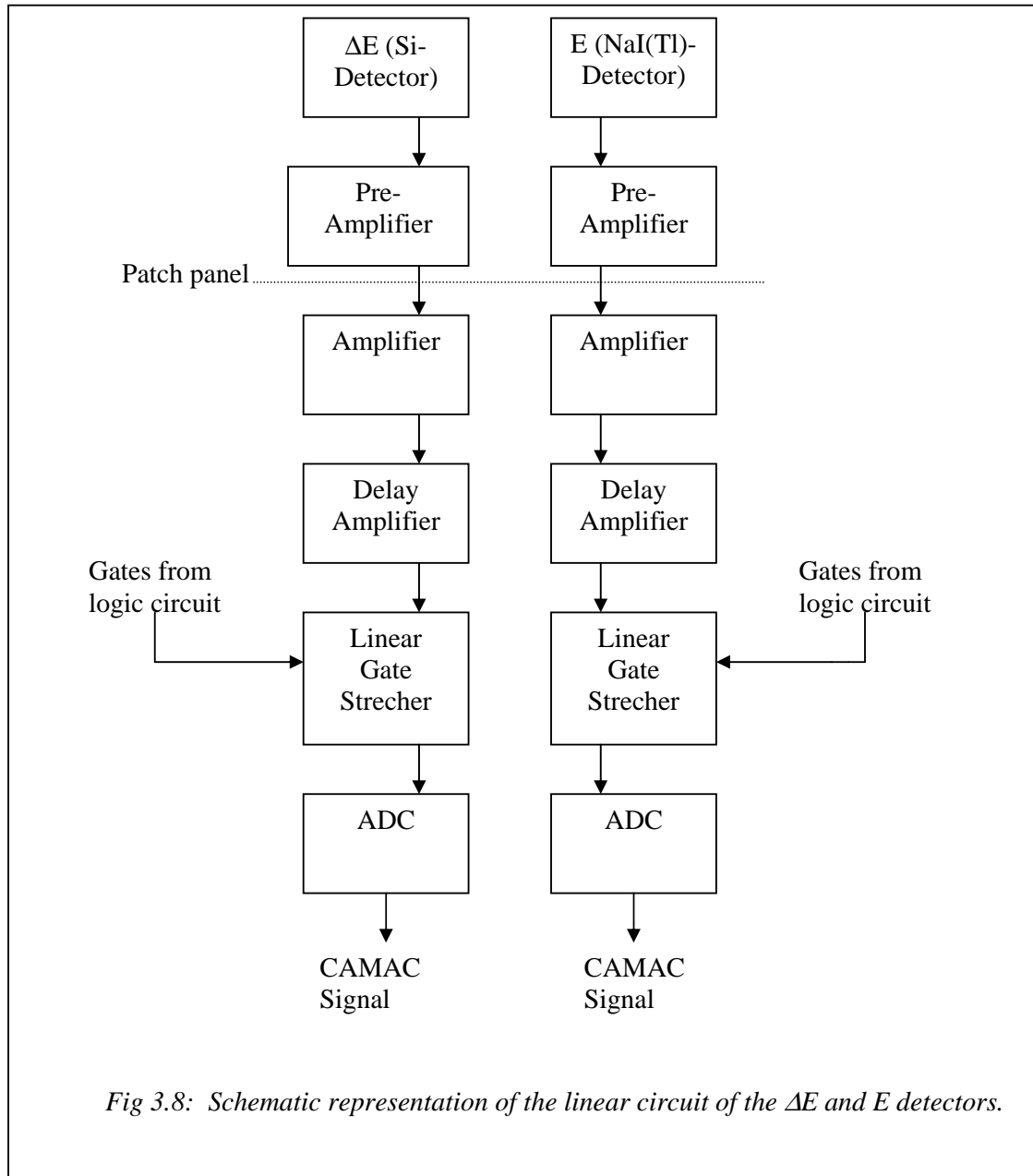
Only the pre-amplifiers of the Si and NaI(Tl) detector were placed in the scattering chamber and for ease of access and adjustment all the remaining electronics for processing of signals were placed in the data control room at iThemba LABS. The electronics adhered to either the standards of Computer Automated and Control (CAMAC) or Nuclear Instrument Module (NIM). The functions of the electronic modules are discussed in the following subsections.

3.7.1 Pre-amplifiers

The Si and NaI(Tl) detectors generate very weak signals when particles deposit energy. To reduce spurious electronic interference of these signals, the pre-amplifiers were placed in the scattering chamber as close as possible to the detectors. The charge sensitive pre-amplifiers of the Si detector generated a fast timing signal and a slow linear signal for the ΔE element in the acquisition process, whereas the pre-amplifier of the NaI(Tl) detector generated the linear signal and fast timing signal for the E element in the acquisition process. The timing signals were transported to the data room via the patch panel system. The patch panel is a signal cable system that is a permanent fixture at iThemba LABS and it connects the experimental vaults to the data room. BNC cables with an impedance of 50Ω and 93Ω were used to transport timing and linear signals, respectively, from the scattering chamber to the data room.

3.7.2 Linear Signals

A schematic representation for the linear circuit of the Si and NaI(Tl) detectors is shown in *figure 3.8*. The linear part of the circuit carries information about the amount of energy that was deposited in each detector. After being amplified by the pre-amplifiers in the scattering chamber, the signals were sent via the patch panel to a second set of amplifiers and delay amplifiers that were placed in the data control room. The signal was fed into a Linear Gate and Stretcher (LGS) where a logic timing signal was required to open the gate if a coincidence existed between the Si and NaI(Tl) detectors. In the case of a coincidence event the linear signal was converted to a digital signal by means of an Analogue to Digital Converter (ADC) and stored.



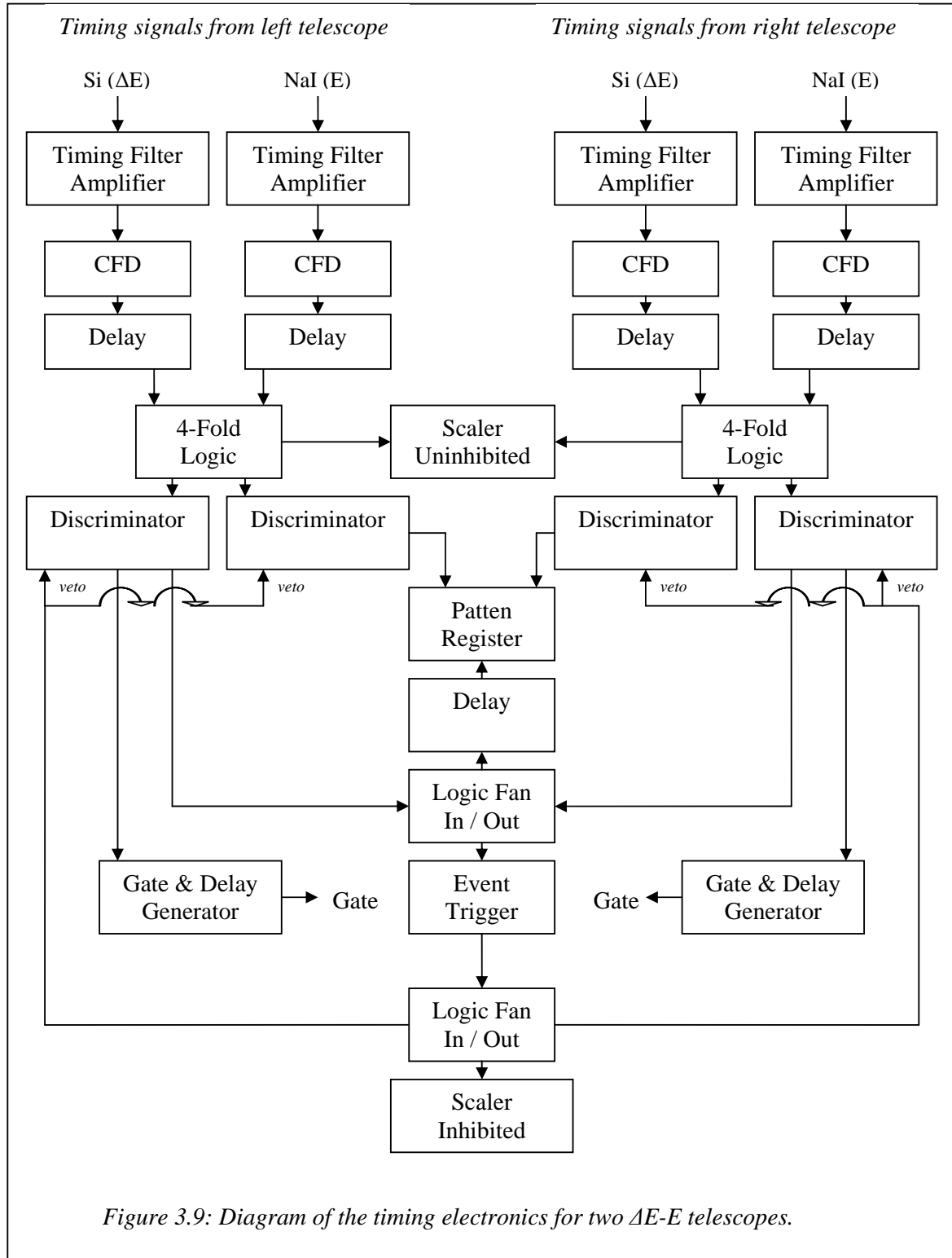


Figure 3.9: Diagram of the timing electronics for two ΔE -E telescopes.

3.7.3 Timing Signal

The timing signals were also processed in the data control room. The timing signals from each element (ΔE and E) of each telescope were tested for a coincidence, the presence of which means that a single particle traversed both telescope elements. If a coincidence event was present and the registering system was not busy (no veto was enforced), the event was registered and stored. In *figure 3.9* the timing logic for the telescopes is illustrated.

3.7.4 Current Integration

The current from the beam stop was transported to the data control room, where it was fed into the current integrator. The current integrator linearly associates a number of pulses per second to the current, with a full-scale value of 1000 pulses per second. In addition to the use of these pulses as an indication of the integrated current, they were also used to estimate electronic dead time in the system during data acquisition and also to provide a trigger for the pulser system. The digital pulser output was split in two with the help of a Gate and Delay Generator (GDG). The signals acted as gain drift triggers and provided the pulser signal that measured the electronic dead time. A diagram of the current integrator and pulsers is given in *figure 3.10*.

3.7.5 Computer dead time measurement

The computer dead time was measured by means of one of the pulser signals. The pulser signal was split in two with a discriminator. The pulser signal was split in two and registered in separate scalers. A busy signal from the computer inhibited one of these scalers, whereas the other one was uninhibited. By taking the ratio between the number counts in the inhibited scaler and those in the uninhibited scaler, the dead time could be determined. A large difference between the inhibited and uninhibited values indicated that too many events were taking place and the computer system could not keep up with logging all the data. Although there was no need to apply any correction to the data for this computer dead time, it nevertheless served as an indication of the efficiency of data collection.

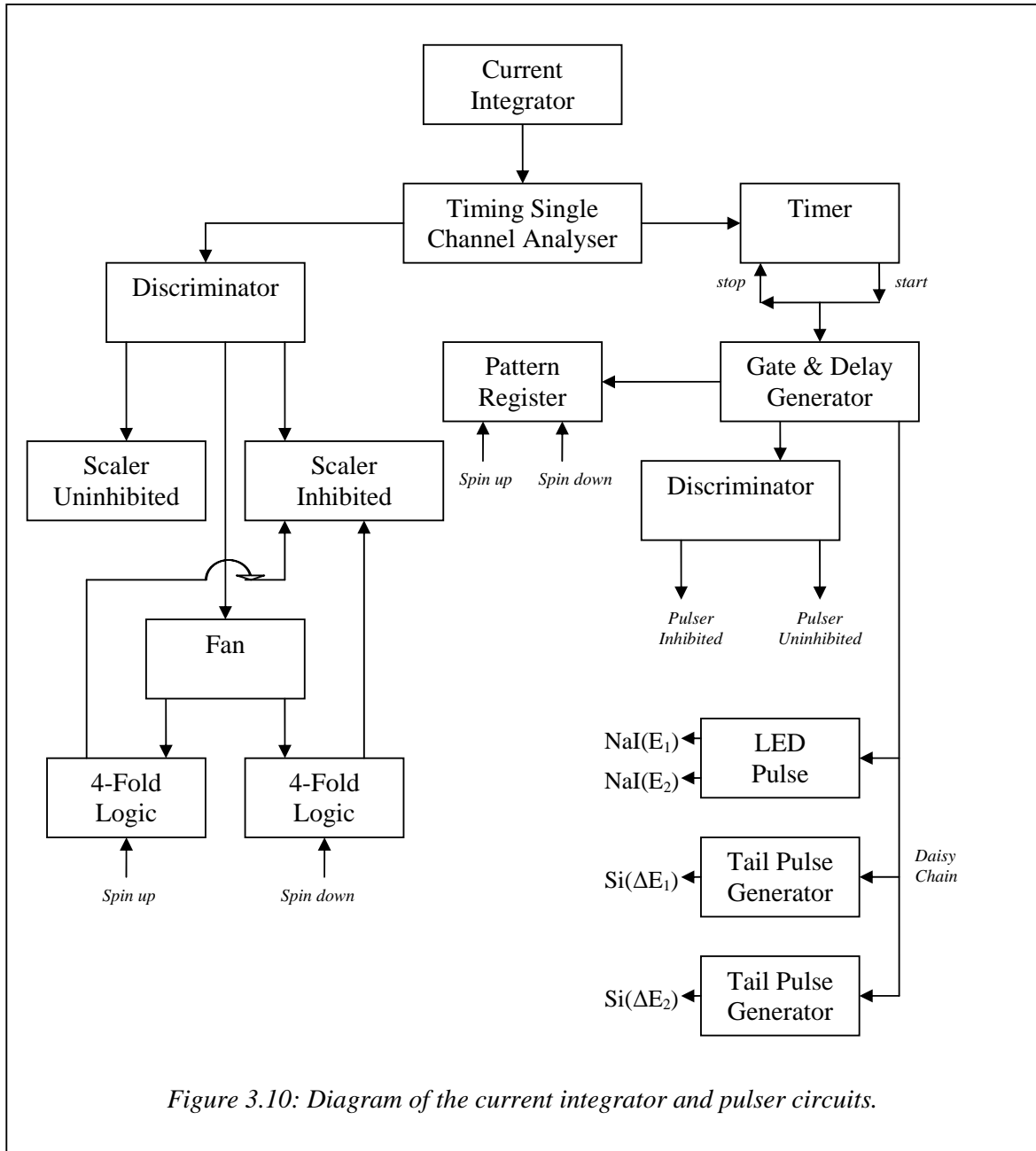


Figure 3.10: Diagram of the current integrator and pulser circuits.

3.8 Data Handling

3.8.1 Computer Interface

The data handling hardware consists of NIM modules, CAMAC crates and a VME front-end. The data is transferred from the NIM's (electronic hardware) via the CAMAC crates, to the VME front-end. The VME is the interface to a VAX data computer and this dedicated VAX did the online data recording. For further information on the hardware of the acquisition systems see the references [Yo94, För92, Pil96].

3.8.2 Software

The software used to control data acquisition originates from the system XSYS, which runs in the VAX VMS operating system environment. In XSYS two program codes are run to handle data, namely the COM file and the EVAL file.

The COM file creates the necessary common virtual memory data areas for the data to be stored. These data areas include normal variables, arrays, gates and two dimensional and three dimensional graphs. The EVAL code (event analyses language) sorts and analyses the raw data stream and stores it in the data areas created by the COM File. This raw data for each run is stored in an event file (EVT file) and these data files can be copied and played back with preset software gates and offline sorting routines at a later time to analyse data. The same COM, EVAL and event files are used for later playbacks and this can be done on any VAX computer with the XSYS software package. For further information on the software of the acquisition systems see the relevant references [Pil89, Ste97, Whi89].

3.9 Experimental Procedure

The experiment was performed over five weekends and experimental data were collected on each of these weekends. During the first two weekends experimental data were collected with ^{93}Nb targets at an incident energy of 130 MeV. During the last three weekends experimental data were collected with ^{59}Co targets at incident energies of 130 MeV and 160 MeV. The detectors, the initial target ladder and the electronics were installed before commencement of the first weekend of the experiment. The detector arms and target ladder

were also aligned and electronically tested during the installation phase. On the commencement of the first weekend all the energy resolutions and settings were determined.

The Si detectors were energy calibrated at the commencement of each weekend with the aid of an alpha emitting ^{228}Th radioactive source. The ^{12}C target with the incident proton beam was used to calibrate the energy of the NaI(Tl) detectors and this was also done at the beginning of each experimental weekend. During the weekend the energy calibration of the NaI(Tl) detectors were repeated if there was an indication that gain drift might have been excessive. As described before, at the start of each weekend the beam was centred on the target position with the aid of a ruby crystal. The beam quality was checked with the empty frame position in the target ladder.

At the beginning of each weekend the detector arm offset for each arm was also determined. These offsets needed to be determined for each weekend and were done by scattering an unpolarised proton beam on the ^{12}C target. Counts were taken with the same detector arms at equal instrument angles to the left and to the right of the beam line. Equal count rates to the left and to the right of the beam indicated the correspondence between different nominal readings.

The ^{93}Nb and ^{59}Co experimental runs typically lasted 2 hours for each continuous measurement and were alternated with ^{12}C runs to determine the beam polarisation. The data from these runs were all acquired with XSYS, as the COM and EVAL file were executed in real time while the experiment was in progress. The preliminary online data were monitored for integrity of data collection. The offline analysis of the data was done after the experiment was completed. This data analysis is discussed in *Chapter 4*.

Chapter 4: FINAL DATA ANALYSIS

4.1 Overview

In this chapter the techniques that were used to extract final experimental data are discussed. Some of the methods used were programmed directly in the EVAL code and applied during acquisition as well as playback of data. Other analyses were done with various computer programs such as KINMAT and ELOSS. The discussion of the analysis also includes the methods and techniques that were used in the calculations of the experimental double differential cross section and experimental analysing power. Of course, some of the procedures were very similar to those employed during the online process. However some other crucial corrections could only be determined by repeated replays and adjustments.

In the first section, the energy calibrations of the detectors in the detector telescopes are discussed. The following section is a discussion on the technique that was used to identify the different particles that emerged from the nuclear reaction. In section 4.4 the projection spectra that were used to extract the counts are discussed. In section 4.5 all the corrections that were made to the data are explained. In section 4.6 and 4.7 an overview is given of the double differential cross section and the analysing power calculations respectively; specific mention is also made of the statistical errors on these two observables. Section 4.8 summarises the systematic errors that were associated with the experiment.

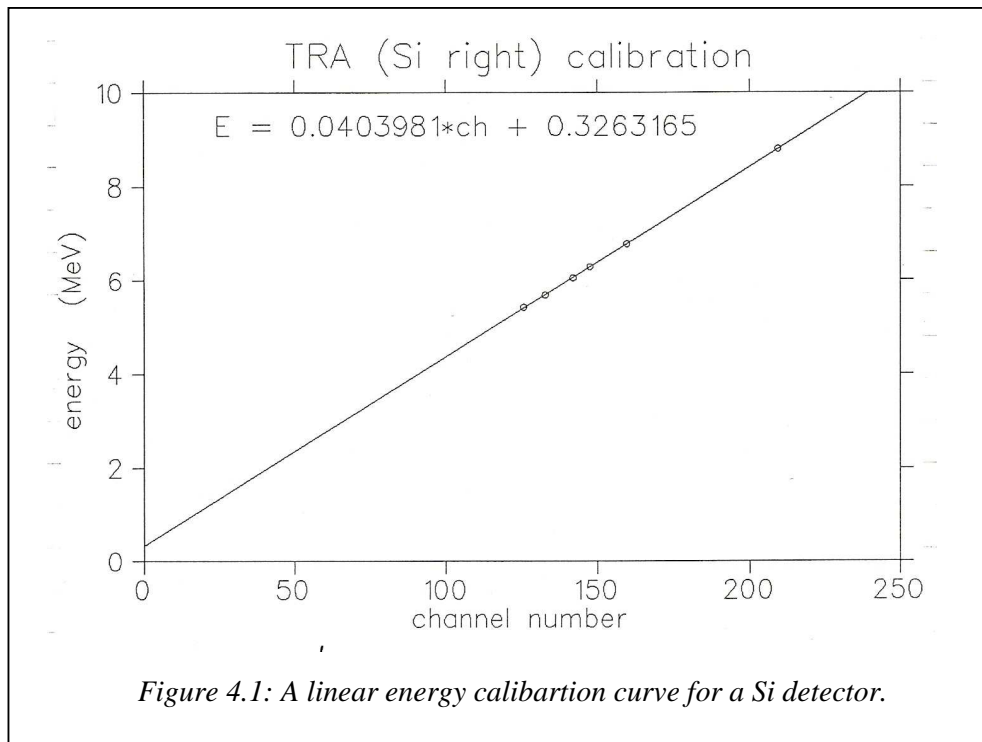
4.2 Energy Calibrations

4.2.1 Silicon detectors (ΔE)

As was mentioned earlier, the silicon (Si) detectors were calibrated with a radioactive ^{228}Th source that emitted α -particles. The calibration was conducted in the scattering chamber with the Si detectors in place and the ^{228}Th source positioned in close proximity. The chamber was pumped to a vacuum of about 1 mbar and bias voltage was applied to the Si detectors. An α -energy spectrum was then recorded in each of the Si detectors. The nuclide ^{228}Th and its decay products emit α -particles with energies of 5.34 MeV, 5.42 MeV, 5.68 MeV, 6.05 MeV, 6.29 MeV, 6.78 MeV and 8.78 MeV. Calculations with the computer program ELOSS showed that α -particles with energies of 8.78 MeV are stopped in only 57 μm of silicon. The

500 μm Si detectors were therefore thick enough to absorb all the energy of the α -particles from the ^{228}Th source.

A least-square linear fit was made between the peaks recorded in the spectrum and the known energies of the α -particles. *Figure 4.1* shows a typical Si detector calibration curve. In *figure 4.1*, however, the linear tendency of the calibration data points does not extrapolate to the origin of the graph. Channel zero corresponds to a small energy value, which means that low electronic noise signals are automatically excluded from the system. Initially, the difference between linear fits with and without the origin amounts to not more than 3% in the energy range of interest.



The calibrations were repeated whenever accidental adjustment to the electronic setup was even remotely possible, such as the period between weekends when the system was unattended. The Si calibration values were stored in the EVAL code and used for energy calibration of the ΔE spectra. The following equations gave the relation between energy E and channel number N ,

$$E_R^{Si} = M_R N_R^{Si} + C_R \quad (4.1)$$

and

$$E_L^{Si} = M_L N_L^{Si} + C_L, \quad (4.2)$$

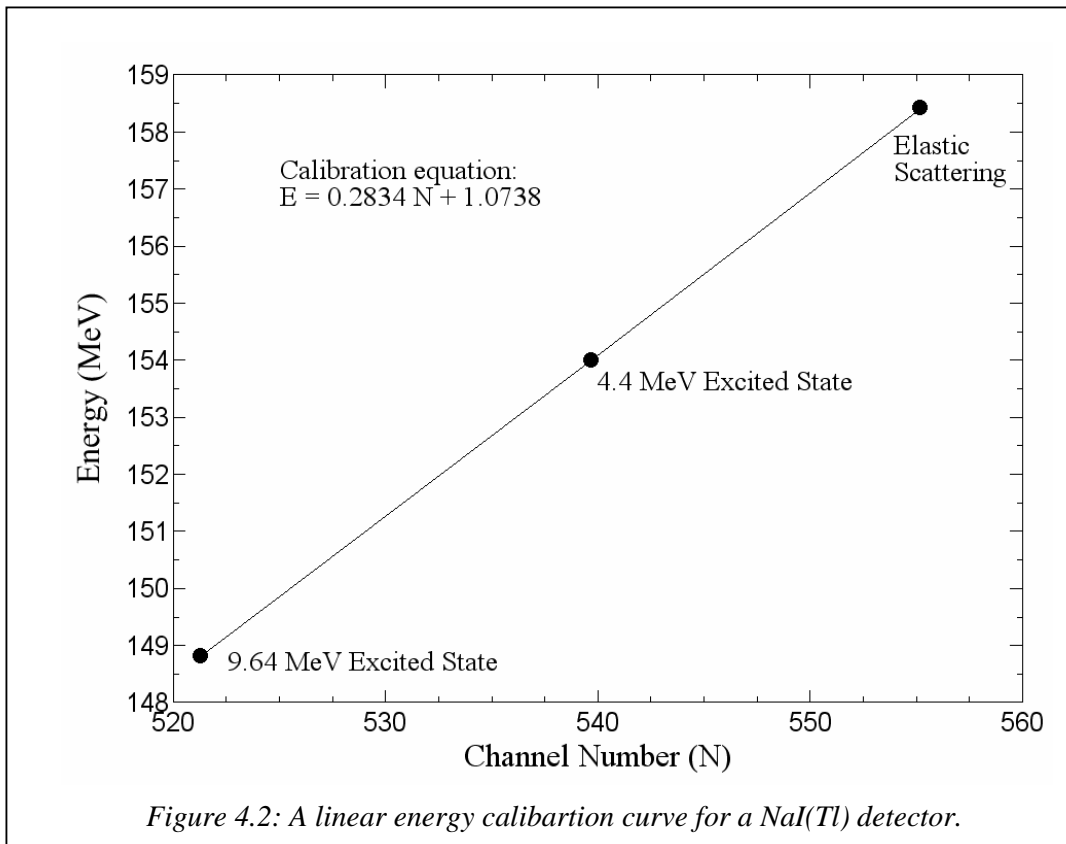
where the subscripts R and L refer to the right and left Si detectors respectively. The calibration constants for the Si detectors for the different weekends are listed in *table 4.A*.

Table 4.A: Calibration constants for the Si detectors.

WEEKEND	M_R	C_R	M_L	C_L
1	0.0397	0.3126	0.0405	0.3470
2	0.0403	0.3242	0.0404	0.3263
3	0.0403	0.3242	0.0404	0.3263
4	0.0403	0.3242	0.0404	0.3263
5	0.0405	0.3391	0.0409	0.3646

4.2.2 NaI(Tl) detectors (E)

The NaI(Tl) detectors (sodium iodide crystal detectors) were calibrated by means of elastic and inelastic proton scattering from a ^{12}C target. The energies of the scattered protons were calculated with the kinematics computer program KINMAT. Energy calibration calculations were based on (p, p) elastic scattering on ^{12}C and (p, p') inelastic scattering to the 4.4 MeV and 9.64 MeV excited states. The calibrations were done at arbitrary lab angles of 24.5° and 19.5° for the 130 MeV and 160 MeV incident beams respectively. Energy loss of the protons due to the 0.008 mm kapton foil ($\text{C}_{22}\text{H}_{10}\text{N}_2\text{O}_5$), the 0.5 mm Si detector and the 0.007 mm havar (An alloy of mainly Co, Cr and Ni) entrance window of the NaI(Tl) detectors were taken into account.



The channel numbers of the elastic and inelastic peaks were plotted as a function of these calculated energies (See *figure 4.2*). A least-square linear fit was performed on the data and this provided the energy calibration parameters for the NaI(Tl) detectors. In the computer code EVAL, the calibrations were treated as linear and the energy E associated with each channel number N was determined with the following equations,

$$E_R^{NaI} = G_R N_R^{NaI} + K_R \quad (4.3)$$

and

$$E_L^{NaI} = G_L N_L^{NaI} + K_L, \quad (4.4)$$

for the right and left NaI(Tl) detectors respectively. In the calibration equations G 's and K 's represent the slopes and the intercepts respectively. Of course the calibration relies only on fairly high energies and the origin was not taken into account when fitting the linear curve. The difference between linear fits with and without the origin included amounts to less than 4%, depending on the actual energy. The calibration is most accurate at high energies where differences of the order of 1% are prevalent. The calibration was repeated at the beginning of

each weekend and whenever excessive gain drift was detected. The calibration values of the NaI(Tl) detectors for the different weekends are tabled in *Table 4.B*.

Table 4.B: Calibration constants for the NaI(Tl) detectors.

WEEKEND	BEAM ENERGY (MEV)	ANGLE (°)	G_R	K_R	G_L	K_L
1	130	25.0	0.3269	-1.7789	0.3023	7.8602
1	130	24.5	0.3281	-3.1099	0.2975	8.4691
1	130	24.5	0.3270	-2.7909	0.3014	6.7817
1	130	25.0	0.3270	-2.4113	0.2994	7.3900
1	130	24.5	0.3248	-1.9133	0.2930	9.6084
2	130	24.5	0.3247	-2.4355	0.3071	5.0376
2	130	24.5	0.3202	-1.2485	0.3081	4.6741
3	130	24.5	0.3304	-4.4063	0.2913	-0.7889
4	160	19.0	0.3442	-10.8860	0.2834	1.0738
5	130	24.5	0.3293	-3.5305	0.2861	-0.2935
5	130	24.5	0.3293	-3.6624	0.2844	0.3392

4.3 Particle Identification

While propagating in a medium, charged particles like alphas and helions lose energy through Coulomb interactions with the orbital electrons within the absorber atoms. The energy loss of a primary particle in an absorber depends mainly on the charge and the velocity of that particle. The relationship between energy loss and the charge and velocity of a particle can be expressed by the Bethe formula [Kno89]

$$-\frac{dE}{dx} = \frac{4\pi e^2 q^2}{m_e v^2} N Z \left[\ln \frac{2m_e v^2}{I} - \ln \left(1 - \frac{v^2}{c^2} \right) - \frac{v^2}{c^2} \right], \quad (4.5)$$

where m_e and e represent the mass and the charge of an electron respectively, q and v represent the charge and velocity of the primary particle respectively, and N and Z represent the number density and atomic number of the absorber. The quantity I represents a parameter for the average excitation and ionization potential of the absorber. For nonrelativistic

charged particles ($v \ll c$), only the first term in the square brackets is significant. This means that different amounts of energy are lost in a medium by particles with the same velocity, but different charge.

If $v \ll c$ the Bethe formula (*equation 4.5*) that describes the energy loss of a particle in a medium can be rewritten as

$$-\frac{dE}{dx} \approx k \frac{m q^2}{E}, \quad (4.6)$$

where m represents the mass, q the charge and E the energy of the incident particle. From *equation 4.6* it is clear that the energy loss of a particle in a medium also demonstrates a dependency on the mass of that particle. This in turn results in different energy loss responses of particles with the same total energy and charge, but with different masses (like alphas and helions).

In the experiment particles were observed in the ΔE - E telescopes, consisting of Si (ΔE) and NaI(Tl) (E) detectors. Particles lost a fraction of their energy in the Si detector which was thinner than the thickness that would stop energetic particles and the remainder was deposited in the NaI(Tl) detector. By plotting the energy loss in the Si detector as a function of the energy loss in the NaI(Tl) detector for each telescope, particle identification spectra (PID's) were obtained (see *figure 3.7*). As a result different particles appear in different loci on the spectrum. An example of a PID from the experiment with the loci of the different particles is illustrated in *figure 4.3* (The plot is such that only helion and alpha particles are clearly visible). By choosing a software gate around the particles of interest (in this experiment helions), they could be singled out for further analysis.

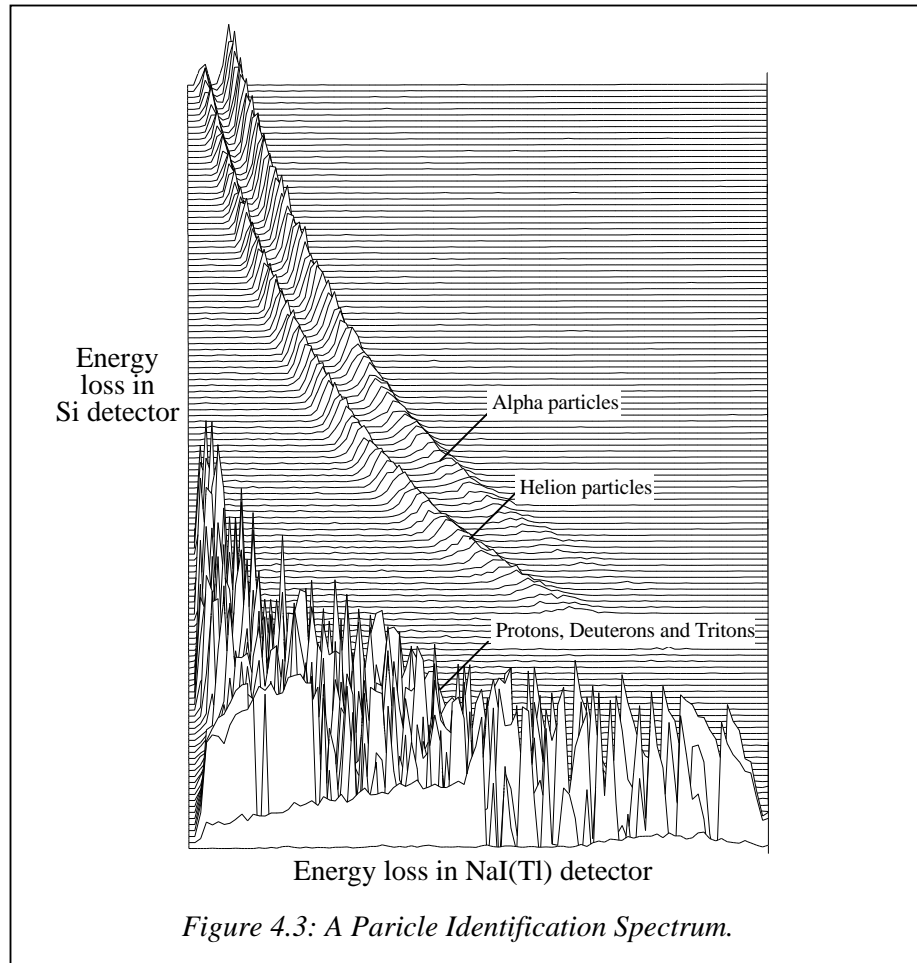


Figure 4.3: A Particle Identification Spectrum.

4.4 Projection Spectra

Although spectra as shown in *figure 4.3* could have been used directly to extract particles of interest, it was more convenient to generate a mass function first. The mass function M for each telescope is calculated from the energies in the different elements of the telescope by using the expression [Eng74]

$$M = (E_{Total}^Y - E_{NaI}^Y)X + Z, \quad (4.7)$$

where E_{Total} represents the total energy measured in the telescope and E_{NaI} the energy measured only in the NaI(Tl) detector. The constants X , Y and Z are chosen and varied to enhance the separation of the loci of the different scattered particles. The mass function is then plotted against the energy measured in the NaI(Tl) detector. An example of such a mass

energy spectrum is illustrated in *figure 4.4*. In this mass-energy spectrum the two loci of the alpha and helion particles are clearly visible. On this spectrum a gate is visible around the particles in the upper locus (alpha particles) in order to extract them for further analysis. The lower locus is that of the helion particles.

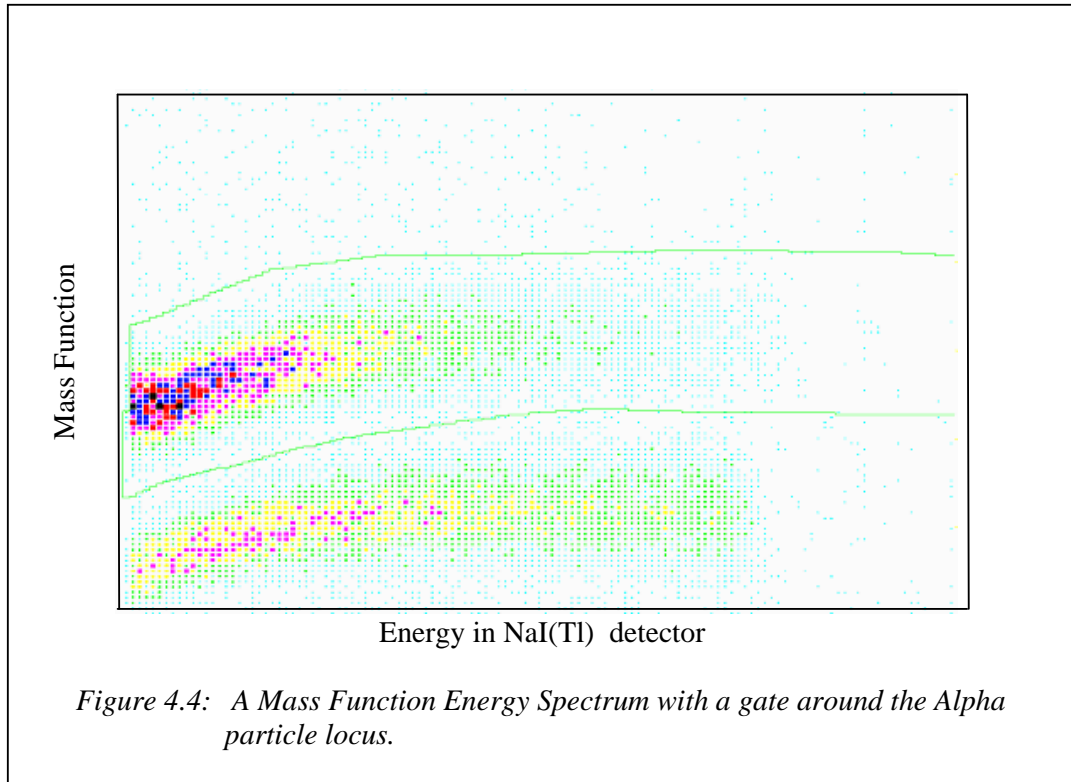


Figure 4.4: A Mass Function Energy Spectrum with a gate around the Alpha particle locus.

The experimental double differential cross section at different scattering angles was determined from the energy spectra corresponding to the selected helions which fall inside the gated mass-energy spectra. The differences in counts in the spectra of the left and right telescopes were used to construct experimental analysing power energy distributions, as will be explained later in this chapter.

4.5 Experimental Data Corrections

4.5.1 Gain Drift

The NaI(Tl) detectors are susceptible to gain drift which can adversely affect the experimental measurements described in this work. As will now be discussed, precautions and procedures have to be implemented to correct for gain drifts. A NaI(Tl) detector unit consists of a scintillation crystal on which a photo multiplier tube is assembled. When a

particle enters the crystal and deposits its energy a small light signal develops. In the photomultiplier tube the light signal generates electrons through the photoelectric process when it impinges on a photocathode. The electrons are then multiplied by means of a dynode chain by a factor of up to 10^6 times to provide a measurable electric pulse [Kno89]. The energy of the particle, the light signal and the electric pulse are roughly linearly proportional to one another. This approximately linear relationship is determined by calibrating the detector as described before.

Due to a number of reasons photomultiplier tubes are subject to significant gain drift, resulting in a change in the calibration values of the detector [Leo94]. To address the problem of gain drift a Light Emitting Diode (LED) was imbedded in the scintillation crystal. The LED was then triggered by a pulser. The LED signal (pulser signal) was recorded in a separate spectrum by the EVAL code. The peak that was recorded at the beginning of a weekend was used as a reference point. If the initial peak associated with the pulser signal shifted during the weekend, the EVAL code automatically and continuously corrected the energy signals of the NaI(Tl) detectors by multiplying with a correction factor. The calibration of the NaI(Tl) detectors was also repeated between experimental target runs if the gain drift was significant.

4.5.2 Reaction Tail Corrections

The process of scintillation that determines the energy of a particle that enters a NaI(Tl) detector relies on Coulomb interactions with the electrons of the atoms in the crystal of the detector. A particle however propagates a distance before stopping in the crystal, while losing energy to the electrons. Before the particle stops some nonelastic nuclear reactions can also occur. The reactions can include those in which neutrons do not deposit energy in the detector as a result of interaction with electrons, or reactions where the Q-value takes up energy from the particle. In these nuclear reactions the energy of the incident particle decreases through processes where scintillation does not occur and therefore full energy detection does not take place. The consequence of this is that the total energy of the particle is not measured in the NaI(Tl) detector and this part of the recorded spectrum is referred to as the reaction tail. Usually corrections have to be made for particles that are not collected in the full peak due to the reaction tail.

As we will now explain, the required reaction tail corrections are not as large for helions as for lighter ions, such as protons. The quadratic relationship between energy loss and charge demonstrated in *equation 4.6*, results in particles with higher charge losing energy much more quickly in a crystal than those with lower charge. Consequently particles with higher charge will also have smaller stopping distances in the crystal than particles with less charge. This results in helion and alpha particles ($m=3, 4$ and $Z=2$) having significantly smaller stopping distances than protons ($m=1$ and $Z=1$), deuterons ($m=2$ and $Z=1$) and tritons ($m=3$ and $Z=1$) [Seg82]. The probability for helion and alpha particles to be involved in nonelastic nuclear interactions is therefore also much smaller in spite of reaction cross sections that could be roughly of the same order of magnitude. As a result the energy loss due to reaction tail processes for helions and alphas are so small ($< 2\%$) [Seg82, Mea66] that corrections in this study were unnecessary.

4.6 Double Differential Cross Section

As mentioned earlier the double differential cross section at different scattering angles was calculated from the counts in the energy spectra. The double differential cross section (in $\text{mb.MeV}^{-1}.\text{sr}^{-1}$) is given by

$$\frac{d^2\sigma}{d\Omega dE} = \frac{10^{27}}{\Delta\Omega \Delta E} \cdot N_c \cdot \frac{1}{N_0} \cdot \frac{1}{\rho}, \quad (4.8)$$

where

N_c is the corrected number of counts in an energy bin,

$\Delta\Omega$ is the solid angle in sr covered by a ΔE -E telescope,

ΔE is the width of the energy bins in MeV,

N_0 is the total number of protons incident on the target, given by

$$N_0 = \frac{10^{-12}}{e_p} \cdot C \cdot R, \quad (4.9)$$

where

C is the integrated charge measured by the current integrator when the data acquisition is inhibited by a busy signal,

R is the selected range in nA which represents $R.1000$ counts per second for the full scale current readout,

e_p is the charge of a proton in Coulomb,

ρ is the number of nuclei per unit area of target nucleus in cm^{-2} and is given by

$$\rho = \frac{N_A}{A} \cdot \frac{\lambda}{\cos \theta_T}, \quad (4.10)$$

where

λ is the target thickness in g/cm^2 ,

N_A is Avogadro's number,

A is the atomic mass of the target in g/mol ,

θ_T is the angle of the target's normal with respect to the beam line.

The statistical error σ_s on each of the energy bins is given by [Kno89]

$$\sigma_s = \sqrt{N}, \quad (4.11)$$

where N is the number of counts per bin. The statistical error for the double differential cross section can therefore be written as

$$\sigma_s = \frac{10^{27}}{\Delta\Omega\Delta E} \cdot \sqrt{N_c} \cdot \frac{1}{N_0} \cdot \frac{1}{\rho}. \quad (4.12)$$

These equations were used to calculate the spin-up and spin-down double differential cross sections and the statistical errors associated with them. The absolute double differential cross section $d^2\sigma_0$ was then calculated by [Bez00]

$$d^2\sigma_0 = \frac{d^2\sigma_{\uparrow} + d^2\sigma_{\downarrow}}{2 + A_y(p_{\uparrow} - p_{\downarrow})}, \quad (4.13)$$

where $d^2\sigma_{\uparrow}$ and $d^2\sigma_{\downarrow}$ represents the spin-up and spin-down double differential cross sections respectively. The quantity A_y represents the analysing power of the reaction, and p_{\uparrow} and p_{\downarrow} represent the polarisation of the beam in the spin-up and spin-down orientations respectively. As $p_{\uparrow} - p_{\downarrow}$ is generally small (about 0.1; see *table 4.D*) and $A_y \leq 1$, the absolute double differential cross section is within a few percent of the average of the spin-up and spin-down values. The absolute double differential cross section was therefore estimated as the average between the spin-up and spin-down double differential cross sections. The equivalent approximation was made for the statistical error. The absolute statistical error $\sigma_{\uparrow\downarrow}$ was therefore estimated with

$$\sigma_{\uparrow\downarrow} = \sqrt{\sigma_{\uparrow}^2 + \sigma_{\downarrow}^2}, \quad (4.14)$$

where σ_{\uparrow} and σ_{\downarrow} represented the statistical errors for the counts in the spin-up and spin-down orientation respectively.

4.7 Analysing Power

4.7.1 Measurement of the Incident Polarisation

The polarisation of the incident proton beam was measured with the aid of the ^{12}C target in the target ladder. The two $\Delta\text{E-E}$ detectors are placed at the same angle θ_p to the left and to the right of the incident beam. The two detectors then measured the number of events when the beam was in the spin-up and spin-down orientations respectively (see *figure 2.4* for an explanation of the orientations). Four values were thus measured by the detector, being the spin-up left L_{\uparrow} , spin-up right R_{\uparrow} , spin-down left L_{\downarrow} and spin-down right R_{\downarrow} .

A polarisation run was repeated regularly (usually every two hours) during the experiment, by means of an elastic scattering reaction on ^{12}C . The analysing power of this reaction at the different beam energies and selected angles is given in *table 4.C*.

Table 4.C: Analysing power of the elastic $^{12}\text{C}(p,p')$ reaction at selected angles and energies.

BEAM ENERGY (MeV)	ANGLE (θ_p) ($^{\circ}$)	A_y
130	24.5	0.86 [Mey83]
160	19.0	0.94 [Mey83]

The values for polarisation-up p_{\uparrow} and polarisation-down p_{\downarrow} can then be calculated from the following equations [Hae74]

$$p_{\uparrow} = \frac{\mathcal{E}_{\uparrow}}{A_y}, \quad (4.15)$$

where

$$\varepsilon_{\uparrow} = \frac{L_{\uparrow} - R_{\uparrow}}{L_{\uparrow} + R_{\uparrow}} \quad (4.16)$$

and

$$p_{\downarrow} = \frac{\varepsilon_{\downarrow}}{A_y}, \quad (4.17)$$

where

$$\varepsilon_{\downarrow} = \frac{L_{\downarrow} - R_{\downarrow}}{L_{\downarrow} + R_{\downarrow}}. \quad (4.18)$$

The average percentage values for the beam polarisation during the experiment are given in *table 4.D*.

Table 4.D: The Average Beam Polarisations for the different weekends.

WEEKEND	BEAM ENERGY (MeV)	POLARISATION-UP (%)	POLARISATION-DOWN (%)
1	130	75.5 ± 2	68.2 ± 2
2	130	77.5 ± 2	64.1 ± 2
3	130	82.4 ± 2	67.8 ± 2
4	160	80.3 ± 2	68.8 ± 2
5	130	75.6 ± 2	73.3 ± 2

4.7.2 Analysing Power Calculations

A relationship between analysing power and beam polarisation can be found by rewriting *equation 2.60* as

$$A_y = \frac{\sigma_L(\theta) - \sigma_R(\theta)}{p^{inc} (\sigma_L(\theta) + \sigma_R(\theta))}, \quad (4.19)$$

where A_y represents the analysing power of the reaction, p^{inc} the polarisation of the incident beam and $\sigma_R(\theta)$ and $\sigma_L(\theta)$ the cross section measurements of the detectors to the right and to the left of the beam line respectively. During the experimental runs the incident beam was alternated between the polarisation-up and polarisation-down orientations. The experimental set-up also comprised of two detectors, one detector to right and one detector left of the beam

line. The relationship between polarisation-up p_{\uparrow} , the analysing power A_y and counts in the left C_L and the right C_R detectors can then be expressed as [Hae74]

$$C_L^{\uparrow} = K_{\uparrow} \alpha_L (1 + p_{\uparrow} A_y) \quad (4.20)$$

and

$$C_R^{\uparrow} = K_{\uparrow} \alpha_R (1 - p_{\uparrow} A_y). \quad (4.21)$$

The factor K represents all the quantities that are common to the detectors and the factor α represent the efficiency of each detector. The quantities common to both detectors can include the cross section σ_0 (see *equation 4.8*), the number of incident particles (see *equation 4.9*) and the target thickness (see *equation 4.10*). By combining the equations for polarisation-up (*equation 4.20* and *4.21*) with the equations for polarisation-down the following expression for the analysing power is derived

$$A_y = \frac{1}{(p_{\downarrow} + p_{\uparrow})} \frac{(C_L^{\uparrow} - C_L^{\downarrow}) + (C_R^{\downarrow} - C_R^{\uparrow})}{C_L^{\uparrow} + C_R^{\uparrow}}, \quad (4.22)$$

Haeberli [Hae74] also derived an equation for the analysing power under the conditions that $p = p_{\uparrow} = p_{\downarrow}$ and expressed it as

$$A_y = \frac{1}{p} \left(\frac{r-1}{r+1} \right), \quad (4.23)$$

where

$$r = \sqrt{\left(\frac{C_L}{C_R} \right)_{\uparrow} \cdot \left(\frac{C_R}{C_L} \right)_{\downarrow}}. \quad (4.24)$$

Similar to the previous equations C_L and C_R represent the counts for the left and the right detectors and the polarisation-up and polarisation-down orientations is indicated by \uparrow or \downarrow respectively. Haeberli [Hae74] emphasised that this approximation ($p_{\uparrow} \approx p_{\downarrow}$) should only be used if the value $\delta = \frac{1}{2}(p_{\uparrow} - p_{\downarrow})$ is small and provided the following equation to estimated the error that arises in p ,

$$p = \frac{1}{A_y} \left(\frac{r-1}{r+1} \right) \left[1 - \frac{(r-1)^2}{4r} A_y^2 \delta^2 + \dots \right]. \quad (4.25)$$

Haeberli stated that for example for $\delta = 0.1$ the error in p is less than 0.01 if $|pA_y| \leq 0.6$.

For comparison purposes calculations for the analysing power were done with both *equations 4.22 and 4.23*. No significant difference were found between the analysing power results of these equations, even when the polarisation-up and polarisation-down had differences of up to 13% (see *table 4.D*, weekend 2). Thus the differences between the polarisation-up and polarisation-down (listed in *table 4.D*) were not large enough ($p_{\uparrow} \approx p_{\downarrow}$) to motivate a preference between *equations 4.22 and equation 4.23* in the final calculation of the analysing power. Consequently *equation 4.22* was used to calculate the analysing power for the final results.

If $p_{\uparrow} \approx p_{\downarrow}$ the statistical error for the analysing power σ_{A_y} can be determined by [Ste97]

$$\sigma_{A_y} = A_y \left[\left(\frac{r}{r^2 - 1} \right)^2 \cdot \left(\frac{1}{C_L^{\uparrow}} + \frac{1}{C_R^{\downarrow}} + \frac{1}{C_R^{\uparrow}} + \frac{1}{C_L^{\downarrow}} \right) + \left(\frac{\sigma_p}{p} \right)^2 \right]^{\frac{1}{2}}, \quad (4.26)$$

where the p represents the average polarization and C the counts. The quantity r is given by *equation 4.28* and σ_p represents the error on the beam polarisation measurement (less than 1%). The experimental analysing power results in *Chapter 6* include the statistical errors indicated on the graphs with error bars.

4.8 Systematic Errors

The systematic errors that influenced the double differential cross section are listed in the table below (*table 4.E*). The combined errors for the differential cross section in this study are estimated to be in the order of 10%. These systematic errors are compared with those from previous studies for which roughly comparable conditions existed. The linear sum of the errors is a number associated with the unrealistic situation where the different errors conspire to give a maximum value.

Table 4.E: Systematic errors that affect the differential cross section.

SOURCES OF SYSTEMATIC ERRORS	MAGNITUDE OF THE ERRORS (%)	MAGNITUDE OF THE ERRORS FROM REFERENCES (%)
Target thickness	7	7 [Are94], 8 [Ste97]
Target angle	< 1	< 1 [Ste97]
Detector telescope solid angle	1.6	1.2-1.5 [Nev01], 2 [Whi89, Ste97]
Particle identification	5	5 [För92], 3 [Whi89]
Electronic dead time	2 – 5	2 [För92], 4 [Whi89]
Energy Calibrations	3 – 4	4 [Ste97, För92]
Current integrator uncertainty	< 1	0.5 [Nev01], 0.2 [För92], < 1 [Ste97]
Linear Sum	~ 24	
Total Systematic Error	~ 10	8 [Whi89], ~ 9 [För92, Ste97]

The symmetry in the detector arrangement decreased the systematic error when analysing power is determined. The result is that most of the systematic errors do not have an influence on the experimental analysing power data. The systematic errors that influenced the analysing power are listed in the table below (*table 4.F*)

Table 4.F: Systematic errors that affect the Analysing Power.

SOURCES OF SYSTEMATIC ERRORS	MAGNITUDE OF THE ERRORS (%)
Particle identification	5
Energy Calibrations	3 - 4
Linear Sum	~ 8
Total Systematic Error	~ 6

Only the particle identification errors and calibration errors needed to be taken into account when analysing power was investigated. This results in a combined systematic error of ~6% for the experimental analysing power measurements.

Chapter 5: THEORETICAL CALCULATIONS

5.1 Overview

The theoretical background described in *Chapter 2* provides all the formulations that underlie the theory of this study. In this chapter the implementation of these formulations into actual calculations to produce theoretical predictions are described. All the programs and methods which were used to obtain the final theoretical results are described. Certain approximations also needed to be introduced, verified and tested, and these are also discussed.

In the first section the multistep pickup computer codes are described. The next section discusses how the intermediate double differential cross section values for multisteps were obtained. In section 5.4 the optical model potentials which were applied to the entrance and exit channels are explained. The last section concludes with an explanation of the density distributions of the ejectile and residual nuclei.

5.2 Multistep Reaction Pickup Codes

The Pickup Multistep Program of Demetriou [Dem96], as modified by Dimitrova [Dim96], which is based on the statistical multistep pickup theory of Feshbach, Kerman and Koonin [Fes80] was used for all the calculations of theoretical double differential cross sections and analysing powers. The Pickup Multistep Code consists of three FORTRAN subroutines namely, PMS.FOR [Dem96, Dim96], DWUCK4.FOR [Kun93] and MOPHE3.FOR [Kat98]. The interaction of these programs with each other is as follows:

The code PMS.FOR (PMS) reads all input quantities from the input file INPUTM. The code then calls the subroutine SHELL where all the possible shell model states for the intermediate nucleus are calculated. The PMS code then determines all the combinations of incident and emission energies, referred to as $C(E_{in}, E_{out})$, needed for the convolution calculations of the multistep double differential cross section. Subsequently the PMS code selects the deuteron transfers from all possible combinations of nuclear states for each of the excitation energies. For each of these deuteron transfers the PMS code calls the subroutine WRITED which creates the input file (FORT.5) as input for DWUCK4.FOR (DWUCK4). The subroutine OPTICAL, called from WRITED, allocates the parameters for the global optical potential

between the target nucleus and a proton. This can be the incident proton (p) or the first step proton (p') or the second step proton (p''). The imaginary parameters and scaling factors for the potential between the residual nucleus and the helion (exit channel) are taken from the input file, INPUTM. The double folding potential and a phenomenological process are used to determine the parameters for the exit channel. This process is discussed in *section 5.4.2*.

The PMS code then repeatedly calls the subroutine DWUCK4 to calculate double differential cross sections and analysing powers for all possible deuteron transfers and combinations of energies $\{C(E_{in}, E_{out})\}$. In DWUCK4 the program MOPHE3.FOR (MOPHE3) is called as a subroutine to calculate the double folding potential between the helion particle and the residual nucleus. After the double differential cross sections for all the possible combinations of energies were calculated by the DWUCK routines, the PMS code calls the subroutine MULTISTEP. In this routine all the combinations of energies within the number of chosen steps are determined.

Final double differential cross sections and analysing powers for one step, two step and three step processes can be calculated. In the input files (PPSTEPS) double differential cross section values for the intermediate stage reactions (p, p') and (p, p', p'') are listed as a function of scattering angle and emission energy. MULTISTEP reads the double differential cross sections for the intermediate stages from these input files (PPSTEPS) and merges them with the calculated values to determine the final theoretical values. The final double differential cross section and analysing power values are written to the output file, OUTPUT. *Figure 5.1* shows a flow chart of the interaction between the different codes.

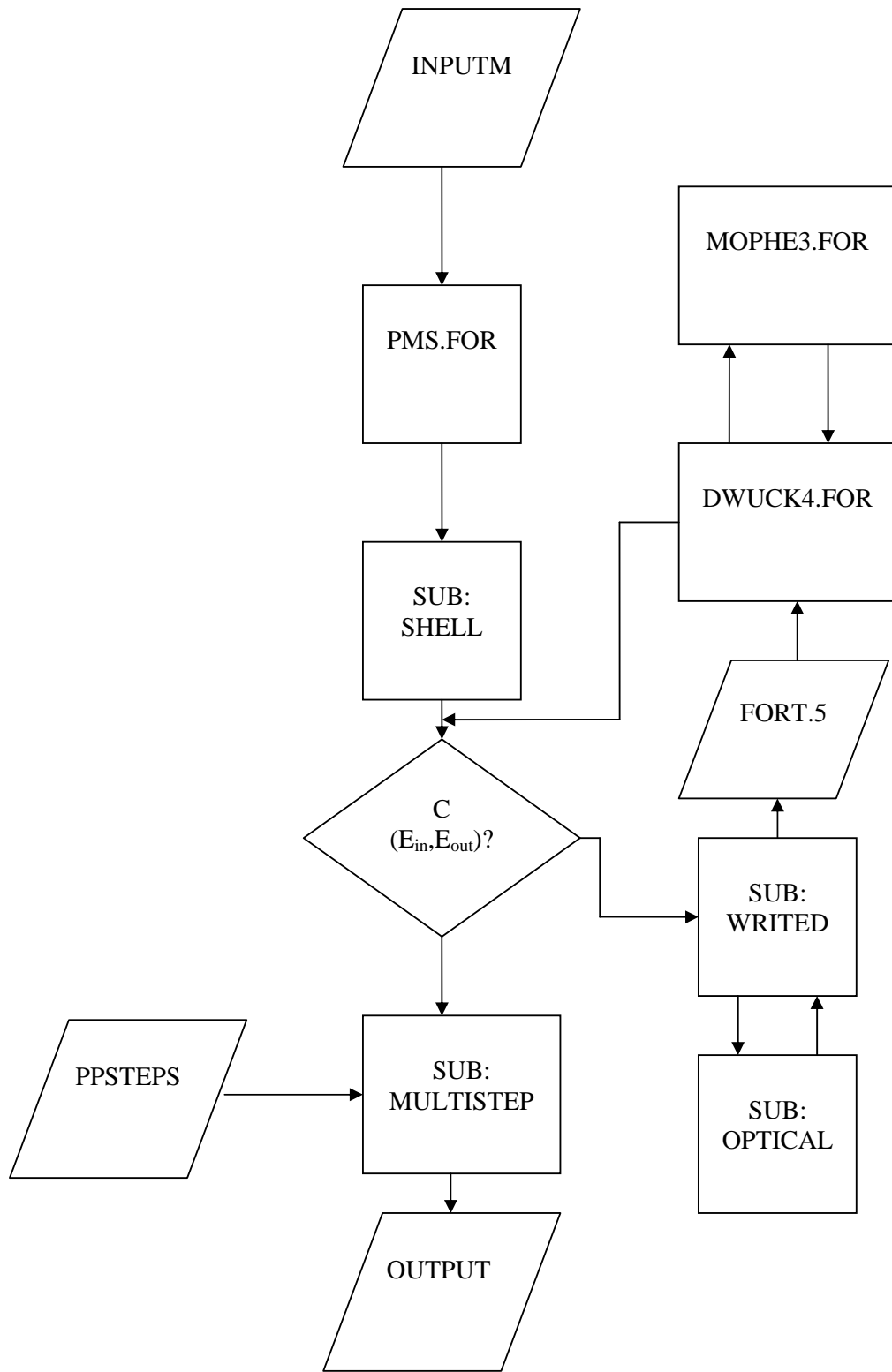


Fig 5.1: Flow chart of the Multistep Pickup Code.

5.3 Intermediate Double Differential Cross Section Values

The multistep calculations were done for one step ($p, {}^3\text{He}$), two step ($p, p', {}^3\text{He}$) and three ($p, p', p'', {}^3\text{He}$) step reactions (see *figure 2.1*). The double differential cross sections of all the possible combination of energies $\{C(E_{\text{in}}, E_{\text{out}})\}$ and shell model states for the ($p, {}^3\text{He}$) reaction were calculated by DWUCK4. If the cross section for a two step reaction ($p, p', {}^3\text{He}$) is calculated, the cross section of the first step (p, p') of the reaction must be known. Similarly if the cross section for a three step ($p, p', p'', {}^3\text{He}$) reaction is calculated the cross section of the first (p, p') and second step (p', p'') have to be known. Cross sections were generated for these intermediate steps and used in the multistep reaction calculations. These cross sections were tabled in the input file PPSTEPS and used in the subroutine MULTISTEP to calculate the final cross section values. Various methods were used and tested to calculate the double differential cross section values for these intermediate steps and some of these methods are discussed in the following paragraphs.

5.3.1 Intermediate double differential cross section values for the ${}^{59}\text{Co}(p, {}^3\text{He})$ reaction

Richter *et al.* used the FKK theory to calculate double differential cross sections for a one step (p, p') and a two step (p, p', p'') intermediate reaction with ${}^{58}\text{Ni}$ as target [Ric92]. This was done at incident energies of 120 MeV, 160 MeV and 200 MeV. A third order interpolation between these energies was made to obtain the intermediate one and two step double differential cross section values at an incident energy of 130 MeV. These intermediate double differential cross section values for ${}^{58}\text{Ni}$ at 130 MeV were used in the calculations for ${}^{59}\text{Co}$ as target. No changes were made to the ${}^{58}\text{Ni}$ intermediate double differential cross section values when they were used in the ${}^{59}\text{Co}$ calculations. This was done because nuclei with similar mass numbers like ${}^{58}\text{Ni}$ and ${}^{59}\text{Co}$ do not exhibit substantial variation in double differential cross section over a range of varying energy [Ric92].

5.3.2 Intermediate double differential cross section values for the ${}^{93}\text{Nb}(p, {}^3\text{He})$ reaction

The intermediate double differential cross section tables which were derived for the ${}^{59}\text{Co}(p, {}^3\text{He})$ multistep reaction were also used in the multistep calculations of the

$^{93}\text{Nb}(p, ^3\text{He})$ reaction. The form of the angular distribution of the double differential cross section for a (p, p') reaction at a specific emission energy does not change appreciably from lighter target nuclei (for example ^{59}Co) to heavier target (for example ^{93}Nb) nuclei. As would be expected, a change in the magnitude of the double differential cross section is observed as a function of target mass. For example the experimental double differential cross section values for the (p, p') reaction on ^{58}Ni , ^{92}Mo and ^{197}Au are plotted in *figure 5.2* [Ric92]. The increase in the magnitude of the double differential cross section as a function of target mass roughly follows the reaction cross section for protons [Jac05]. Based on these results, an adjustment to obtain the correct absolute magnitude was done by multiplying the intermediate cross section values for ^{59}Co by a factor when calculations for the $^{93}\text{Nb}(p, ^3\text{He})$ reaction were done. In other words all the calculations for the $^{93}\text{Nb}(p, ^3\text{He})$ reaction were therefore derived from the intermediate double differential cross section tables of the $^{59}\text{Co}(p, ^3\text{He})$ reaction.

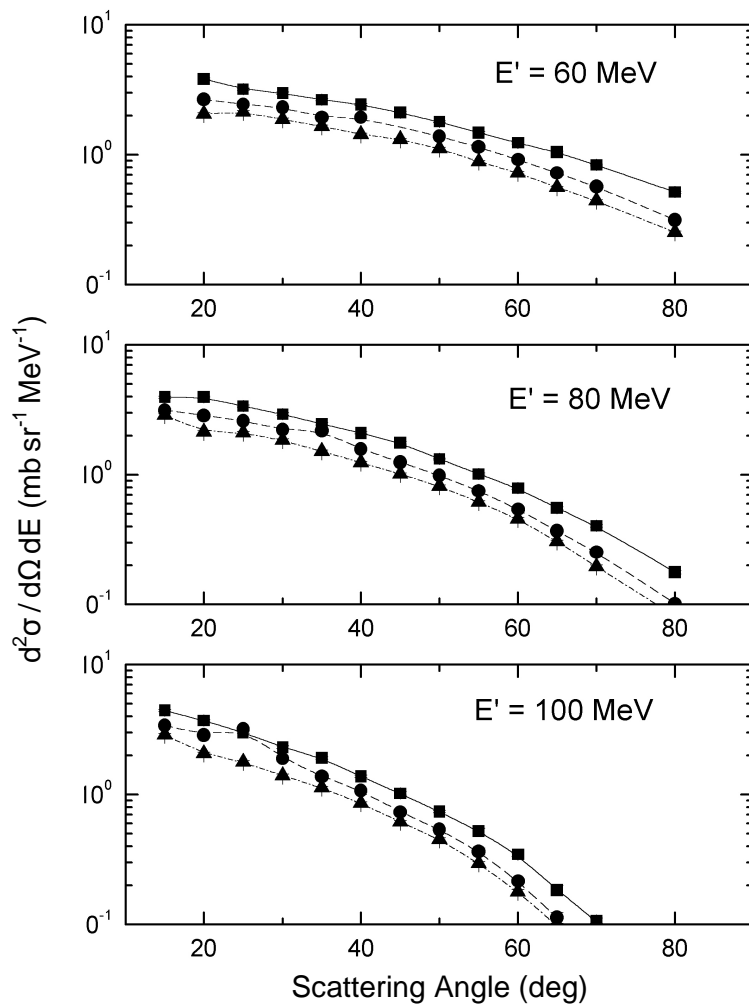


Figure 5.2: Angular cross section distributions for (p, p') reactions on ^{58}Ni (\blacktriangle), ^{100}Mo (\bullet) and ^{197}Au (\blacksquare) at an incident energy 120 MeV and emission energies E' as indicated [Ric92]. The lines through the experimental cross section data serve to guide the eye.

5.4 Optical Model Parameter Sets

5.4.1 The potential used for the entrance channel

In all the theoretical calculations involving ^{59}Co and ^{93}Nb as target nuclei the global optical proton-nucleus potentials of Madland and Schwandt [Mad88, Sch82] was used, because these potentials describe elastic proton scattering in a large range of target masses and incident energies very accurately.

5.4.2 The optical model parameters used for the exit channel

Calculations by Cowley *et al.* [Cow97] of the $(p, ^3\text{He})$ double differential cross section showed an unreasonable sensitivity to the optical model potential parameters between the helion and residual nucleus and finding an appropriate set presented a problem. This difficulty was overcome by using the double folding model (see *section 2.4*) to calculate the real part of the optical potential of the exit channel [Cow00]. The imaginary part of the potential was taken to be of the Woods-Saxon form, given by *equation 2.7*. The parameters of the imaginary part of the potential were determined in a phenomenological manner. The complete potential can be written as

$$V^{DF}(r) = F_c U_c^{DF}(r) + F_{so} U_{so}^{DF}(r) \vec{L} \cdot \vec{S} + iW(r), \quad (5.1)$$

where $U_c^{DF}(r)$ and $U_{so}^{DF}(r)$ are the central and spin-orbit part of the potential and $W(r)$ is the imaginary part of the potential. The real central and spin-orbit parts of the folded potential were rescaled by the factors F_c and F_{so} respectively. The parameters for the imaginary part of the potential and scaling factors which fitted the experimental double differential cross section data the best are tabulated in *table 5.A*. The parameters of the imaginary optical potential have a strong linear dependence on the incident energy of the reaction. This dependence is evident in the parameters of both residual nuclei (^{57}Fe and ^{91}Zr).

Table 5.A: The scaling factors and imaginary optical potential parameters.

Target	Energy (MeV)	F_c	F_{so}	W (MeV)	R (fm)	a (fm)
⁵⁹ Co	100	1	1	95	1.5	0.6
	130	1	1	60	1	0.3
	160	1	1	30	1	0.2
⁹³ Nb	100	0.5	25	35	1.5	0.6
	130	0.5	25	10	1	0.3

This dependence is clearly illustrated in *figure 5.3* where the volume integrals of the imaginary optical parameters of the ³He potential are plotted as a function of incident energy. It is obvious from *figure 5.3* that the volume integrals of the different nuclei (⁵⁹Co and ⁹³Nb) follow similar trends at 100 MeV and 130 MeV and both vary systematically with the incident energy. Although the incident proton energy, and its wave function should be unrelated to the ³He potential to first order, the observed relationship is reasonable if one keep in mind that we determine the latter by requiring a good fit to data at low excitation energy, in other words we use the range where the one-step mechanism dominates to extract the imaginary potential. Thus we implicitly also emphasise a value of the ³He energy which varies with incident energy. Clearly the energy variation of the ³He imaginary optical potential implies that this needs to be taken into account at each value of the incident energy as the emission energy varies. Due to lack of theoretical guidance this has been ignored in this work.

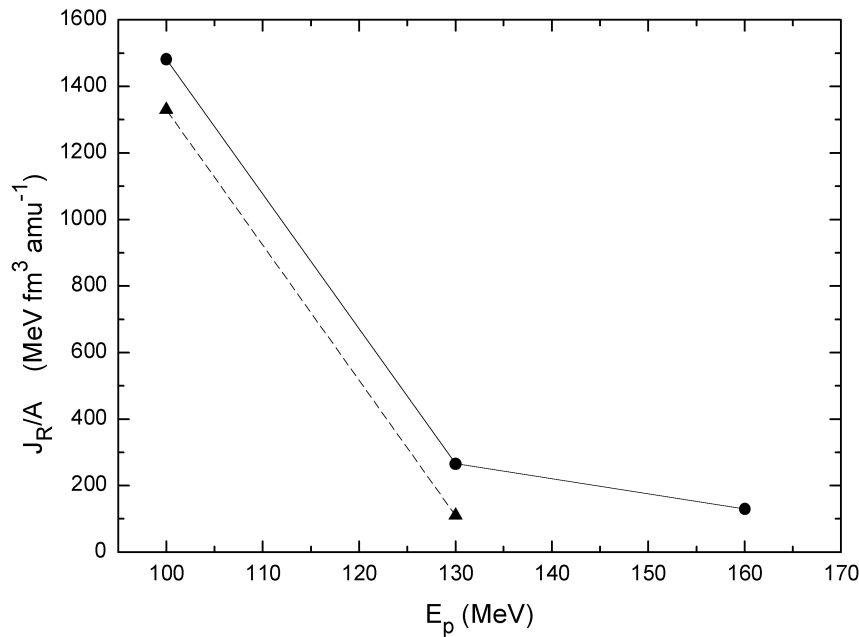


Figure 5.3: The volume integral value calculated with the imaginary optical potential parameters for the exit channel of ^{59}Co (—) and ^{93}Nb (----) as function of incident energy. The value for ^{93}Nb was multiplied by a factor of 5 to assist with display.

5.5 Density Distributions

Density distributions for both the residual nuclei and the helions were needed to calculate the real part of the double folding potential (equation 2.67). These density distributions for the different residual nuclei, calculated by Stoitsov [Sto04] by means of the Hartree-Fock-Bogoliubov (HFB) theory, were read into the subroutine MORPHE3 from the input file. The internal structure of the helion was taken as a simple $1s1p$ harmonic oscillator shell model wave function. The density distribution for helions then reduced to a single Gaussian form with range parameters extracted from electron scattering data [Sak98]. These relative densities as a function of nuclear radius are plotted in figure 5.4 for both the ^{57}Fe and the ^{91}Zr nuclei.

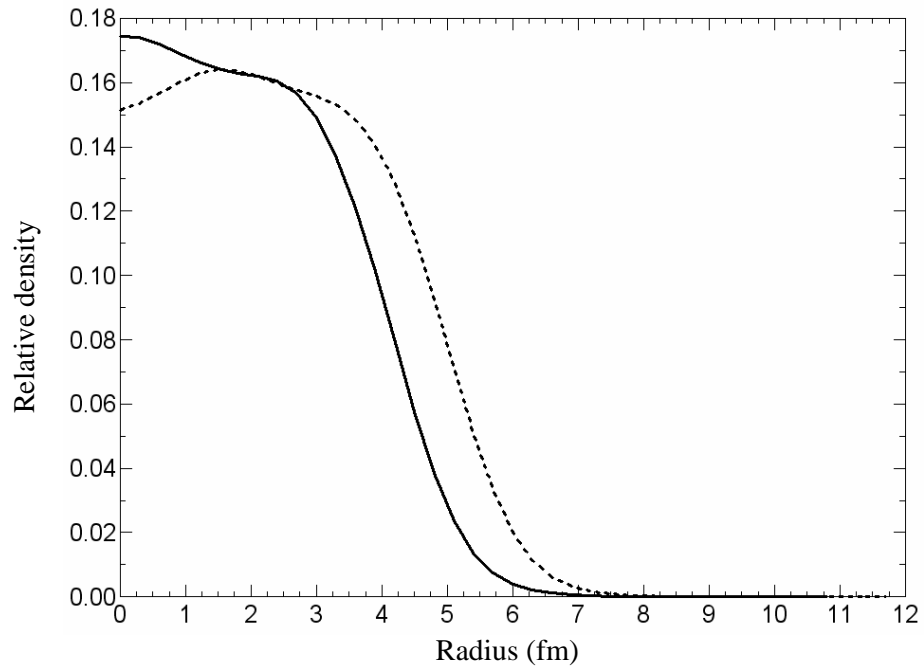


Figure 5.4: The relative density distributions that were used for the ^{57}Fe (—) and the ^{91}Zr (----) nuclei. These distributions were obtained from Stoitsov [Sto04].

Chapter 6: RESULTS

6.1 Overview

In this chapter, the experimental and theoretical analysing power and cross section results are presented and deductions are made about the validity of the assumed reaction mechanism. Previously Cowley *et al.* [Cow00] investigated $^{93}\text{Nb}(\bar{p}, ^3\text{He})$ and $^{59}\text{Co}(\bar{p}, ^3\text{He})$ reactions at an incident energy of 100 MeV. However, that study indicated a need to investigate this reaction at higher incident energies in order to explore the expected change in analysing power towards 200 MeV, as was found by Renshaw *et al.* [Ren91]. In order to ensure that the data in the complete energy interval between 100 MeV and 160 MeV are treated consistently by the theory, the data for $^{93}\text{Nb}(\bar{p}, ^3\text{He})$ and $^{59}\text{Co}(\bar{p}, ^3\text{He})$ at 100 MeV [Cow00] are re-analysed in this work.

In the first section the phenomenological parameterisation of double differential cross section of Kalbach [Kal88] is presented. A comparison is made between the experimental double differential cross section data and calculated values of the Kalbach parameterisation to confirm that the data behave as predicted by known systematic trends. The second section investigates the double differential cross section and analysing power in combination. In this description specific reference is made to the steps in the reactions and the importance of the contribution of each step to the final values of the analysing power and cross section. The next section discusses the multistep theoretical predictions of the double differential cross sections and the comparison with experimental results. The theoretical and experimental results for the analysing power are subsequently discussed.

6.2 Phenomenological Parameterisation of Kalbach

The calculations utilising the phenomenological parameterisation of Kalbach [Kal88] were compared with the experimental double differential cross section data. Kalbach found that the double differential cross section and the scattering angle for any pre-equilibrium reaction were primarily related to one another simply by a slope η . This slope is largely determined by the ratio between the energies of the incident and scattered particles. The relationship

between the double differential cross section and the scattering angle θ can be expressed as [Kal88]

$$\frac{d^2\sigma}{d\Omega dE_{^3\text{He}}} = \frac{1}{4\pi} \left(\frac{d\sigma}{dE_{^3\text{He}}} \right) \frac{\eta}{\sinh \eta} \exp(\eta \cos \theta), \quad (6.1)$$

for a direct reaction process. The energy differential cross section $\left(\frac{d\sigma}{dE_{^3\text{He}}} \right)$ is equal to the angular integrated yield of ^3He , which we adjust to fit the magnitude of the angular distribution. We included this factor into the normalisation factor when we apply the expression to the experimental data. The slope η , which is a function of the incident energy E'_p and the emission energy $E'_{^3\text{He}}$, includes the mentioned energy ratio X and is given by

$$\eta(E'_{^3\text{He}}, E'_p) = 0.04E_1X + 1.8 \times 10^{-6}(E_1X)^3 + 6.7 \times 10^{-7} M_p m_{^3\text{He}} (E_3X)^4, \quad (6.2)$$

with

$$X = E'_{^3\text{He}} / E'_p,$$

$$E'_{^3\text{He}} = E_{^3\text{He}} + S_{^3\text{He}},$$

$$E'_p = E_p + S_p,$$

$$E_1 = \min(E'_p, 130 \text{ MeV}),$$

$$E_3 = \min(E'_p, 40 \text{ MeV}),$$

$$M_p = 1 \text{ and } m_{^3\text{He}} = 1.$$

The separation energies S_p and $S_{^3\text{He}}$ are obtained from the liquid drop model. For these separation energies the pairing and shell terms of the liquid drop formula are neglected.

Chadwick *et al.* [Cha94] showed that the parameterisation of Kalbach can be explained by applying momentum and energy considerations to a semi classical pre-equilibrium model, with inclusion of the multistep mechanisms. By conserving linear momentum Chadwick *et al.* expressed the emission rate from the n th state as a function of the particle-hole (p and h) density distributions of the n th state nucleus $\rho(p, h, E, \vec{K})$ and the residual nucleus $\rho(p_r, h_r, E - \varepsilon_\Omega, \vec{K} - \vec{k}_\Omega)$, resulting in

$$\frac{d^2 \lambda_n(\Omega, \varepsilon)}{d\Omega d\varepsilon} = \frac{2\mu\varepsilon\sigma_{inv}}{\pi^2 \hbar^3} \frac{\rho(p_r, h_r, E - \varepsilon_\Omega, \vec{K} - \vec{k}_\Omega)}{\rho(p, h, E, \vec{K})}, \quad (6.3)$$

where μ represent the reduced mass of the ejectile, σ_{inv} is the cross section for the inverse process and E and \vec{K} are the total energy and momentum of the system respectively. The energy and momentum of the residual nucleus after emission are given by $E - \varepsilon_\Omega$ and $\vec{K} - \vec{k}_\Omega$ respectively, where ε_Ω and \vec{k}_Ω represent the energy and the momentum of the emitted particle respectively. The particle-hole density ρ of the nuclei can then be expressed in a Gaussian form as (similar to the distribution in *equation 2.46*)

$$\rho(p, h, E, \vec{K}) = \rho(p, h, E) \frac{1}{(2\pi)^{3/2} \sigma^3} \exp(-K^2/2\sigma^2), \quad (6.4)$$

where σ is the momentum cut-off and $\rho(p, h, E)$ represents the state level density in energy space. From the pre-equilibrium emission of a particle with momentum \vec{k}_Ω , the squared absolute value of the residual nucleus momentum is

$$|\vec{K} - \vec{k}_\Omega|^2 = K^2 + k_\Omega^2 - 2Kk_\Omega \cos \theta, \quad (6.5)$$

where θ is the angle of the emission in relation to the projectile direction. By accepting the emission rate to be proportional to the cross section and substituting *equation 6.4* and *equation 6.5* into *equation 6.3*, the following expression results

$$\frac{d^2 \sigma_n(\Omega, \varepsilon)}{d\Omega d\varepsilon} = \frac{d\sigma_n(\varepsilon)}{d\varepsilon} \frac{1}{4\pi} \frac{2a_n}{e^{a_n} - e^{-a_n}} \exp(a_n \cos \theta), \quad (6.6)$$

where $\frac{d\sigma_n(\varepsilon)}{d\varepsilon}$ is the n th stage angle integrated cross section and

$$a_n = \frac{3Kk_\Omega}{2(p_r + h_r)m\varepsilon_{av}}. \quad (6.7)$$

Equation 6.6 is clearly related to the Kalbach double differential cross section (*equation 6.1*) and provides a physics justification for the Kalbach parameterisation.

At incident energies above 100 MeV, and emission energies higher than 30 MeV, the assumption can be made that the nuclear interaction can be described by mainly Multistep Direct (MSD) reaction processes [För92]. Consequently calculations were made by using only the MSD reaction part of the Kalbach equation (as given by *equation 6.1*), while the

Multistep Compound (MSC) part of the equation was neglected [Kal88]. The normalisation process to compare the Kalbach double differential cross section distributions to the experimental double differential cross sections was performed with a chi-square fit. The χ^2 deviation is

$$\chi^2 = \sum_i \left(\frac{x_i - c\mu_i}{\sigma_i} \right)^2, \quad (6.8)$$

where x_i is the experimental double differential cross section, μ_i is given by

$$\mu_i = \frac{n}{\sinh n} e^{n \cos \theta}. \quad (6.9)$$

The value σ_i is the statistical error associated with the experimental double differential cross section and

$$c = \frac{1}{4\pi} \left(\frac{d\sigma}{dE_{\text{He}}} \right). \quad (6.10)$$

The c values were determined by normalising the Kalbach curves to the experimental data. The c values which gave the best agreement between the parameterisation and experimental quantities, are listed in *table 6.A*. Angular distributions comparing the Kalbach parameterisation calculations with experimental double differential cross section for the (\bar{p} , ^3He) reactions at different incident and emission energies and with for both target nuclei, are shown in *figure 6.1*.

Good agreement in shape between the Kalbach calculations and the experimental double differential cross section angular distributions is obtained. The underestimation of the Kalbach curves at angles smaller than 20° at the higher emission energies is an indication of other reaction processes which are neglected, such as a collective excitation of the nucleus. The good agreement between the Kalbach parameterisation values and the experimental double differential cross section distributions serves as an additional unbiased validation of the experimental cross section data and shows that it displays the trend as expected from systematics. The good agreement thus inspires confidence in the integrity of the data.

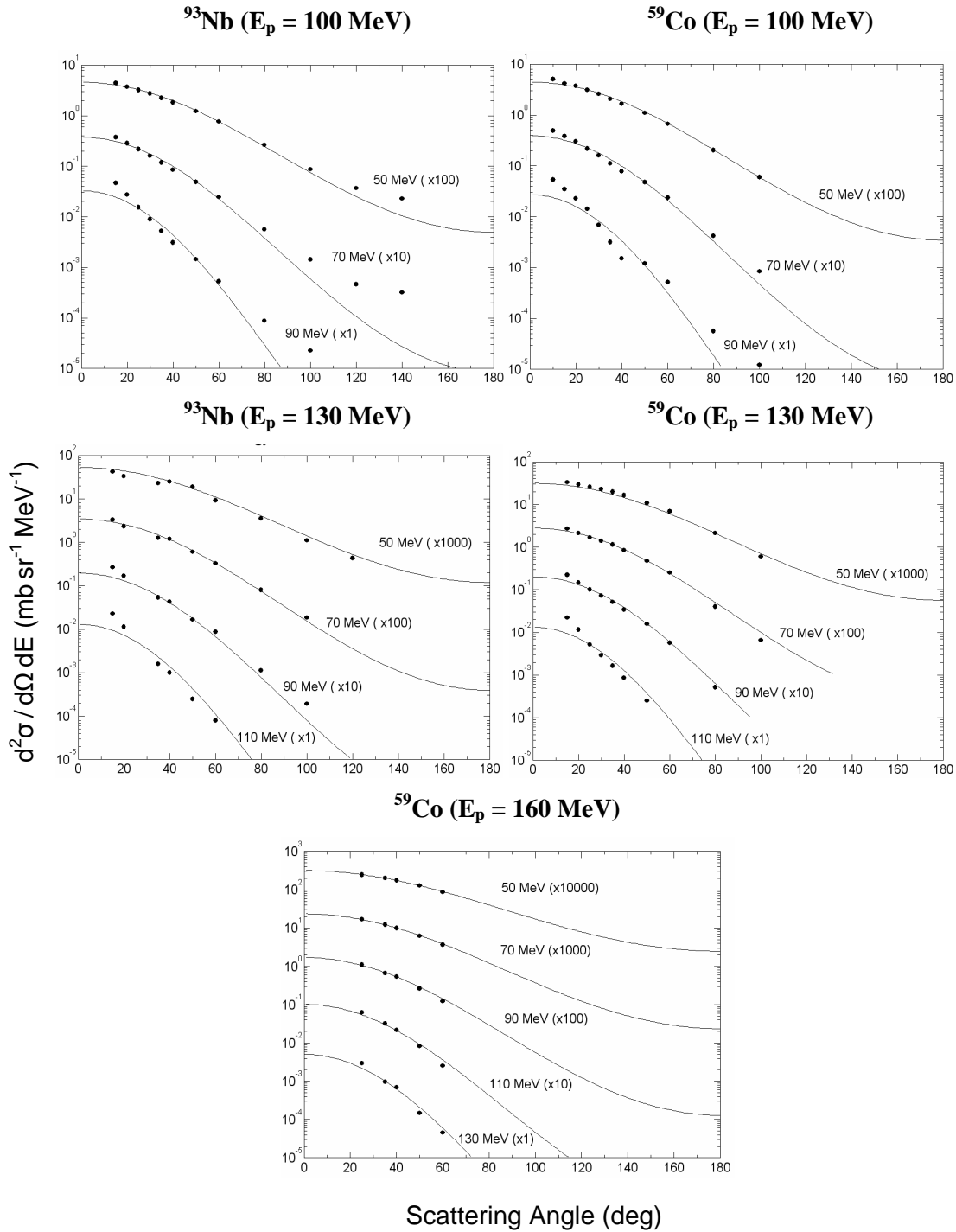


Figure 6.1: Cross section angular distributions for the $(p, ^3\text{He})$ reaction on different target nuclei and at incident and emission energies as indicated. The symbols represent the experimental data and the plots represent the predictions of the phenomenological parameterisation of Kalbach [Kal88].

A clear relationship is evident between the normalisation constants (which are proportional to the integrated yield of the emitted helions) and the emission energy of the helions (see *table 6.A*). The normalisation constants are plotted as a function of the emission energy in *figure 6.2* and an exponential fit is made through the data points (the equation for the fit is indicated on the graph).

Table 6.A: The c values that were applied to the Kalbach curves to fit the experimental data.

Ejected energy (MeV)	100 MeV on ^{93}Nb (mb MeV $^{-1}$)	100 MeV on ^{59}Co (mb MeV $^{-1}$)	130 MeV on ^{93}Nb (mb MeV $^{-1}$)	130 MeV on ^{59}Co (mb MeV $^{-1}$)	160 MeV on ^{59}Co (mb MeV $^{-1}$)
50	6.7×10^{-3}	6.2×10^{-3}	8.7×10^{-3}	5.7×10^{-3}	6.5×10^{-3}
70	3.5×10^{-3}	3.5×10^{-3}	3.8×10^{-3}	3.1×10^{-3}	3.4×10^{-3}
90	2.0×10^{-3}	1.6×10^{-3}	1.8×10^{-3}	1.6×10^{-3}	1.8×10^{-3}
110	-	-	0.6×10^{-3}	0.6×10^{-3}	0.8×10^{-3}
130	-	-	-	-	0.3×10^{-3}

From *figure 6.2* it is evident that the normalisation constants show a strong dependence on the emission energy of the ^3He . The constants for ^{93}Nb are generally higher than those of ^{59}Co indicating a higher probability for helion emission in heavier nuclei as would be expected from the target mass dependence of the reaction cross section. The constants are independent of incident energy for both target nuclei.

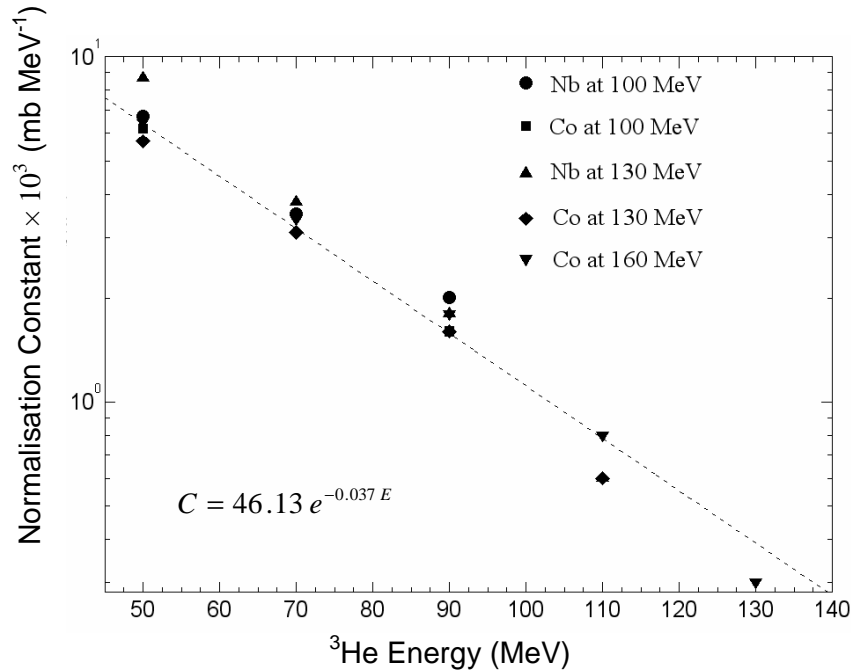


Figure 6.2: The normalisation factors applied to the Kalbach parameterisation as function of the ^3He emission energy. The dashed line is an exponential fit to the values and the equation for this fit is indicated on the graph.

The magnitude of the normalisation constants decreases systematically with an increase in emission energy, for both nuclei (see *figure 6.2*). The observed exponential drop-off of the constants with an increase in emission energy is a typical differential cross section characteristic that was also found for (p, p') reactions on a number of target nuclei by Cowley *et al.* [Cow90].

6.3 Double Differential Cross Section and Analysing Power in terms of Multistep Theory

The comparison of experimental double differential cross sections with the phenomenological Kalbach parameterisation only serves as an indication of consistent systematic trend of the experimental data. A true understanding of the reaction mechanism requires an investigation of the relationship between observables like experimental double differential cross sections and analysing power with formal calculations based on a theoretical model. The theoretical multistep formalism in this study (discussed in *Chapter 2*) assumes a nucleon pair (quasi deuteron) pickup reaction mechanism with a multistep mechanism preceding this pickup. Experimental double differential cross sections and analysing power for the $^{59}\text{Co}(\bar{p}, {}^3\text{He})$ and the $^{93}\text{Nb}(\bar{p}, {}^3\text{He})$ reactions at the incident energies of 100 MeV, 130 MeV and 160 MeV are now compared with the results of these theoretical calculations and are also discussed.

Double differential cross section and analysing power distributions covering the total range of incident and emission energies for both target nuclei (^{59}Co and ^{93}Nb) are compared in *figure 6.3* to *figure 6.7*. Calculations that exhibit the relative importance of the contributions of the first three steps are also plotted on each graph. Because the probability for deuteron formation in the nucleus is not known, the theoretical double differential cross sections were normalised independently to the experimental data and this was done at each incident energy. The normalisation constants were chosen to give the best fit at the complete range of outgoing energies associated with that incident energy.

The magnitude of the double differential cross section at small scattering angles decreases with an increase in incident energy. For comparable low excitation energies the slope of the double differential cross section also increases as the incident energy increases, as would be expected for a single step direct reaction. This indicates a lower probability for helion emission with an increase in incident energy, which is similar to results found by Cowley *et al.* [Cow97]. The opposite is observed at lower incident energies where a higher probability for helion emission is evident, also with a more even spread of the double differential cross section over larger scattering angles. This coincides with an increase in the probability for the multistep reactions (more than one step) at lower incident energies.

In the analysing power graphs the theoretical curves for the single step reaction at low emission energies sometimes show large deviations from zero (see *figure 6.3* and *6.4*). The corresponding double differential cross section curves, however, show that the contribution of the first step in those cases is negligible. Nevertheless, the curves for those one step reactions are sometimes shown even when they clearly do not influence the shape of the distribution at all (for example *figure 6.3* at $E' = 50$ MeV).

At the lowest emission energies the calculations regularly underestimate the double differential cross section data. This might merely be due to the way in which the normalisation was done for each incident energy and could be resolved by adjusting the normalisation constants. However, we believe that the observed trend is more likely explained as the influence of more than three steps, which was not included in the calculations. This underestimation is however of no concern because the inclusion of these higher steps will have no effect on the analysing power; the analysing power at high excitation energies is already close to zero.

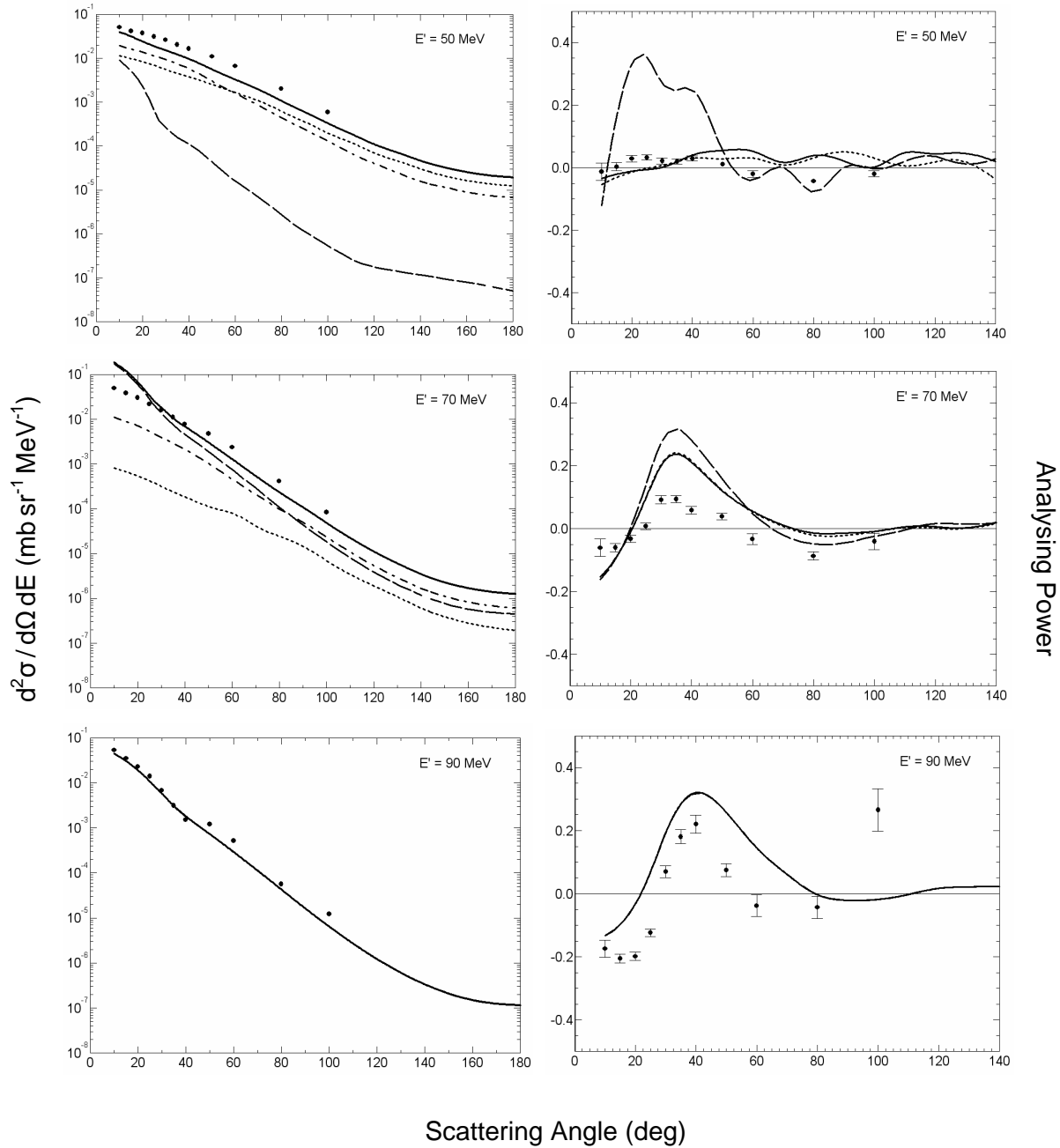


Figure 6.3: Double differential cross section and analysing power as a function of scattering angle for $^{59}\text{Co}(\bar{p}, {}^3\text{He})$ at an incident energy of 100 MeV and emission energies as indicated. The experimental double differential cross section data are compared with theoretical calculations for one step (— — —), two step (- · - · -) and three step (····) contributions. The sum of the first three steps is indicated with a continuous curve. The experimental analysing power data are compared with theoretical calculations for a one step reaction (— — —), a one step plus a two step reactions (····) and a one step plus a two step plus a three steps reaction (indicated with a continuous curve).

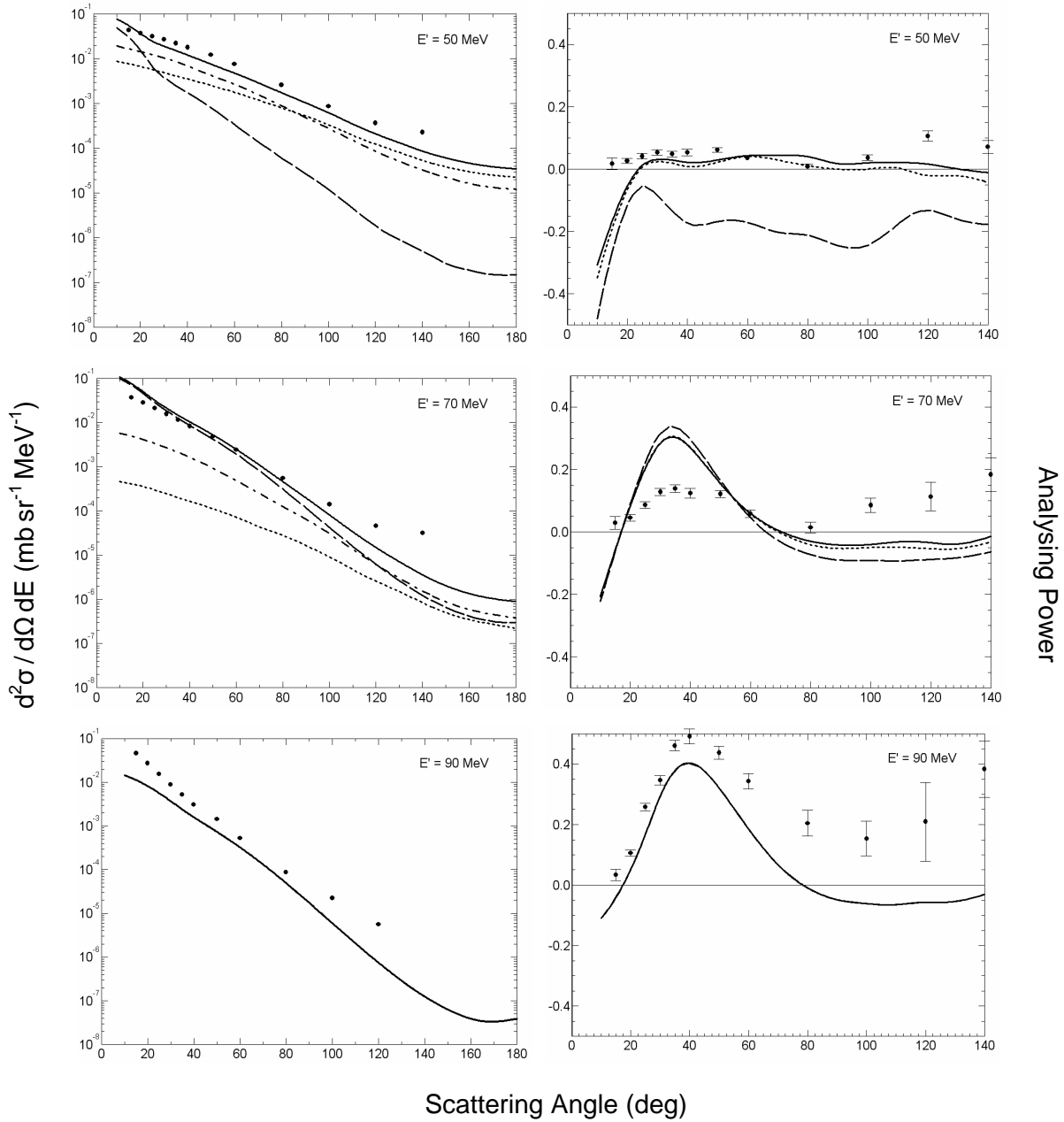


Figure 6.4: Analysing power and double differential cross section as a function of scattering angle for $^{93}\text{Nb}(\bar{p}, ^3\text{He})$ at an incident energy of 100 MeV and emission energies as indicated. The experimental data are compared with theoretical calculations for one, two and three step reactions. For other details also see the caption to figure 6.3.

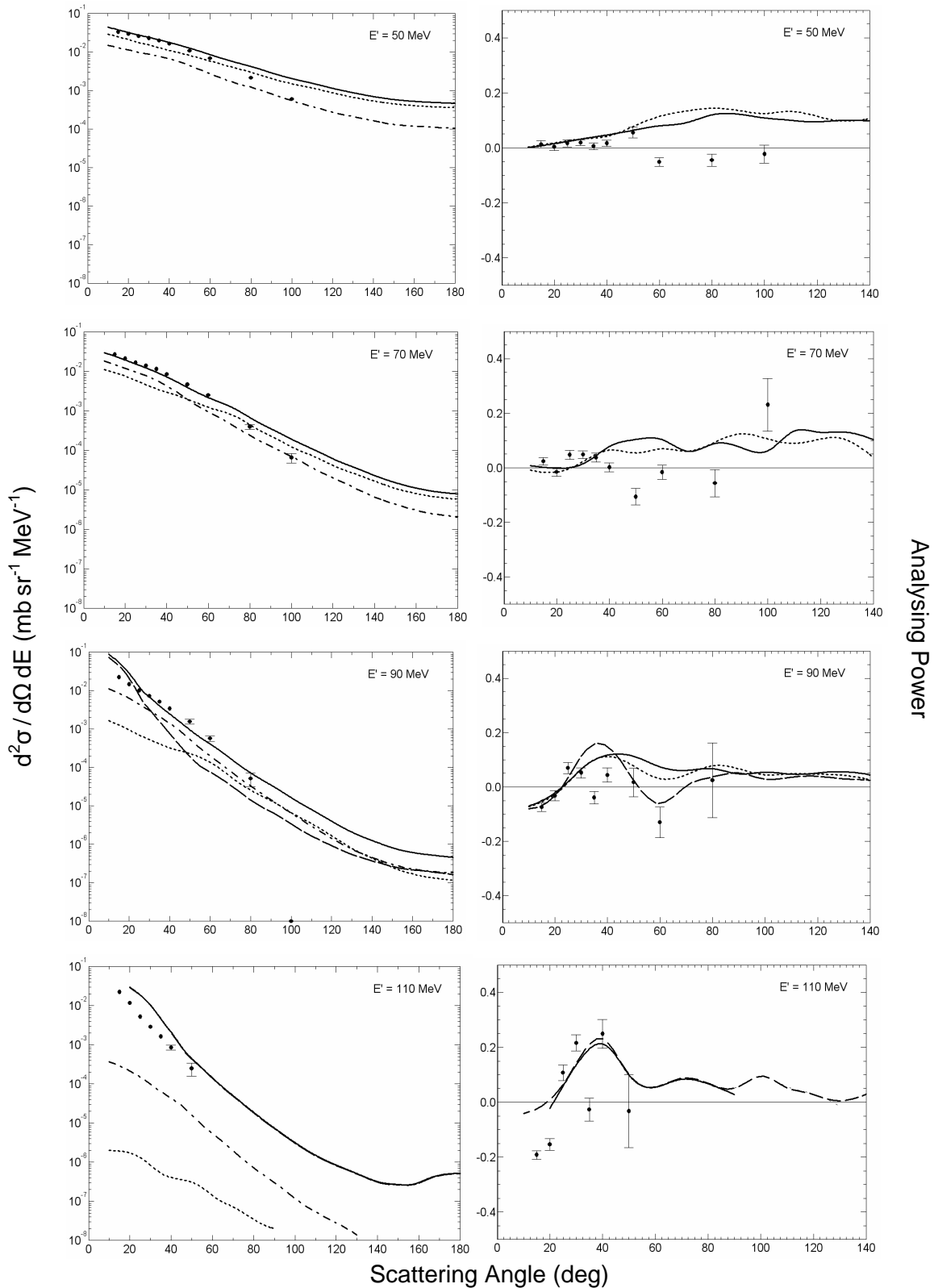


Figure 6.5: Analysing power and double differential cross section as a function of scattering angle for $^{59}\text{Co}(\bar{p}, {}^3\text{He})$ at an incident energy of 130 MeV and emission energies as indicated. The experimental data are compared with theoretical calculations for one, two and three step reactions. For other details also see the caption to figure 6.3.

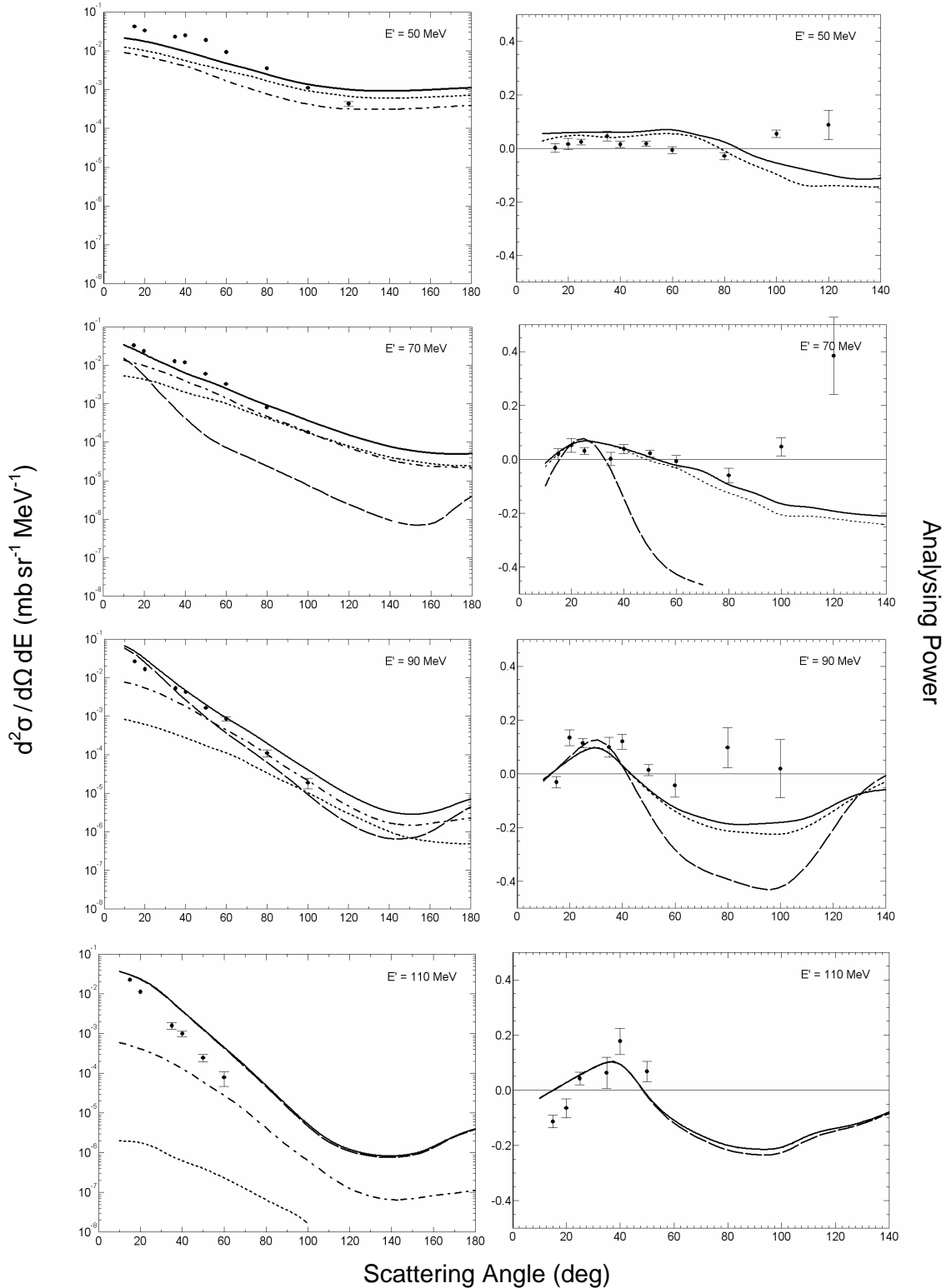


Figure 6.6: Analysing power and double differential cross section as a function of scattering angle for $^{93}\text{Nb}(\bar{p}, {}^3\text{He})$ at an incident energy of 130 MeV and emission energies as indicated. The experimental data are compared with theoretical calculations for one, two and three step reactions. For other details also see the caption to figure 6.3.

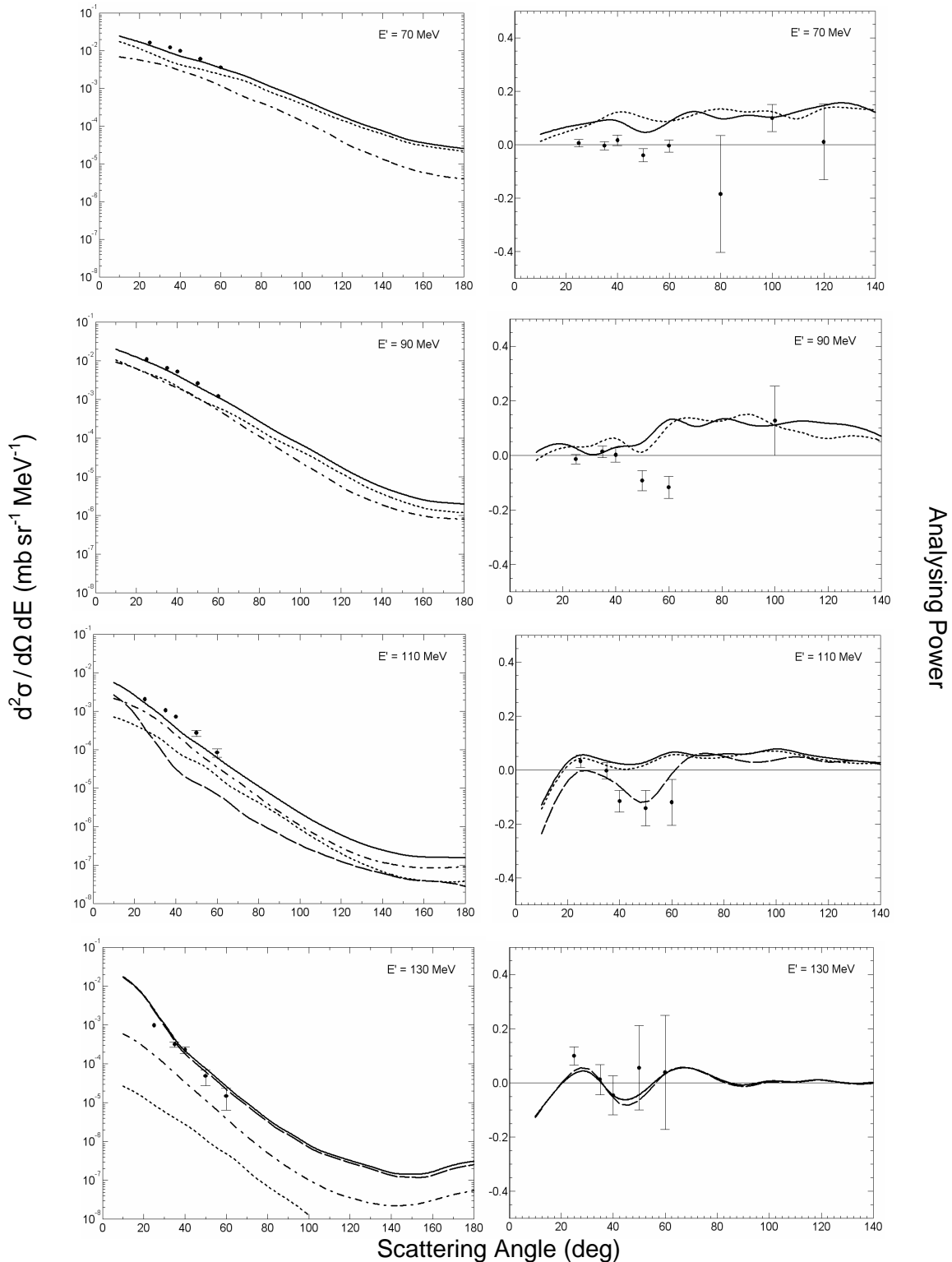


Figure 6.7: Analysing power and double differential cross section as a function of scattering angle for $^{59}\text{Co}(\bar{p}, {}^3\text{He})$ at an incident energy of 160 MeV and emission energies as indicated. The experimental data are compared with theoretical calculations for one, two and three step reactions. For other details also see the caption to figure 6.3.

6.4 Features of the Double Differential Cross Section Angular Distributions

The relationships between the $(\bar{p}, {}^3\text{He})$ double differential cross section distributions and a number of variable conditions are discussed in the following subsections. In this section we emphasise features that are illustrated best by the properties of the cross section distributions.

6.4.1 Dependence of the double differential cross section on target nucleus

The double differential cross sections for the reactions ${}^{93}\text{Nb}(\bar{p}, {}^3\text{He})$ and ${}^{59}\text{Co}(\bar{p}, {}^3\text{He})$ at an incident energy of 130 MeV are shown in *figure 6.8* in order to compare the relationship between the double differential cross section for different target nuclei. The experimental and theoretical double differential cross sections for ${}^{93}\text{Nb}$ as well as for ${}^{59}\text{Co}$ agree well in shape at all emission energies. However, the cross sections for ${}^{93}\text{Nb}$ are consistently higher than those for ${}^{59}\text{Co}$, as was already pointed out it is expected due to increase in reaction cross section with larger target mass. This is better illustrated in *figure 6.9* where, for clarity of representation, only experimental data are shown.

In the *figure 6.9* the slopes of the curves increase with an increase in emission energy. This is in agreement with the expected relationship between the slope η and the emission energy, discussed earlier. The forward peaked double differential cross section is as a result of a dominance of the single step direct reaction mechanism at low excitation energies. This dominance of the single step reactions is also clearly illustrated in *figure 6.8* where excitation energies are low.

Subtle differences between the double differential cross sections of the different target nuclei are evident in comparing the contribution of the different steps towards the final double differential cross section. When an emission energy of 60 MeV is reached the first step for both target nuclei is negligibly small. The third step however contributes more to the total double differential cross section in ${}^{59}\text{Co}(\bar{p}, {}^3\text{He})$ than for ${}^{93}\text{Nb}(\bar{p}, {}^3\text{He})$ at larger angles. This characteristic is evident at emission energies of 60 MeV and 80 MeV in *figure 6.8*.

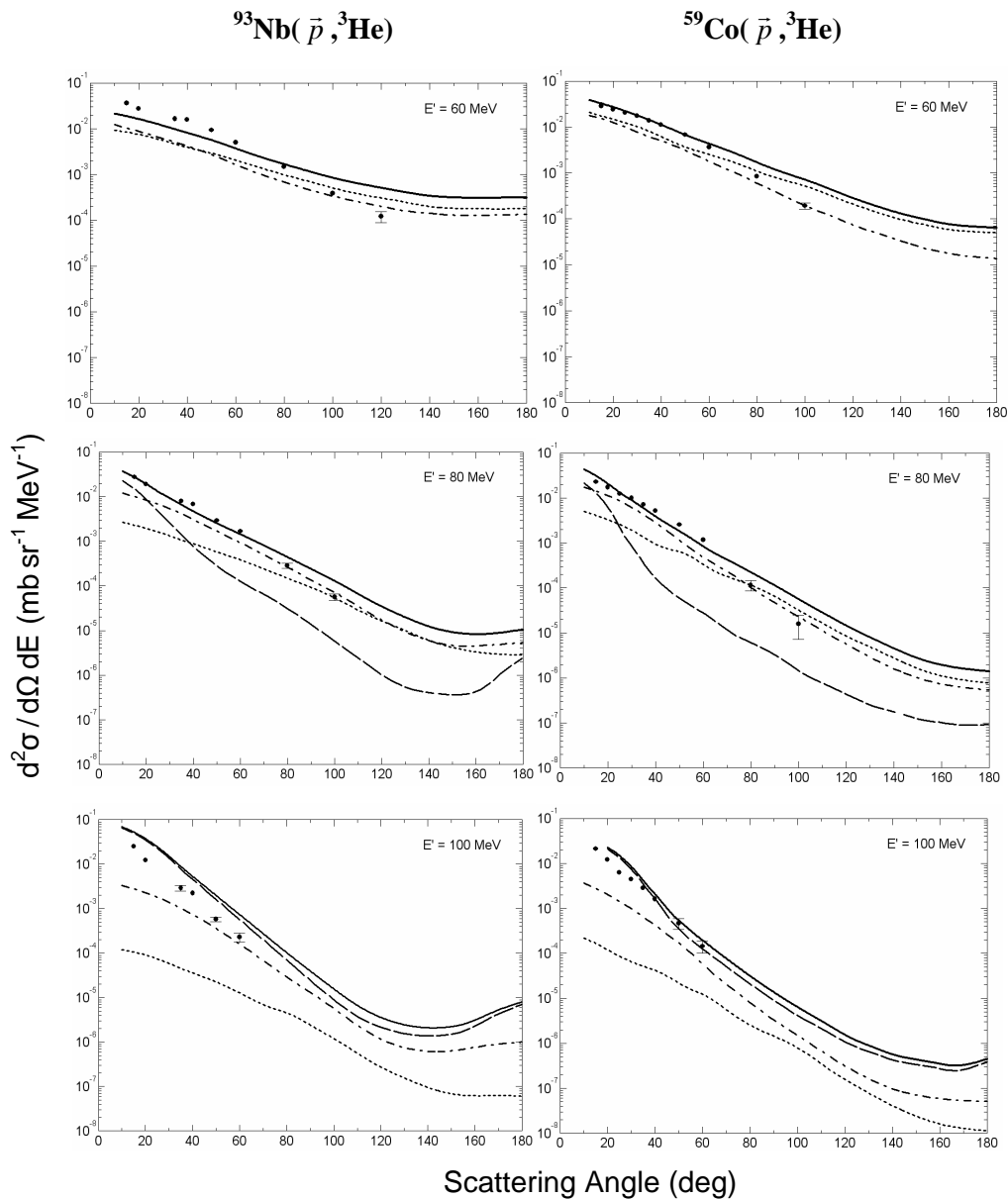


Figure 6.8: Cross section angular distributions for $^{93}\text{Nb}(\bar{p}, ^3\text{He})$ and $^{59}\text{Co}(\bar{p}, ^3\text{He})$ at 130 MeV incident energies and emission energies as indicated. The experimental data are compared with theoretical calculations for one step (— —), two step (- · - · -) and three step (····) contributions. The sum of the first three steps is indicated with a continuous curve.

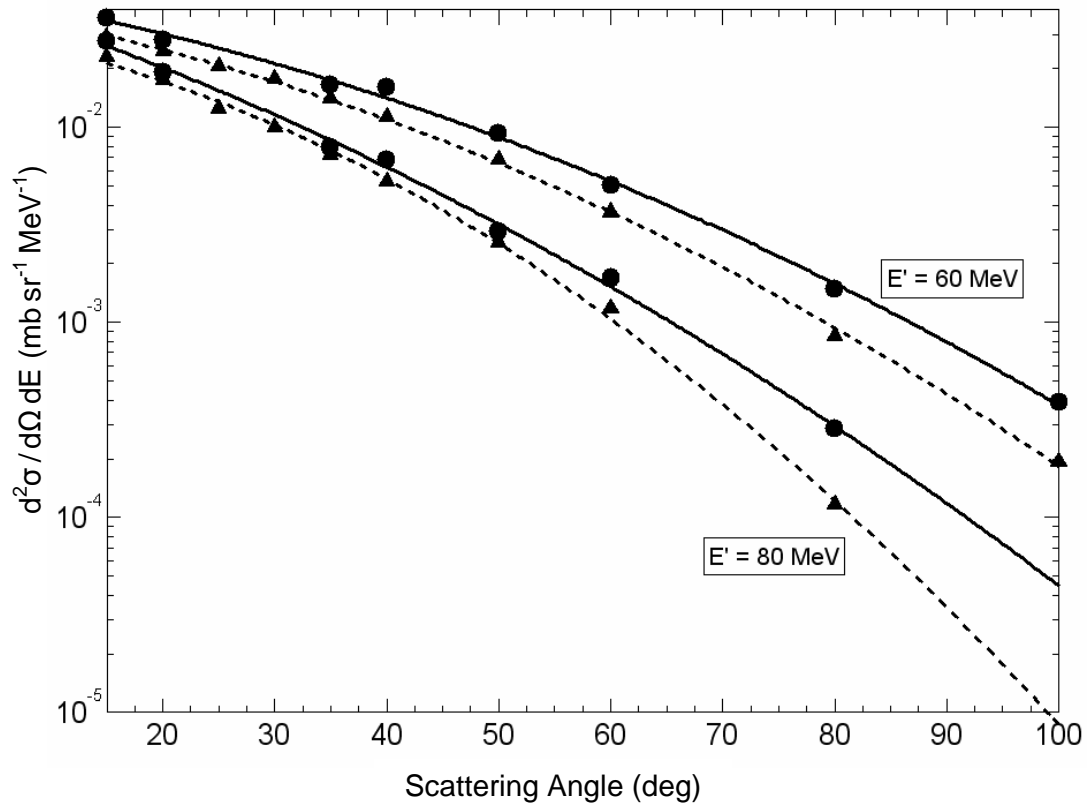


Figure 6.9: Cross section angular distributions for $^{93}\text{Nb}(\bar{p}, {}^3\text{He})$ and $^{59}\text{Co}(\bar{p}, {}^3\text{He})$ at 130 MeV incident energies and emission energies as indicated. The lines through the experimental cross section data of ^{93}Nb (\bullet) and ^{59}Co (\blacktriangle) serve to guide the eye.

6.4.2 Dependence of the double differential cross section on incident energy

Graphs of the double differential cross section for the reaction $^{59}\text{Co}(\bar{p}, ^3\text{He})$ at incident energies of 100 MeV, 130 MeV and 160 MeV are plotted in *figure 6.10* in order to illustrate the relationship between the features of the double differential cross section for different incident energies. The emission energies were chosen to be approximately 80% of the incident energies because according to Kalbach [Kal88] the reaction with the same ratio between incident and emission energy would result in similar slopes η for curves of double differential cross section as a function of scattering angle. The selection of incident and emission energy with a small difference also means that the first step dominates the reaction mechanism for the selected cases.

The set of graphs in *figure 6.10* shows that the magnitude of the double differential cross section at lower incident energies is higher than at higher incident energies. This is again to be expected due to the proton reaction cross section decreasing with incident energy in the range of 100 MeV to 160 MeV [Jac05]. The relative contribution of the second and third step reactions at larger scattering angles also increases with an increase in incident energy. This is most evident at an incident energy of 160 MeV where the first step reaction curve becomes distinguishable from the curve of the total differential cross section towards larger scattering angles. This is as a result of the one step reaction being more forward peaked at higher incident energies.

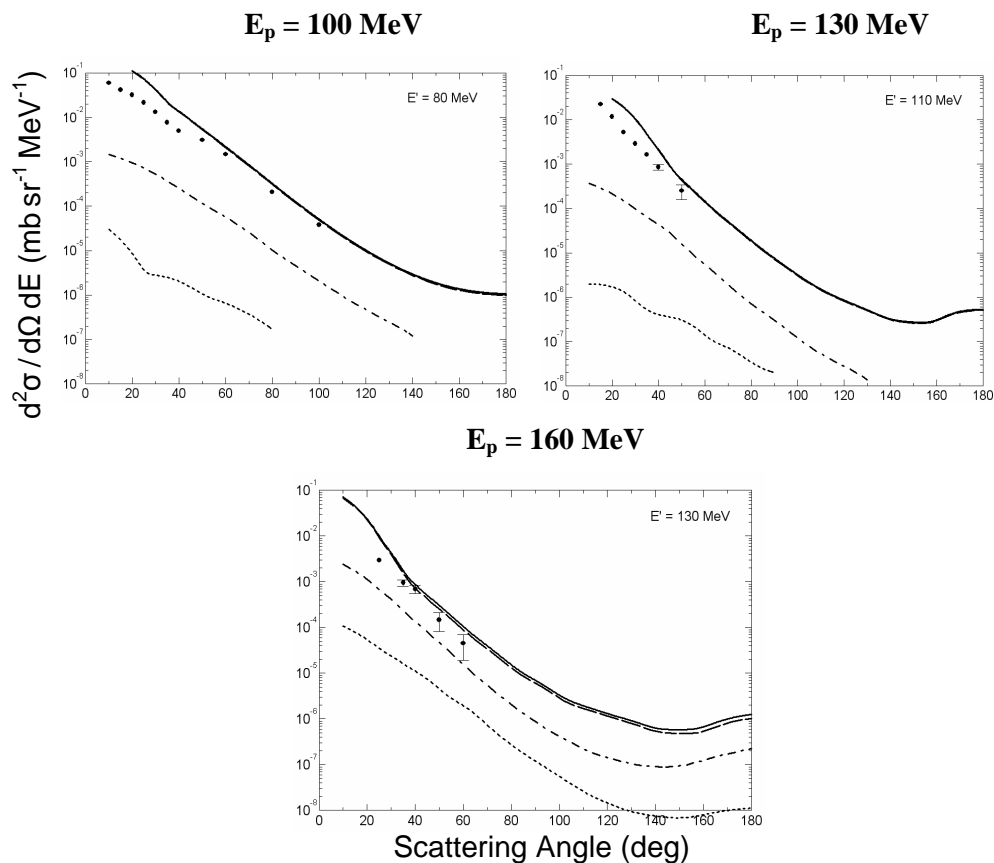


Figure 6.10: Cross section angular distributions for $^{59}\text{Co}(\bar{p}, {}^3\text{He})$ at incident energies 100 MeV, 130 MeV, 160 MeV and emission energies as indicated. The experimental data are compared with theoretical calculations for one step (— —), two step (- · - · -) and three step (····) contributions. The sum of the first three steps is indicated with a continuous curve. Emission energies were chosen to be approximately 80% of the incident energies

6.4.3 Variation of the double differential cross section with excitation energy

Graphs of the double differential cross section for the reaction $^{59}\text{Co}(\bar{p}, {}^3\text{He})$ at incident energies of 100 MeV, 130 MeV and 160 MeV are plotted in *figure 6.11* to investigate the relationship between double differential cross section and the energy transfer in the reactions (energy transfer is trivially linked to the excitation energy). The panels as arranged in three columns in *figure 6.11* represent graphs with the same energy differences of 50 MeV, 40

MeV and 30 MeV, respectively. This means that the excitation energy of the graphs in each column is equal, given by a value $E' = E_{diff} + Q$.

An increase in the slopes of angular distributions as function of emission energy is visible in the graphs in each row as the emission energy increases (*figure 6.11*). This is clearly seen to be as a result of the relative contributions of the first, second and third step towards the total double differential cross section, specifically with the first step being forward peaked. The first step contributes least to the total double differential cross section at an incident energy of 100 MeV and emission energy of 50 MeV. This phenomenon is evident in all the graphs with an energy difference 50 MeV (first column of graphs in *figure 6.11*). The contributions of the second and third step reactions are large at this energy differences, thus showing that the multistep reaction dominates the reaction mechanism at large energy differences.

The first-step reaction is the most prominent at small energy differences, as is seen in the graphs in the last column of *figure 6.11*. One-step reactions therefore increasingly dominate the mechanism at higher incident energies with high emission energies (small energy differences). Intuitively this is expected because of the correlation between energy loss and the number of steps in the reaction mechanism. All the double differential cross sections in the last column of *figure 6.11* are forward peaked, further illustrating the importance of a single step reaction mechanism.

The second-step reaction dominates between those extremes which were identified in the previous two paragraphs, and this is evident in the second column of *figure 6.11* where the energy difference between the incident and emission energies is 40 MeV (intermediate excitation energy). It is also obvious that the most variation in the contribution of the three different steps exists in this intermediate range of excitation energy. In each column the percentage of incident energy that is transferred in the reaction increases as the incident energy decreases.

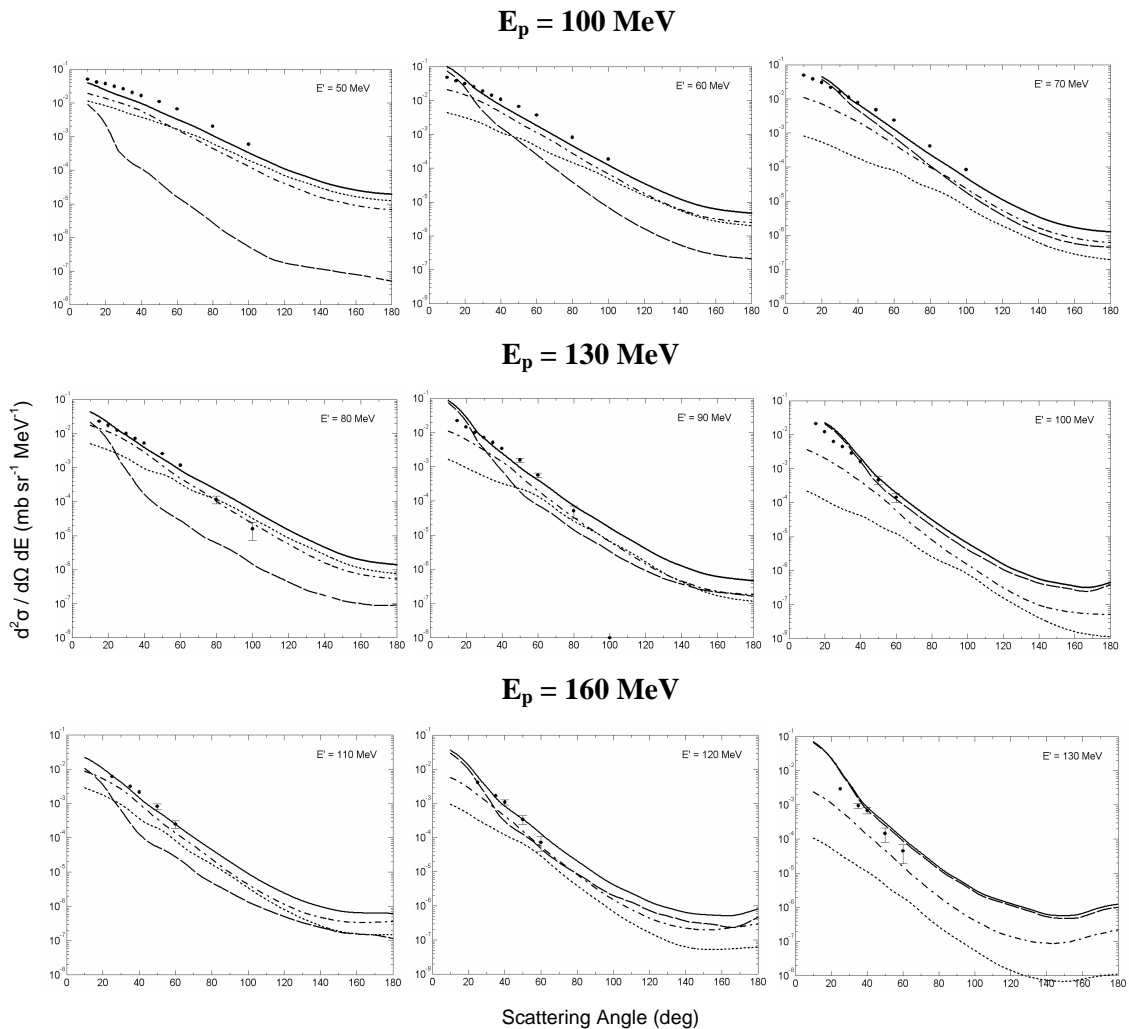


Figure 6.11: Cross section angular distributions for $^{59}\text{Co}(\bar{p}, {}^3\text{He})$ at incident energies 100 MeV, 130 MeV, 160 MeV and emission energies as indicated. The experimental data are compared with theoretical calculations for one step (— — —), two step (- · - · -) and three step (····) contributions. The sum of the first three steps is indicated with a continuous curve.

6.5 Characteristics of the Analysing Power Distributions

Because each successive collision of the multistep chain dilutes some of the spin characteristics of the reaction, the memory of the polarisation of the incident beam should fade away as the steps of the reaction increases. Analysing power is therefore more intrinsically sensitive to the details of the multistep reaction mechanism than the double differential cross section which relies on the gradual change in the shape of the contributions of each successive step. Hence the experimental double differential cross section gives the total double differential cross section values of all the steps but the experimental analysing power can be associated more closely with the number of steps in the reaction.

The theoretical curves for the one step reaction, a one step plus a two step reaction and a one step plus a two step plus a three step reactions are plotted on all the graphs. The relationships between the characteristics of the analysing power and a number of variables are discussed in the following subsections.

6.5.1 Comparison of analysing power distributions for different target nuclei

The analysing power distributions for the reactions $^{93}\text{Nb}(\vec{p}, ^3\text{He})$ and $^{59}\text{Co}(\vec{p}, ^3\text{He})$ at an incident energy of 130 MeV are plotted in *figure 6.12* to display the trend of the analysing power for different target nuclei. It is clear that the analysing power has some subtle dependence on the target nucleus, especially at high excitation energies. This is not unexpected as the number of nucleons in the nucleus will determine the rate at which higher-step processes become important.

At very low emission energies for both nuclei the analysing power tends towards smaller values as a result of the dominance of higher step reactions. The first step reactions with these target nuclei however show a slight difference in analysing power values which is probably only a manifestation of the structure differences of the two targets.

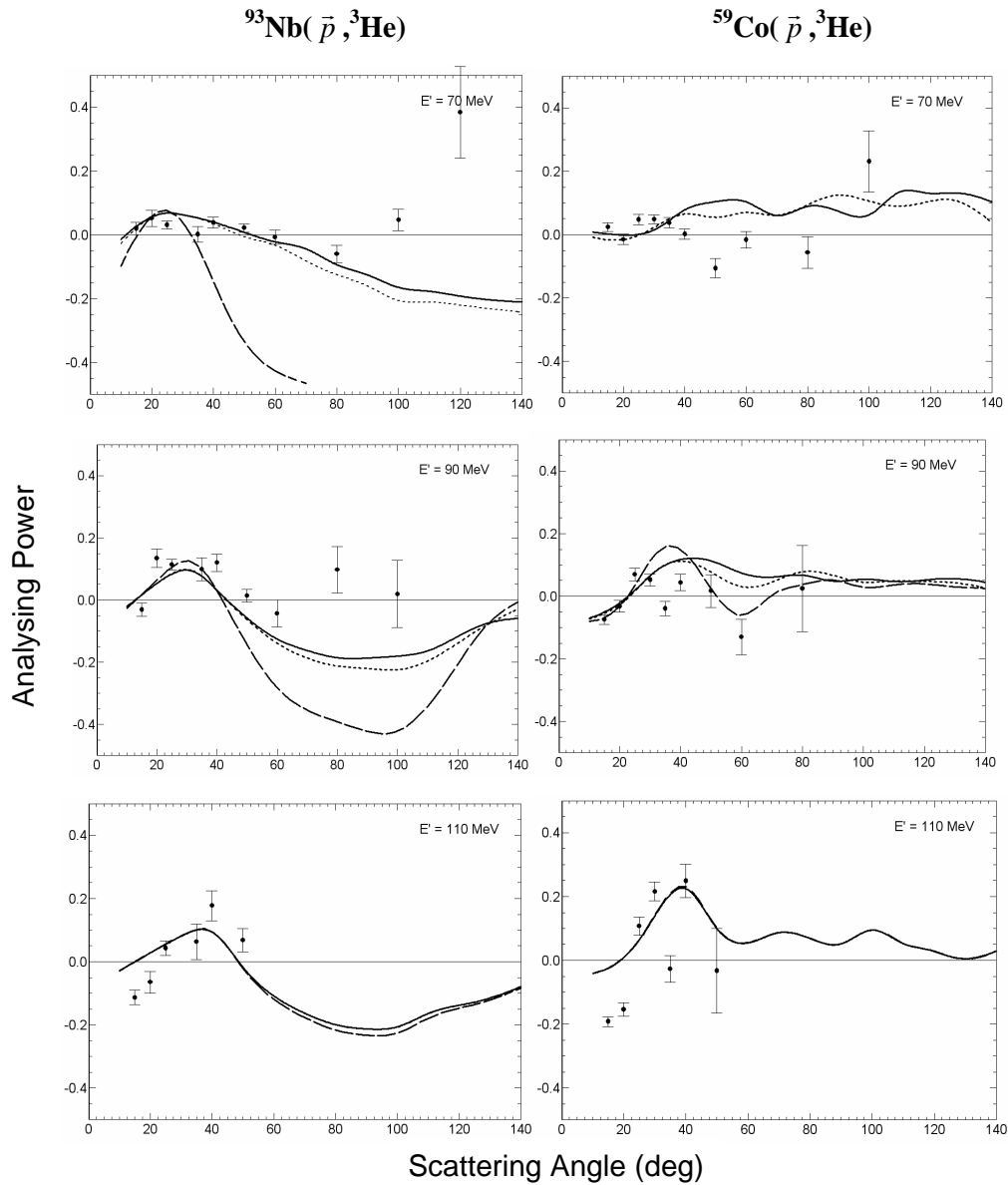


Figure 6.12: Analysing power as a function of scattering angle for $^{93}\text{Nb}(\bar{p}, ^3\text{He})$ and $^{59}\text{Co}(\bar{p}, ^3\text{He})$ at 130 MeV incident energies and emission energies as indicated. The experimental data are compared with theoretical calculations for a one step reaction (---), a one step plus a two step reaction (.....) and a one step plus a two step plus a three steps reaction (indicated with a continuous curve).

6.5.2 Analysing power as a function of incident energy

Analysing power distributions for the reaction $^{59}\text{Co}(\bar{p}, {}^3\text{He})$ at incident energies of 100 MeV, 130 MeV and 160 MeV and emission energies that are 80% of that of the incident energy are displayed in *figure 6.13*. The choice of emission energy is again motivated by the fact that Kalbach predicts similar shapes for the corresponding cross section distributions. The theoretical curves generally follow the experimental data.

We find slight evidence that the analysing power drops off towards zero as the incident energy increases, which is noticeable especially at the highest incident energy. This trend is consisted with zero analysing power values that were measured at an incident energy of 200 MeV [Ren91]. The shapes of the analysing power distributions at incident energies of 100 MeV and 130 MeV are in rough qualitative agreement, both with peaks at 40° and with most of the structure visible at low scattering angles. Of course, at the relatively high emission energy, the two and three step reaction contributions hardly influences the analysing power.

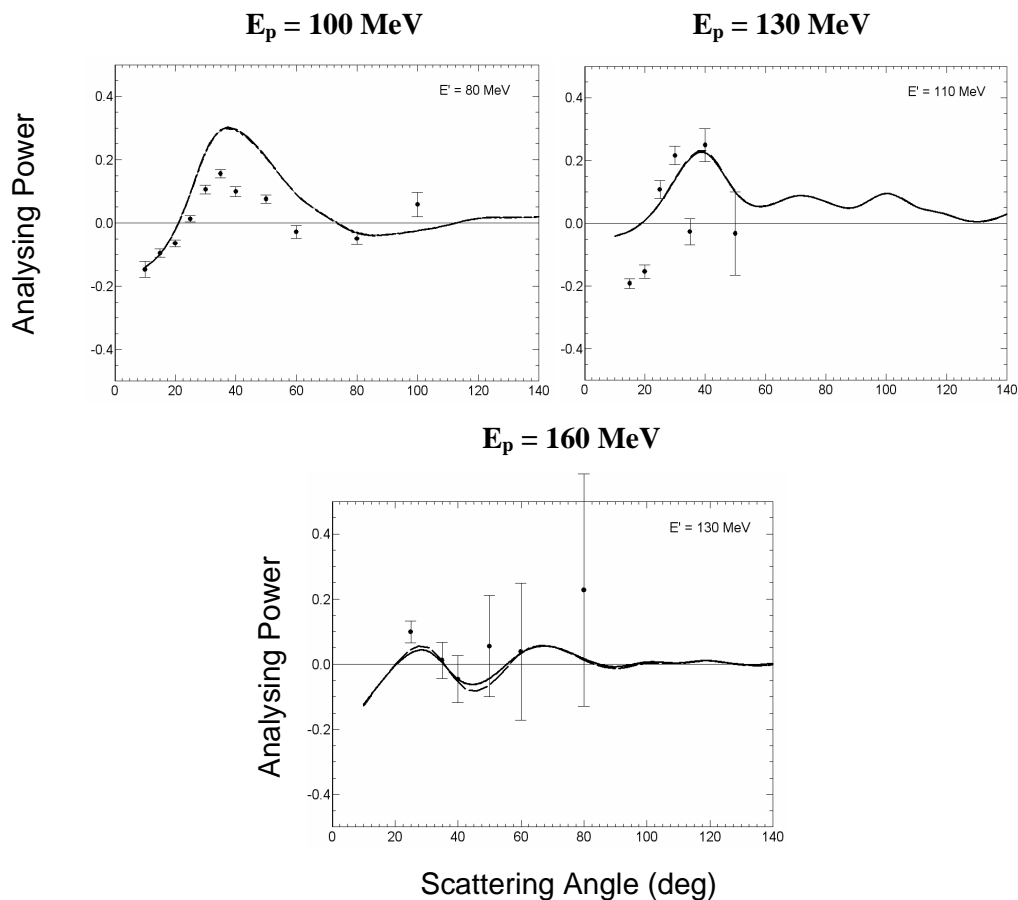


Figure 6.13: Analysing power as a function of scattering angle for $^{59}\text{Co}(\bar{p}, ^3\text{He})$ at 100 MeV, 130 MeV and 160 MeV incident energies and emission energies as indicated. The experimental data are compared with theoretical calculations for a one step reaction (— —) and a one step plus a two step plus a three steps reaction (indicated with a continuous curve). Emission energies were chosen to be approximately 80% of the incident energies

6.5.3 The dependence of the analysing power on excitation energy

The analysing power distributions of the reactions $^{59}\text{Co}(\bar{p}, ^3\text{He})$ and $^{93}\text{Nb}(\bar{p}, ^3\text{He})$ at incident energies of 100 MeV, 130 MeV and 160 MeV representing sets of graphs with energy differences of 20 MeV, 40 MeV and 60 MeV are plotted in *figure 6.14* to *figure 6.16* respectively. The theoretical predictions reproduce reasonably well the experimental data in all these figures.

The analysing power curves for the different nuclei at an energy difference of 20 MeV show similar features (see *figure 6.14*). The curves for both nuclei have positive peaks at $\sim 40^\circ$ and show a tendency to drop to zero as the scattering angle increases. In general, analysing power measurements at small scattering angle (forward peaked reactions) are associated with single step reactions. The positive peak in these analysing power curves can therefore be associated with single step direct reactions. As the excitation energy increases to 40 MeV (*figure 6.15*) the positive peak in the analysing power curves tends to shift to an angle of $\sim 30^\circ$. The height of the positive peaks also decreases with the increase in excitation energy. This is expected because reaction steps are directly linked to the excitation energy [Cow00] and the analysing power would drop with an increase in the steps of the reaction. At an excitation energy of 40 MeV (*figure 6.15*) the theoretical analysing power curves of the one step and sum of the first two steps become more distinguishable at larger scattering angles (larger than 20°). The experimental data support the one step reaction mechanism on ^{59}Co at scattering angles around $\sim 50^\circ$, especially at higher incident energies (130 MeV and 160 MeV). This emphasises the dominance of single step reactions at higher incident energies, even at larger scattering angles.

As was mentioned previously, measurements at large scattering angles are associated with multistep reactions. This explains the small analysing power values at large scattering angles in all the graphs. In *figure 6.16* (excitation energy of 60 MeV) the experimental data clearly support the dominance of multistep processes. At an incident energy of 100 MeV the theoretical curves for the higher step reactions (two and three step reactions) follow the experimental analysing power data particularly well. The analysing power of the different target nuclei (^{59}Co and ^{93}Nb) at similar incident energies and emission energies also

reproduces the experimental data reasonably well, suggesting that the reaction mechanisms in these target nuclei are quite similar.

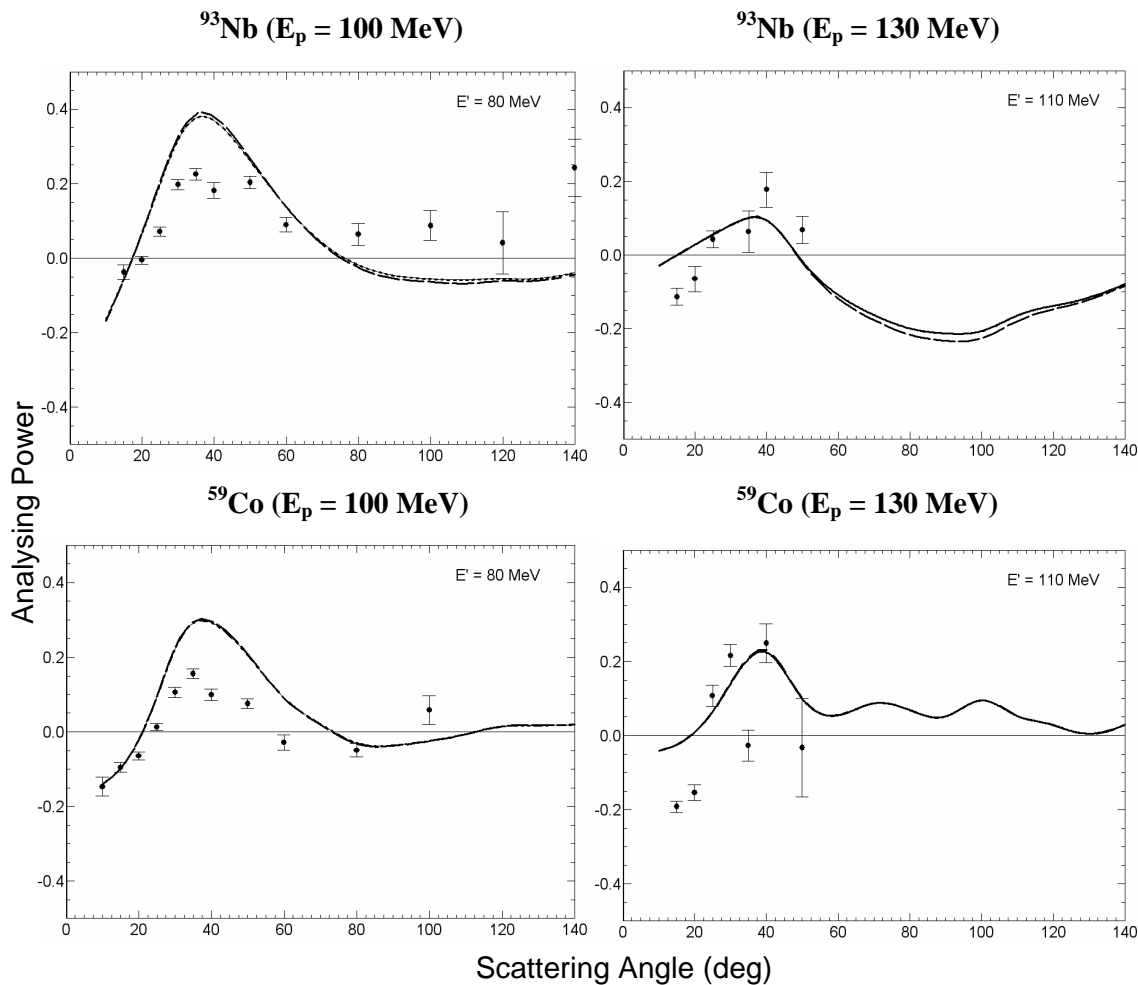


Figure 6.14: Analysing power as a function of scattering angle for $^{93}\text{Nb}(\bar{p}, {}^3\text{He})$ and $^{59}\text{Co}(\bar{p}, {}^3\text{He})$ with energy differences of 20 MeV. The experimental data are compared with theoretical calculations for a one step reaction (---), a one step plus a two step reaction (.....) and a one step plus a two step plus a three steps reaction (indicated with a continuous curve).

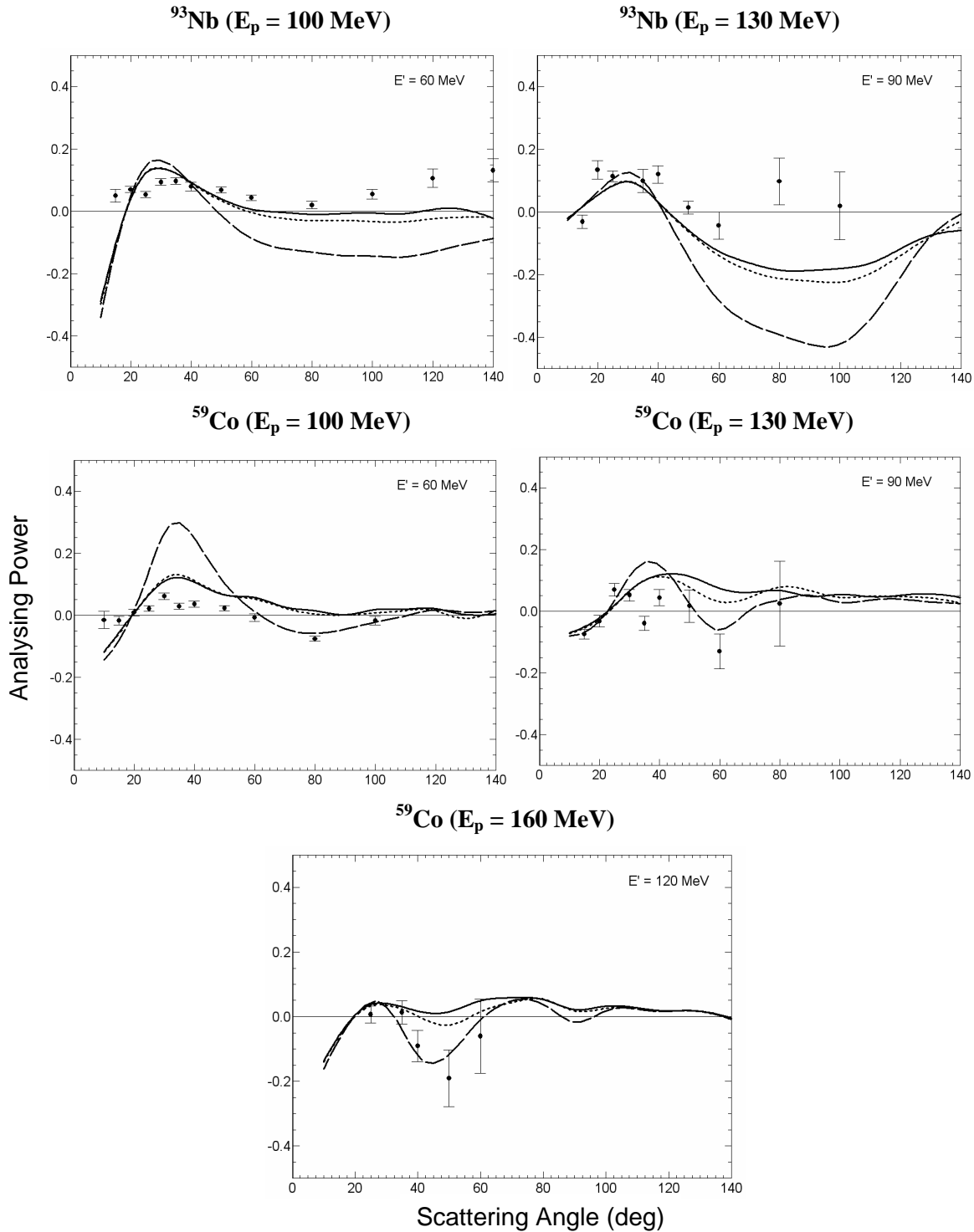


Figure 6.15: Analysing power as a function of scattering angle for $^{93}\text{Nb}(\bar{p}, ^3\text{He})$ and $^{59}\text{Co}(\bar{p}, ^3\text{He})$ with energy differences of 40 MeV. The experimental data are compared with theoretical calculations for a one step reaction (---), a one step plus a two step reaction (.....) and a one step plus a two step plus a three steps reaction (indicated with a continuous curve).

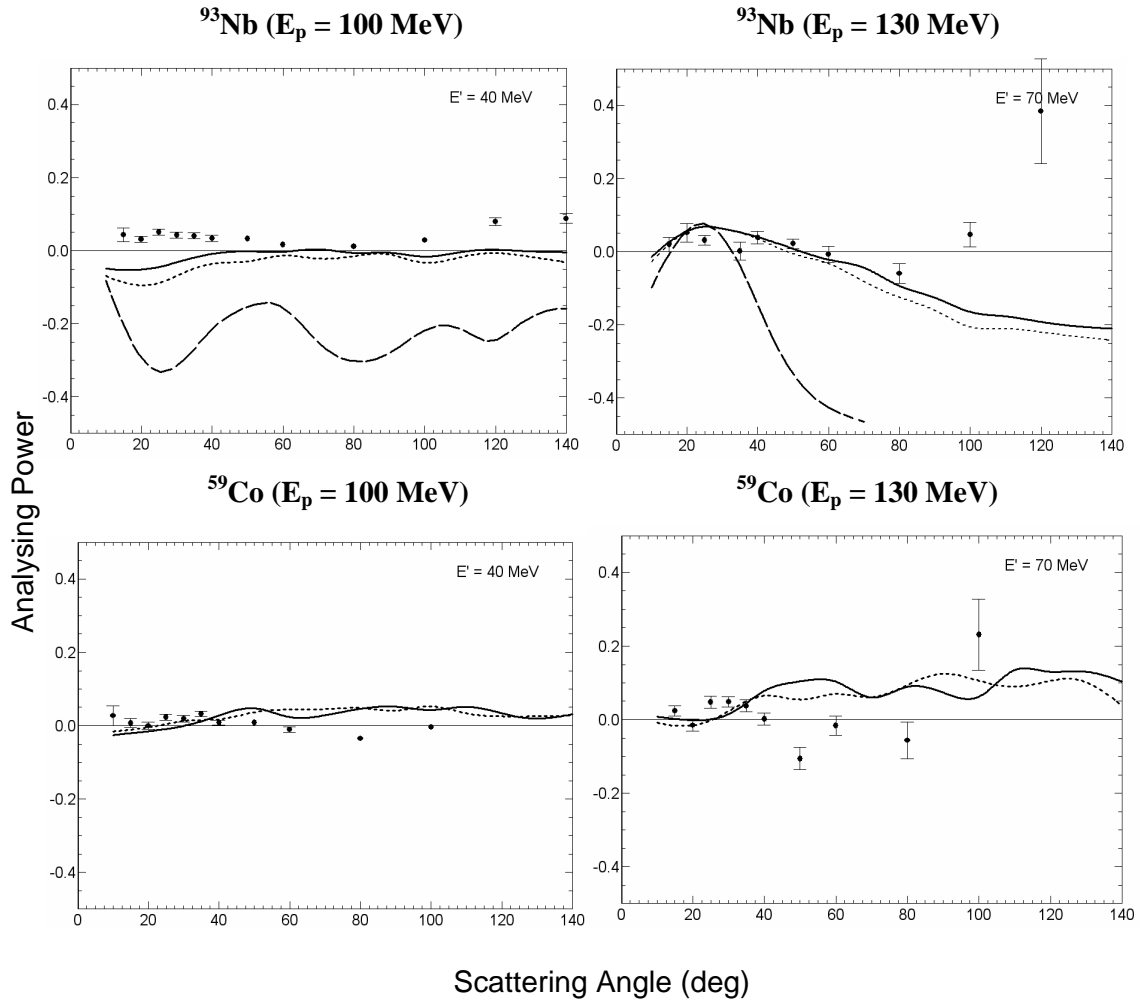


Figure 6.16: Analysing power as a function of scattering angle for $^{93}\text{Nb}(\bar{p}, ^3\text{He})$ and $^{59}\text{Co}(\bar{p}, ^3\text{He})$ with energy differences of 60 MeV. The experimental data are compared with theoretical calculations for a one step reaction (---), a one step plus a two step reaction (.....) and a one step plus a two step plus a three steps reaction (indicated with a continuous curve).

6.6 Summary of Results

The theory describes the experimental double differential cross section and analysing power data reasonably well over all incident and emission energies for both target nuclei. The double differential cross section distributions follow the systematic trend as predicted by the parameterisation of Kalbach, with an increase in yield with target mass as would be expected for an increase in reaction cross section.

The analysing power curves show similar trends at high emission energies for all incident energies but, as the emission energy decreases the values generally drop towards zero. The analysing power also becomes smaller as the incident energy increases with values fluctuating around zero at an incident energy of 160 MeV. Differences are observed for different target nuclei, but the analysing powers follow the general expected trend to drop to zero when excitation energies and scattering angles are increased.

The relative contributions of the first three steps vary systematically with incident and emission energy. The multistep mechanism (more than one step) dominates at low emission energies and large scattering angles. The one step reactions always display the forward peaking expected for a direct reaction. This characteristic feature of the one step reaction becomes more significant as the incident energy is increased, resulting in the second and third step reactions to become relatively more prominent by default at high incident energies and large scattering angles. The number of steps in the reaction mechanism increases as the excitation energy increases, with the multistep reactions being dominant at all excitation energies larger than ~ 30 MeV. The relative contributions of the different steps towards the total double differential cross section show no prominent dependence on the mass of the target nucleus.

For reference all sets of experimental double differential cross section and analysing power data are tabulated in *Appendix A*.

Chapter 7: SUMMARY AND CONCLUSIONS

In this study the energy dependence of the ($\bar{p}, ^3\text{He}$) reaction between 100 MeV and 160 MeV was explored by extracting the experimental double differential cross section and the analysing power distributions. The emphasis of the theoretical interpretation was put on a multistep reaction that precedes a pickup mechanism to finally form a composite emitted particle. Specifically, the $^{93}\text{Nb}(\bar{p}, ^3\text{He})$ and $^{59}\text{Co}(\bar{p}, ^3\text{He})$ reactions with incident energies of 100 MeV, 130 MeV and 160 MeV were investigated. Consequently this study expanded the work of Cowley *et al.* [Cow00] performed at an incident energy of 100 MeV to higher incident energies of 130 MeV and 160 MeV. Furthermore the data of Cowley *et al.* [Cow00] were re-analysed and included in this study for reasons of consistency of theoretical treatment over the complete range of incident energies.

Experimental double differential cross section and analysing power distributions were measured at angles ranging from 15° to 120° and at emission energies ranging from 30 MeV to the upper kinematic limit. These experimental data were compared with theoretical calculations. They were performed by employing the statistical multistep theory of Feshbach, Kerman and Koonin (FKK) [Fes88] which was extended to include a two nucleon (considered to be a deuteron) pickup at any stage of the multistep chain. A pickup mechanism was chosen as opposed to a knockout mechanism because it is speculated that there is a low probability of finding preformed helion clusters in the nucleus.

The new calculations at an incident energy of 100 MeV gave similar theoretical results as those of Cowley *et al.* indicating that the calculations are not very sensitive to exact details of the implementation of the implemented theory. As the incident energy is increased the characteristics of the reaction mechanism also remained consistent. Most insight on the reaction mechanism in this study came from examining the double differential cross section distributions in conjunction with the analysing power values. The theory predicted the experimental double differential cross section and analysing power data reasonably well over all incident and emission energies for both target nuclei. In general the two target nuclei demonstrated similar responses, suggesting that both of them shared the same reaction mechanism. An increase in the magnitude of the experimental double differential cross

section of this reaction was observed as the number of nucleons in the nucleus increased. This increase is roughly as would be expected because of the relation between the target mass and the reaction cross section.

The contributions of the first three steps of the multistep reaction to the double differential cross section and analysing power were also investigated. The multistep mechanism (more than one step) dominated at low emission energies and large scattering angles. The single step contributions were typically forward peaked as determined by the direct reaction process. This characteristic of the single step reaction became more prominent as the incident energy increases, therefore at these higher incident energies the relative contribution of the second and third steps became more noticeable at large scattering angles. At excitation energies larger than ~30 MeV the higher step reactions played an increasingly important role over the whole range of scattering angles. Conversely, the single step reactions dominated at high emission energies and small scattering angles (forward peaked reactions) for all incident energies. The relative contributions of the different steps towards the total double differential cross section showed no clear dependence on the mass of the target nucleus.

The reasonable agreement between the theoretical predictions and the experimental data, serves as an indication that the assumed multistep pickup mechanism is probably correct. Nevertheless, one would have hoped for even better agreement between the theory and the experimental data, and there are certainly areas for refinement to the theoretical calculations. For example, the sensitivity of the ^3He potential is a main point of concern and guidance on this would be useful. Although the pickup reaction mechanism does reasonably well a knockout reaction mechanism should also be investigated, but this was beyond the scope of this study.

Clearly, as was pointed out, further improvements to the present theoretical formulation, as well as studies of alternative reaction mechanisms are desirable.

APPENDIX A

A.1 Experimental data for $^{59}\text{Co}(\bar{p}, ^3\text{He})$ at an incident energy of 100 MeV

Angle [Deg]	Energy [MeV]	Cross section (σ) [mb sr ⁻¹ MeV ⁻¹]	Statistical error on σ	Analysing power (A_y)	Statistical error on A_y
10	34	5.55E+01	1.05E+00	-3.21E-02	2.63E-02
	38	5.33E+01	1.02E+00	2.75E-02	2.69E-02
	42	5.21E+01	1.01E+00	-3.24E-02	2.72E-02
	46	5.11E+01	1.00E+00	-1.75E-02	2.75E-02
	50	5.06E+01	9.99E-01	-1.32E-02	2.76E-02
	54	5.01E+01	9.94E-01	-1.63E-02	2.77E-02
	58	4.83E+01	9.76E-01	-1.50E-02	2.82E-02
	62	4.83E+01	9.75E-01	-1.89E-02	2.82E-02
	66	4.84E+01	9.77E-01	-1.26E-02	2.82E-02
	70	4.93E+01	9.85E-01	-6.13E-02	2.79E-02
	74	5.68E+01	1.06E+00	-1.36E-01	2.59E-02
	78	5.97E+01	1.08E+00	-1.47E-01	2.52E-02
	82	6.91E+01	1.17E+00	-1.73E-01	2.34E-02
	86	7.25E+01	1.20E+00	-1.94E-01	2.28E-02
	90	5.36E+01	1.03E+00	-1.74E-01	2.66E-02
15	34	4.78E+01	3.78E-01	-5.62E-04	1.20E-02
	38	4.55E+01	3.68E-01	6.87E-03	1.23E-02
	42	4.45E+01	3.64E-01	9.05E-03	1.24E-02
	46	4.31E+01	3.58E-01	-2.13E-03	1.26E-02
	50	4.17E+01	3.53E-01	3.18E-03	1.28E-02
	54	4.09E+01	3.49E-01	-3.57E-02	1.29E-02
	58	3.94E+01	3.43E-01	-1.71E-02	1.32E-02
	62	3.78E+01	3.36E-01	-8.68E-03	1.34E-02
	66	3.75E+01	3.35E-01	-2.38E-02	1.35E-02
	70	3.84E+01	3.38E-01	-6.02E-02	1.34E-02
	74	4.25E+01	3.56E-01	-1.16E-01	1.27E-02
	78	4.18E+01	3.53E-01	-9.53E-02	1.28E-02
	82	4.70E+01	3.74E-01	-1.36E-01	1.20E-02
	86	4.80E+01	3.78E-01	-1.22E-01	1.20E-02
	90	3.49E+01	3.23E-01	-2.06E-01	1.39E-02
20	34	4.43E+01	2.55E-01	1.16E-02	9.73E-03
	38	4.22E+01	2.49E-01	-6.31E-04	9.96E-03
	42	4.10E+01	2.45E-01	1.71E-03	1.01E-02
	46	3.94E+01	2.40E-01	1.27E-02	1.03E-02
	50	3.73E+01	2.34E-01	2.89E-02	1.06E-02
	54	3.53E+01	2.28E-01	1.70E-02	1.09E-02
	58	3.40E+01	2.23E-01	9.34E-03	1.11E-02
	62	3.18E+01	2.16E-01	-8.67E-03	1.15E-02

	66	3.11E+01	2.13E-01	3.26E-02	1.16E-02
	70	3.03E+01	2.11E-01	-3.25E-02	1.18E-02
	74	3.21E+01	2.17E-01	-5.37E-02	1.15E-02
	78	3.19E+01	2.16E-01	-6.46E-02	1.15E-02
	82	3.07E+01	2.12E-01	-7.73E-02	1.17E-02
	86	3.24E+01	2.18E-01	-1.07E-01	1.14E-02
	90	2.29E+01	1.83E-01	-1.98E-01	1.35E-02
25	34	3.99E+01	1.95E-01	2.64E-02	7.57E-03
	38	3.71E+01	1.88E-01	2.33E-02	7.84E-03
	42	3.55E+01	1.84E-01	2.20E-02	8.03E-03
	46	3.33E+01	1.78E-01	1.71E-02	8.28E-03
	50	3.11E+01	1.72E-01	3.25E-02	8.57E-03
	54	2.92E+01	1.67E-01	2.16E-02	8.85E-03
	58	2.70E+01	1.61E-01	2.17E-02	9.19E-03
	62	2.56E+01	1.56E-01	1.54E-02	9.44E-03
	66	2.38E+01	1.51E-01	4.33E-02	9.79E-03
	70	2.17E+01	1.44E-01	7.73E-03	1.03E-02
	74	2.13E+01	1.42E-01	-1.25E-03	1.04E-02
	78	2.16E+01	1.44E-01	1.30E-02	1.03E-02
	82	1.83E+01	1.32E-01	-2.08E-02	1.12E-02
	86	1.97E+01	1.37E-01	-8.41E-02	1.07E-02
	90	1.42E+01	1.16E-01	-1.23E-01	1.27E-02
30	34	3.57E+01	1.78E-01	5.05E-03	8.49E-03
	38	3.30E+01	1.71E-01	1.93E-02	8.83E-03
	42	3.06E+01	1.65E-01	2.55E-02	9.18E-03
	46	2.84E+01	1.59E-01	2.32E-02	9.50E-03
	50	2.60E+01	1.52E-01	2.12E-02	9.94E-03
	54	2.41E+01	1.46E-01	3.48E-02	1.03E-02
	58	2.14E+01	1.38E-01	6.15E-02	1.10E-02
	62	1.93E+01	1.31E-01	4.55E-02	1.15E-02
	66	1.78E+01	1.26E-01	6.50E-02	1.20E-02
	70	1.61E+01	1.20E-01	9.17E-02	1.27E-02
	74	1.43E+01	1.13E-01	8.92E-02	1.34E-02
	78	1.32E+01	1.08E-01	1.06E-01	1.40E-02
	82	1.09E+01	9.84E-02	1.17E-01	1.54E-02
	86	1.14E+01	1.01E-01	1.02E-02	1.50E-02
	90	6.87E+00	7.82E-02	6.98E-02	1.93E-02
35	34	3.04E+01	1.44E-01	1.48E-02	7.00E-03
	38	2.77E+01	1.37E-01	3.19E-02	7.32E-03
	42	2.50E+01	1.31E-01	2.78E-02	7.70E-03
	46	2.28E+01	1.24E-01	3.07E-02	8.09E-03
	50	2.06E+01	1.18E-01	1.96E-02	8.51E-03
	54	1.82E+01	1.11E-01	2.86E-02	9.05E-03
	58	1.63E+01	1.05E-01	2.94E-02	9.54E-03
	62	1.44E+01	9.90E-02	5.44E-02	1.02E-02
	66	1.26E+01	9.26E-02	8.52E-02	1.08E-02

	70	1.12E+01	8.74E-02	9.35E-02	1.15E-02
	74	9.40E+00	8.00E-02	1.07E-01	1.25E-02
	78	7.72E+00	7.25E-02	1.56E-01	1.38E-02
	82	6.60E+00	6.70E-02	2.02E-01	1.49E-02
	86	6.21E+00	6.50E-02	1.87E-01	1.54E-02
	90	3.16E+00	4.63E-02	1.81E-01	2.17E-02
40	34	2.66E+01	1.22E-01	1.96E-02	6.80E-03
	38	2.41E+01	1.16E-01	8.17E-03	7.15E-03
	42	2.11E+01	1.09E-01	1.81E-02	7.63E-03
	46	1.87E+01	1.03E-01	3.25E-02	8.10E-03
	50	1.65E+01	9.64E-02	2.94E-02	8.63E-03
	54	1.44E+01	8.99E-02	3.36E-02	9.27E-03
	58	1.26E+01	8.43E-02	3.60E-02	9.87E-03
	62	1.09E+01	7.82E-02	4.92E-02	1.06E-02
	66	9.35E+00	7.25E-02	3.61E-02	1.15E-02
	70	7.78E+00	6.62E-02	5.82E-02	1.26E-02
	74	6.56E+00	6.07E-02	3.75E-02	1.37E-02
	78	4.99E+00	5.30E-02	9.96E-02	1.57E-02
	82	4.18E+00	4.85E-02	1.57E-01	1.71E-02
	86	3.47E+00	4.42E-02	1.71E-01	1.88E-02
	90	1.52E+00	2.92E-02	2.20E-01	2.83E-02
50	34	1.95E+01	5.91E-02	3.17E-03	5.09E-03
	38	1.69E+01	5.49E-02	8.41E-03	5.48E-03
	42	1.48E+01	5.14E-02	4.05E-03	5.85E-03
	46	1.27E+01	4.76E-02	1.60E-02	6.32E-03
	50	1.10E+01	4.43E-02	1.09E-02	6.79E-03
	54	9.34E+00	4.09E-02	1.33E-02	7.36E-03
	58	8.03E+00	3.79E-02	2.33E-02	7.94E-03
	62	6.69E+00	3.46E-02	1.98E-02	8.70E-03
	66	5.70E+00	3.19E-02	2.85E-02	9.43E-03
	70	4.77E+00	2.92E-02	3.84E-02	1.03E-02
	74	3.81E+00	2.61E-02	5.72E-02	1.15E-02
	78	3.13E+00	2.37E-02	7.52E-02	1.27E-02
	82	2.62E+00	2.16E-02	8.50E-02	1.39E-02
	86	2.05E+00	1.91E-02	9.91E-02	1.57E-02
	90	1.21E+00	1.47E-02	7.51E-02	2.04E-02
60	34	1.37E+01	5.86E-02	-2.01E-02	7.02E-03
	38	1.15E+01	5.36E-02	-1.07E-02	7.67E-03
	42	9.72E+00	4.94E-02	-2.30E-02	8.34E-03
	46	8.04E+00	4.49E-02	-2.01E-02	9.18E-03
	50	6.65E+00	4.08E-02	-2.06E-02	1.01E-02
	54	5.55E+00	3.73E-02	-1.82E-02	1.10E-02
	58	4.52E+00	3.37E-02	-6.92E-03	1.22E-02
	62	3.72E+00	3.06E-02	-9.61E-03	1.34E-02
	66	3.04E+00	2.76E-02	-3.47E-02	1.48E-02
	70	2.36E+00	2.43E-02	-3.35E-02	1.67E-02

	74	1.89E+00	2.18E-02	-4.40E-03	1.87E-02
	78	1.49E+00	1.93E-02	-2.89E-02	2.10E-02
	82	1.19E+00	1.72E-02	6.39E-03	2.33E-02
	86	8.80E-01	1.48E-02	-5.42E-03	2.69E-02
	90	5.19E-01	1.14E-02	-3.80E-02	3.43E-02
80	34	6.11E+00	1.53E-02	-3.07E-02	3.36E-03
	38	4.68E+00	1.34E-02	-3.45E-02	3.84E-03
	42	3.55E+00	1.17E-02	-4.85E-02	4.41E-03
	46	2.71E+00	1.02E-02	-4.60E-02	5.06E-03
	50	2.03E+00	8.82E-03	-4.31E-02	5.83E-03
	54	1.53E+00	7.64E-03	-6.19E-02	6.73E-03
	58	1.14E+00	6.60E-03	-7.55E-02	7.79E-03
	62	8.16E-01	5.59E-03	-6.67E-02	9.21E-03
	66	5.96E-01	4.78E-03	-5.90E-02	1.08E-02
	70	4.17E-01	3.99E-03	-8.73E-02	1.29E-02
	74	2.98E-01	3.38E-03	-6.48E-02	1.53E-02
	78	2.11E-01	2.84E-03	-4.95E-02	1.82E-02
	82	1.47E-01	2.37E-03	-6.19E-02	2.18E-02
	86	8.78E-02	1.83E-03	6.59E-03	2.83E-02
	90	5.66E-02	1.47E-03	-4.33E-02	3.49E-02
100	34	2.61E+00	8.89E-03	-5.59E-03	4.64E-03
	38	1.81E+00	7.39E-03	-3.93E-03	5.57E-03
	42	1.25E+00	6.16E-03	-8.33E-03	6.70E-03
	46	8.64E-01	5.11E-03	1.54E-03	8.07E-03
	50	5.98E-01	4.25E-03	-2.00E-02	9.71E-03
	54	4.06E-01	3.50E-03	-6.16E-03	1.18E-02
	58	2.77E-01	2.89E-03	-1.71E-02	1.43E-02
	62	1.85E-01	2.37E-03	-8.99E-03	1.75E-02
	66	1.24E-01	1.93E-03	3.25E-02	2.15E-02
	70	8.45E-02	1.60E-03	-4.10E-02	2.59E-02
	74	5.74E-02	1.32E-03	4.15E-02	3.17E-02
	78	3.80E-02	1.07E-03	5.80E-02	3.84E-02
	82	2.62E-02	8.90E-04	3.16E-02	4.70E-02
	86	1.68E-02	7.12E-04	4.10E-03	5.78E-02
	90	1.22E-02	6.08E-04	2.65E-01	6.66E-02

A.2 Experimental data for $^{59}\text{Co}(\bar{p}, ^3\text{He})$ at an incident energy of 130 MeV

Angle [Deg]	Energy [MeV]	Cross section (σ) [mb sr ⁻¹ MeV ⁻¹]	Statistical error on σ	Analysing power (A_y)	Statistical error on A_y
15	30	4.61E-02	1.42E-03	1.34E-02	1.10E-02
	34	4.22E-02	1.36E-03	2.48E-02	1.14E-02
	38	3.97E-02	1.32E-03	-9.79E-03	1.17E-02
	42	3.69E-02	1.27E-03	-1.57E-02	1.22E-02
	46	3.52E-02	1.24E-03	-8.49E+00	5.00E+01
	50	3.35E-02	1.21E-03	1.29E-02	1.28E-02
	54	3.21E-02	1.18E-03	6.93E-03	1.30E-02
	58	3.10E-02	1.16E-03	-2.02E-02	1.33E-02
	62	2.88E-02	1.12E-03	1.64E-02	1.38E-02
	66	2.80E-02	1.10E-03	-3.30E-02	1.40E-02
	70	2.70E-02	1.08E-03	2.36E-02	1.42E-02
	74	2.51E-02	1.05E-03	6.08E-03	1.47E-02
	78	2.45E-02	1.03E-03	5.14E-03	1.49E-02
	82	2.29E-02	9.99E-04	-3.77E-02	1.54E-02
	86	2.32E-02	1.01E-03	-8.50E-02	1.53E-02
	90	2.25E-02	9.90E-04	-7.40E-02	1.55E-02
	94	2.22E-02	9.85E-04	-1.06E-01	1.56E-02
	98	2.12E-02	9.61E-04	-1.50E-01	1.59E-02
	102	2.14E-02	9.66E-04	-1.86E-01	1.58E-02
	106	2.11E-02	9.60E-04	-2.17E-01	1.58E-02
	110	2.24E-02	9.88E-04	-1.92E-01	1.54E-02
	114	1.75E-02	8.61E-04	-3.12E-01	1.82E-02
	118	6.06E-03	4.76E-04	-3.83E-02	4.25E-02
	122	7.09E-04	1.72E-04	1.30E-01	9.63E-02
20	30	4.23E-02	1.34E-03	-1.92E-03	1.13E-02
	34	3.76E-02	1.26E-03	9.92E-03	1.19E-02
	38	3.47E-02	1.21E-03	-3.13E-02	1.24E-02
	42	3.38E-02	1.20E-03	4.26E-02	1.25E-02
	46	3.12E-02	1.15E-03	1.36E-02	1.31E-02
	50	2.97E-02	1.12E-03	3.31E-03	1.34E-02
	54	2.72E-02	1.07E-03	2.73E-02	1.39E-02
	58	2.61E-02	1.05E-03	1.99E-02	1.42E-02
	62	2.44E-02	1.02E-03	-1.22E-02	1.47E-02
	66	2.25E-02	9.77E-04	4.50E-02	1.53E-02
	70	2.13E-02	9.50E-04	-1.49E-02	1.57E-02
	74	2.01E-02	9.24E-04	1.04E-02	1.62E-02
	78	1.85E-02	8.86E-04	3.47E-02	1.69E-02
	82	1.75E-02	8.60E-04	7.44E-03	1.74E-02
	86	1.68E-02	8.43E-04	2.27E-02	1.78E-02
	90	1.46E-02	7.87E-04	-3.24E-02	1.90E-02
	94	1.39E-02	7.67E-04	-1.99E-02	1.95E-02
	98	1.30E-02	7.41E-04	-9.23E-02	2.02E-02

	102	1.23E-02	7.22E-04	-4.71E-02	2.07E-02
	106	1.14E-02	6.95E-04	-7.33E-02	2.15E-02
	110	1.17E-02	7.04E-04	-1.54E-01	2.12E-02
	114	9.02E-03	6.12E-04	-1.92E-01	2.49E-02
25	30	3.98E-02	1.17E-03	7.18E-04	1.05E-02
	34	3.60E-02	1.11E-03	1.21E-02	1.10E-02
	38	3.26E-02	1.06E-03	-1.67E-02	1.15E-02
	42	3.02E-02	1.02E-03	1.51E-02	1.20E-02
	46	2.84E-02	9.93E-04	2.09E-02	1.24E-02
	50	2.59E-02	9.46E-04	1.69E-02	1.30E-02
	54	2.42E-02	9.16E-04	2.24E-02	1.34E-02
	58	2.20E-02	8.73E-04	1.56E-02	1.41E-02
	62	2.06E-02	8.45E-04	1.25E-02	1.45E-02
	66	1.90E-02	8.12E-04	1.86E-02	1.51E-02
	70	1.69E-02	7.65E-04	4.76E-02	1.60E-02
	74	1.60E-02	7.45E-04	1.09E-02	1.65E-02
	78	1.43E-02	7.03E-04	6.82E-02	1.74E-02
	82	1.25E-02	6.58E-04	6.45E-03	1.86E-02
	86	1.14E-02	6.30E-04	6.67E-02	1.95E-02
	90	1.02E-02	5.93E-04	7.02E-02	2.06E-02
	94	8.61E-03	5.46E-04	7.43E-02	2.25E-02
	98	7.94E-03	5.25E-04	1.21E-01	2.34E-02
	102	6.36E-03	4.70E-04	1.75E-01	2.59E-02
	106	5.72E-03	4.45E-04	1.63E-01	2.74E-02
	110	5.24E-03	4.26E-04	1.07E-01	2.87E-02
	114	3.16E-03	3.28E-04	8.50E-02	3.84E-02
	118	9.70E-04	1.76E-04	1.70E-01	8.03E-02
	122	1.56E-04	7.16E-05	-5.17E-02	1.86E-01
30	30	3.69E-02	8.74E-04	-1.38E-02	8.47E-03
	34	3.26E-02	8.22E-04	-1.39E-02	8.96E-03
	38	2.98E-02	7.86E-04	1.44E-02	9.36E-03
	42	2.72E-02	7.51E-04	-9.61E-03	9.78E-03
	46	2.51E-02	7.22E-04	1.78E-02	1.02E-02
	50	2.32E-02	6.93E-04	1.87E-02	1.06E-02
	54	2.09E-02	6.59E-04	3.62E-02	1.11E-02
	58	1.89E-02	6.26E-04	2.18E-02	1.17E-02
	62	1.77E-02	6.07E-04	-6.87E-03	1.21E-02
	66	1.55E-02	5.68E-04	1.47E-02	1.29E-02
	70	1.40E-02	5.39E-04	4.80E-02	1.36E-02
	74	1.27E-02	5.13E-04	-1.56E-03	1.43E-02
	78	1.11E-02	4.81E-04	4.09E-02	1.53E-02
	82	9.99E-03	4.56E-04	5.94E-02	1.61E-02
	86	8.54E-03	4.21E-04	5.54E-02	1.74E-02
	90	7.24E-03	3.88E-04	5.24E-02	1.89E-02
	94	6.10E-03	3.56E-04	6.39E-02	2.06E-02
	98	5.28E-03	3.31E-04	7.00E-02	2.22E-02
	102	4.45E-03	3.04E-04	1.34E-01	2.41E-02

	106	3.63E-03	2.75E-04	1.65E-01	2.66E-02
	110	2.89E-03	2.45E-04	2.16E-01	2.96E-02
	114	1.78E-03	1.91E-04	1.92E-01	3.92E-02
	118	5.24E-04	9.97E-05	2.62E-01	8.71E-02
	122	1.51E-04	5.59E-05	4.48E-01	1.25E-01
35	30	3.38E-02	8.83E-04	-2.69E-02	9.33E-03
	34	3.02E-02	8.35E-04	-1.90E-02	9.85E-03
	38	2.69E-02	7.90E-04	-5.67E-03	1.04E-02
	42	2.41E-02	7.47E-04	-1.21E-02	1.10E-02
	46	2.19E-02	7.13E-04	1.44E-03	1.15E-02
	50	1.99E-02	6.79E-04	5.78E-03	1.21E-02
	54	1.75E-02	6.37E-04	1.01E-02	1.29E-02
	58	1.60E-02	6.09E-04	9.35E-03	1.34E-02
	62	1.40E-02	5.70E-04	5.78E-03	1.44E-02
	66	1.30E-02	5.49E-04	4.47E-02	1.49E-02
	70	1.15E-02	5.17E-04	3.74E-02	1.59E-02
	74	9.79E-03	4.76E-04	4.33E-03	1.72E-02
	78	8.49E-03	4.44E-04	2.13E-02	1.85E-02
	82	7.24E-03	4.10E-04	5.89E-03	2.00E-02
	86	5.97E-03	3.72E-04	1.80E-02	2.21E-02
	90	5.17E-03	3.46E-04	-3.92E-02	2.37E-02
	94	3.89E-03	3.00E-04	-1.22E-03	2.74E-02
	98	3.50E-03	2.85E-04	8.19E-02	2.88E-02
	102	2.87E-03	2.58E-04	5.04E-02	3.19E-02
	106	1.89E-03	2.09E-04	-3.05E-03	3.92E-02
	110	1.64E-03	1.95E-04	-2.74E-02	4.20E-02
	114	9.28E-04	1.45E-04	-1.31E-02	5.79E-02
	118	2.58E-04	7.54E-05	1.25E-02	1.19E-01
	122	7.54E-05	4.18E-05	-6.07E-02	2.01E-01
40	30	3.12E-02	7.65E-04	-1.06E-03	8.77E-03
	34	2.65E-02	7.05E-04	1.28E-02	9.49E-03
	38	2.36E-02	6.66E-04	-1.16E-02	1.00E-02
	42	2.12E-02	6.32E-04	-9.15E-03	1.06E-02
	46	1.89E-02	5.97E-04	8.66E-03	1.12E-02
	50	1.65E-02	5.57E-04	1.66E-02	1.20E-02
	54	1.48E-02	5.29E-04	2.36E-02	1.26E-02
	58	1.32E-02	4.98E-04	6.29E-03	1.34E-02
	62	1.13E-02	4.62E-04	-4.45E-03	1.44E-02
	66	9.86E-03	4.31E-04	1.30E-02	1.55E-02
	70	8.50E-03	4.00E-04	1.95E-03	1.67E-02
	74	7.46E-03	3.75E-04	1.15E-02	1.78E-02
	78	5.98E-03	3.36E-04	3.23E-02	1.99E-02
	82	5.29E-03	3.16E-04	-5.86E-03	2.11E-02
	86	4.25E-03	2.83E-04	1.50E-02	2.36E-02
	90	3.42E-03	2.54E-04	4.39E-02	2.62E-02
	94	2.92E-03	2.35E-04	-4.05E-03	2.84E-02
	98	2.00E-03	1.94E-04	1.32E-01	3.43E-02

	102	1.63E-03	1.75E-04	1.15E-01	3.82E-02
	106	1.12E-03	1.45E-04	1.21E-01	4.59E-02
	110	8.57E-04	1.27E-04	2.49E-01	5.22E-02
	114	3.46E-04	8.04E-05	8.78E-02	8.44E-02
50	30	2.41E-02	9.10E-04	8.80E-03	1.56E-02
	34	2.05E-02	8.41E-04	1.11E-02	1.36E-02
	38	1.71E-02	7.69E-04	-6.05E-02	1.46E-02
	42	1.51E-02	7.22E-04	-1.06E-02	1.60E-02
	46	1.27E-02	6.63E-04	2.65E-02	1.70E-02
	50	1.08E-02	6.11E-04	-1.97E-02	1.85E-02
	54	9.53E-03	5.74E-04	5.56E-02	2.00E-02
	58	7.93E-03	5.24E-04	-2.20E-02	2.13E-02
	62	6.80E-03	4.85E-04	2.97E-02	2.34E-02
	66	5.86E-03	4.50E-04	-1.19E-02	2.52E-02
	70	4.72E-03	4.04E-04	-1.56E-02	2.72E-02
	74	3.76E-03	3.61E-04	-1.06E-01	3.02E-02
	78	2.99E-03	3.21E-04	-3.62E-02	3.40E-02
	82	2.57E-03	2.98E-04	-1.81E-02	3.81E-02
	86	1.81E-03	2.50E-04	-2.42E-01	4.08E-02
	90	1.58E-03	2.34E-04	1.87E-03	4.96E-02
	94	9.61E-04	1.82E-04	1.70E-02	5.24E-02
	98	7.01E-04	1.56E-04	-1.01E-01	6.69E-02
	102	4.68E-04	1.27E-04	-1.53E-02	7.83E-02
	106	3.81E-04	1.12E-04	-1.52E-01	9.82E-02
	110	2.51E-04	9.31E-05	-1.16E-01	1.18E-01
60	30	1.80E-02	5.01E-04	-8.08E-03	1.15E-02
	34	1.44E-02	4.47E-04	-1.26E-02	9.94E-03
	38	1.20E-02	4.08E-04	-1.52E-02	1.11E-02
	42	9.87E-03	3.71E-04	4.95E-04	1.22E-02
	46	8.24E-03	3.39E-04	-3.44E-02	1.34E-02
	50	6.95E-03	3.11E-04	-3.34E-02	1.46E-02
	54	5.65E-03	2.81E-04	-5.17E-02	1.59E-02
	58	4.68E-03	2.56E-04	-1.53E-02	1.76E-02
	62	3.67E-03	2.26E-04	-4.31E-02	1.93E-02
	66	2.98E-03	2.04E-04	-1.07E-01	2.17E-02
	70	2.52E-03	1.88E-04	6.67E-03	2.42E-02
	74	1.76E-03	1.57E-04	-1.61E-02	2.64E-02
	78	1.45E-03	1.42E-04	-7.24E-02	3.14E-02
	82	1.18E-03	1.28E-04	-5.32E-02	3.46E-02
	86	7.75E-04	1.04E-04	-6.01E-02	3.86E-02
	90	5.71E-04	8.89E-05	-1.87E-01	4.72E-02
	94	3.73E-04	7.22E-05	-1.30E-01	5.60E-02
	98	2.69E-04	6.11E-05	3.76E-02	6.88E-02
	102	1.45E-04	4.49E-05	-1.97E-02	8.11E-02
	106	-9.11E-02	1.55E-01	-5.06E-02	1.11E-01
	110	-3.38E-01	2.18E-01	-9.11E-02	1.55E-01

80	30	8.37E-03	2.54E-04	-1.52E-03	1.10E-02
	34	6.07E-03	2.17E-04	-3.90E+00	5.00E+01
	38	4.67E-03	1.90E-04	-8.64E-03	1.46E-02
	42	3.61E-03	1.67E-04	8.35E-03	1.66E-02
	46	2.76E-03	1.46E-04	3.82E-02	1.89E-02
	50	2.15E-03	1.29E-04	-4.53E-02	2.15E-02
	54	1.51E-03	1.08E-04	-4.54E-02	2.56E-02
	58	1.13E-03	9.40E-05	-7.61E-02	2.94E-02
	62	8.44E-04	8.11E-05	-8.25E-02	3.40E-02
	66	6.46E-04	7.10E-05	-1.09E-01	3.88E-02
	70	4.03E-04	5.60E-05	-5.63E-02	4.95E-02
	74	2.53E-04	4.43E-05	-4.17E-02	6.30E-02
	78	1.71E-04	3.61E-05	-7.88E-02	7.86E-02
	82	1.16E-04	3.01E-05	-2.79E-01	8.97E-02
	86	8.48E-05	2.57E-05	-1.61E-02	1.07E-01
	90	5.17E-05	2.01E-05	2.45E-02	1.37E-01
	94	3.41E-05	1.61E-05	1.40E-01	1.78E-01
100	30	3.55E-03	1.31E-04	1.51E-02	1.37E-02
	34	2.44E-03	1.09E-04	-1.07E-02	1.62E-02
	38	1.68E-03	9.03E-05	3.64E-02	1.96E-02
	42	1.17E-03	7.58E-05	2.03E-03	2.31E-02
	46	8.49E-04	6.44E-05	-8.72E-03	2.72E-02
	50	6.04E-04	5.44E-05	-2.29E-02	3.21E-02
	54	4.31E-04	4.60E-05	1.04E-02	3.78E-02
	58	2.75E-04	3.67E-05	-1.38E-02	4.77E-02
	62	1.93E-04	3.08E-05	-1.66E-02	5.63E-02
	66	1.20E-04	2.42E-05	7.38E-02	7.18E-02
	70	6.63E-05	1.80E-05	2.31E-01	9.64E-02
	74	5.53E-05	1.64E-05	-1.11E-01	1.08E-01
	78	3.07E-05	1.23E-05	2.18E-01	1.40E-01
	82	1.60E-05	8.83E-06	-4.95E-01	1.84E-01
	86	1.11E-05	7.37E-06	-3.64E+00	5.02E+01

A.3 Experimental data for $^{59}\text{Co}(\bar{p}, ^3\text{He})$ at an incident energy of 160 MeV

Angle [Deg]	Energy [MeV]	Cross section (σ) [mb sr ⁻¹ MeV ⁻¹]	Statistical error on σ	Analysing power (A_y)	Statistical error on A_y
25	30	3.97E-02	1.01E-03	-4.25E-03	9.40E-03
	34	3.34E-02	9.30E-04	5.69E-03	1.01E-02
	38	3.12E-02	8.98E-04	2.22E-04	1.04E-02
	42	2.83E-02	8.56E-04	3.30E-02	1.09E-02
	46	2.63E-02	8.26E-04	2.36E-02	1.13E-02
	50	2.45E-02	7.98E-04	-1.66E-02	1.16E-02
	54	2.31E-02	7.74E-04	2.04E-02	1.20E-02
	58	2.12E-02	7.42E-04	3.66E-02	1.25E-02
	62	1.99E-02	7.20E-04	5.79E-03	1.29E-02
	66	1.82E-02	6.88E-04	-9.11E-03	1.35E-02
	70	1.67E-02	6.59E-04	5.81E-03	1.41E-02
	74	1.56E-02	6.36E-04	1.48E-02	1.46E-02
	78	1.39E-02	6.02E-04	1.50E-02	1.54E-02
	82	1.35E-02	5.94E-04	5.75E-02	1.56E-02
	86	1.22E-02	5.64E-04	4.65E-02	1.64E-02
	90	1.10E-02	5.35E-04	-1.42E-02	1.73E-02
	94	1.03E-02	5.18E-04	5.48E-03	1.78E-02
	98	9.06E-03	4.86E-04	1.11E-02	1.91E-02
	102	8.14E-03	4.61E-04	1.35E-02	2.01E-02
	106	7.19E-03	4.33E-04	8.79E-03	2.14E-02
	110	6.26E-03	4.04E-04	3.34E-02	2.29E-02
	114	5.83E-03	3.90E-04	-4.27E-03	2.37E-02
	118	4.85E-03	3.56E-04	6.52E-03	2.60E-02
	122	4.23E-03	3.32E-04	-2.60E-02	2.78E-02
	126	3.49E-03	3.02E-04	4.10E-02	3.05E-02
	130	2.97E-03	2.79E-04	9.93E-02	3.30E-02
	134	2.35E-03	2.48E-04	-7.96E-02	3.73E-02
	138	3.97E-02	1.01E-03	5.59E-02	4.03E-02
	142	3.34E-02	9.30E-04	-5.60E-02	4.48E-02
	146	3.12E-02	8.98E-04	2.87E-02	6.11E-02
	150	2.83E-02	8.56E-04	4.83E-01	9.87E-02
35	30	3.52E-02	9.09E-04	4.36E-03	9.69E-03
	34	2.94E-02	8.36E-04	-4.14E-03	1.04E-02
	38	2.63E-02	7.92E-04	-1.14E-02	1.09E-02
	42	2.40E-02	7.56E-04	9.23E-03	1.14E-02
	46	2.19E-02	7.24E-04	1.74E-02	1.19E-02
	50	2.02E-02	6.94E-04	7.23E-04	1.24E-02
	54	1.82E-02	6.60E-04	-2.87E-02	1.30E-02
	58	1.64E-02	6.26E-04	-1.59E-02	1.37E-02
	62	1.49E-02	5.97E-04	1.50E-02	1.44E-02
	66	1.39E-02	5.77E-04	-1.34E-02	1.48E-02
	70	1.23E-02	5.43E-04	-3.55E-03	1.57E-02

	74	1.16E-02	5.28E-04	-1.23E-02	1.62E-02
	78	9.61E-03	4.80E-04	1.18E-02	1.79E-02
	82	8.74E-03	4.57E-04	1.12E-02	1.87E-02
	86	7.97E-03	4.38E-04	5.33E-03	1.95E-02
	90	6.63E-03	3.99E-04	1.38E-02	2.14E-02
	94	5.71E-03	3.70E-04	5.72E-02	2.30E-02
	98	5.17E-03	3.52E-04	8.13E-03	2.42E-02
	102	4.38E-03	3.24E-04	-2.33E-02	2.63E-02
	106	3.73E-03	2.99E-04	1.56E-02	2.84E-02
	110	3.21E-03	2.78E-04	-2.46E-03	3.06E-02
	114	2.55E-03	2.48E-04	-3.27E-02	3.44E-02
	118	2.29E-03	2.35E-04	1.35E-02	3.63E-02
	122	1.70E-03	2.02E-04	-9.80E-02	4.19E-02
	126	1.29E-03	1.76E-04	5.43E-02	4.84E-02
	130	9.59E-04	1.52E-04	1.19E-02	5.60E-02
	134	8.09E-04	1.39E-04	5.98E-02	6.12E-02
	138	3.52E-02	9.09E-04	2.19E-01	6.90E-02
	142	2.94E-02	8.36E-04	2.27E-01	9.21E-02
	146	2.63E-02	7.92E-04	2.71E-01	1.39E-01
40	30	3.19E-02	9.37E-04	1.44E-02	1.11E-02
	34	2.71E-02	8.71E-04	-6.57E-03	1.17E-02
	38	2.38E-02	8.16E-04	1.87E-02	1.24E-02
	42	2.14E-02	7.75E-04	-1.21E-02	1.30E-02
	46	1.97E-02	7.43E-04	-2.84E-02	1.36E-02
	50	1.76E-02	7.03E-04	1.63E-02	1.43E-02
	54	1.59E-02	6.67E-04	-2.38E-02	1.51E-02
	58	1.44E-02	6.38E-04	-1.85E-02	1.57E-02
	62	1.23E-02	5.89E-04	2.14E-02	1.71E-02
	66	1.12E-02	5.62E-04	4.23E-04	1.79E-02
	70	9.96E-03	5.30E-04	1.66E-02	1.90E-02
	74	8.84E-03	5.00E-04	-4.09E-03	2.00E-02
	78	7.99E-03	4.75E-04	5.08E-03	2.11E-02
	82	6.89E-03	4.41E-04	-4.54E-02	2.27E-02
	86	6.21E-03	4.19E-04	-6.72E-02	2.39E-02
	90	5.36E-03	3.89E-04	1.64E-03	2.58E-02
	94	4.44E-03	3.54E-04	-7.94E-02	2.82E-02
	98	3.94E-03	3.33E-04	-4.50E-02	3.01E-02
	102	3.20E-03	3.01E-04	-1.10E-01	3.32E-02
	106	2.75E-03	2.78E-04	-8.94E-02	3.59E-02
	110	2.19E-03	2.49E-04	-1.16E-01	4.00E-02
	114	1.80E-03	2.26E-04	-6.79E-02	4.43E-02
	118	1.51E-03	2.06E-04	-9.06E-02	4.83E-02
	122	1.10E-03	1.76E-04	-5.52E-02	5.67E-02
	126	9.43E-04	1.63E-04	-4.38E-02	6.14E-02
	130	6.92E-04	1.40E-04	-4.64E-02	7.20E-02
	134	3.46E-04	9.89E-05	-2.81E-01	9.95E-02
	138	3.19E-02	9.37E-04	-2.15E-01	1.15E-01
	142	2.71E-02	8.71E-04	1.26E-02	1.39E-01

50	30	2.66E-02	8.63E-04	-2.58E-02	1.22E-02
	34	2.10E-02	7.69E-04	-2.09E-02	1.35E-02
	38	1.87E-02	7.27E-04	-2.30E-03	1.42E-02
	42	1.65E-02	6.85E-04	-2.31E-02	1.50E-02
	46	1.45E-02	6.42E-04	-4.70E-02	1.60E-02
	50	1.29E-02	6.05E-04	-1.19E-02	1.70E-02
	54	1.09E-02	5.58E-04	2.56E-03	1.84E-02
	58	9.90E-03	5.31E-04	-1.87E-02	1.93E-02
	62	8.42E-03	4.89E-04	-6.28E-02	2.10E-02
	66	7.19E-03	4.53E-04	-1.26E-02	2.26E-02
	70	6.17E-03	4.19E-04	-3.97E-02	2.44E-02
	74	5.40E-03	3.92E-04	-7.13E-02	2.62E-02
	78	4.27E-03	3.49E-04	1.95E-02	2.92E-02
	82	3.84E-03	3.32E-04	3.56E-03	3.07E-02
	86	3.32E-03	3.08E-04	-8.78E-02	3.30E-02
	90	2.63E-03	2.74E-04	-9.26E-02	3.69E-02
	94	2.22E-03	2.52E-04	-4.81E-02	4.02E-02
	98	1.83E-03	2.29E-04	-1.08E-01	4.45E-02
	102	1.32E-03	1.94E-04	-3.12E-02	5.24E-02
	106	1.19E-03	1.84E-04	-3.05E-02	5.52E-02
	110	8.32E-04	1.54E-04	-1.41E-01	6.58E-02
	114	6.34E-04	1.35E-04	-2.82E-01	7.40E-02
	118	4.66E-04	1.16E-04	-1.91E-01	8.72E-02
	122	3.44E-04	9.93E-05	-2.31E-01	1.00E-01
	126	2.69E-04	8.78E-05	-1.67E-01	1.17E-01
	130	1.47E-04	6.48E-05	5.54E-02	1.56E-01
60	30	2.02E-02	5.41E-04	-1.26E-03	1.04E-02
	34	1.59E-02	4.83E-04	-7.30E-03	1.13E-02
	38	1.36E-02	4.48E-04	1.59E-02	1.22E-02
	42	1.12E-02	4.08E-04	3.10E-02	1.33E-02
	46	1.00E-02	3.85E-04	-1.33E-03	1.41E-02
	50	8.69E-03	3.59E-04	-1.31E-02	1.50E-02
	54	7.31E-03	3.30E-04	-5.36E-02	1.63E-02
	58	6.02E-03	2.99E-04	-8.68E-02	1.80E-02
	62	5.05E-03	2.75E-04	-5.40E-02	1.95E-02
	66	4.22E-03	2.51E-04	2.61E-02	2.14E-02
	70	3.68E-03	2.34E-04	-4.50E-03	2.30E-02
	74	3.05E-03	2.13E-04	-7.21E-02	2.53E-02
	78	2.28E-03	1.85E-04	-1.21E-02	2.89E-02
	82	1.92E-03	1.69E-04	-2.90E-02	3.17E-02
	86	1.51E-03	1.50E-04	-1.50E-02	3.55E-02
	90	1.23E-03	1.36E-04	-1.17E-01	3.93E-02
	94	9.42E-04	1.19E-04	2.06E-03	4.49E-02
	98	7.15E-04	1.04E-04	-1.18E-01	5.12E-02
	102	5.52E-04	9.08E-05	-2.85E-02	5.89E-02
	106	3.47E-04	7.22E-05	-1.87E-01	7.30E-02
	110	2.55E-04	6.19E-05	-1.19E-01	8.54E-02

	114	2.38E-04	5.98E-05	-9.47E-02	8.86E-02
	118	1.45E-04	4.65E-05	-6.05E-02	1.15E-01
	122	7.32E-05	3.30E-05	-1.97E-01	1.62E-01
	126	6.38E-05	3.10E-05	-1.57E-01	1.71E-01
	130	4.51E-05	2.59E-05	3.91E-02	2.10E-01

A.4 Experimental data for $^{93}\text{Nb}(\bar{p}, ^3\text{He})$ at an incident energy of 100 MeV

Angle [Deg]	Energy [MeV]	Cross section (σ) [mb sr ⁻¹ MeV ⁻¹]	Statistical error on σ	Analysing power (A_y)	Statistical error on A_y
15	34	4.95E+01	6.47E-01	-1.11E-02	1.79E-02
	38	4.64E+01	6.26E-01	3.29E-02	1.85E-02
	42	4.58E+01	6.22E-01	4.35E-02	1.86E-02
	46	4.48E+01	6.15E-01	-1.02E-02	1.88E-02
	50	4.40E+01	6.09E-01	1.71E-02	1.90E-02
	54	4.13E+01	5.91E-01	1.58E-02	1.96E-02
	58	3.93E+01	5.76E-01	1.83E-02	2.01E-02
	62	3.89E+01	5.73E-01	5.01E-02	2.02E-02
	66	3.81E+01	5.67E-01	5.84E-02	2.04E-02
	70	3.76E+01	5.63E-01	2.91E-02	2.06E-02
	74	3.78E+01	5.65E-01	1.74E-03	2.05E-02
	78	3.88E+01	5.73E-01	-1.91E-02	2.02E-02
	82	3.88E+01	5.72E-01	-3.76E-02	2.03E-02
	86	3.93E+01	5.76E-01	-1.16E-01	2.00E-02
	90	4.66E+01	6.28E-01	3.39E-02	1.85E-02
20	34	4.48E+01	2.59E-01	1.54E-02	8.24E-03
	38	4.31E+01	2.54E-01	1.12E-02	8.41E-03
	42	4.14E+01	2.49E-01	3.10E-02	8.57E-03
	46	3.90E+01	2.41E-01	4.05E-02	8.83E-03
	50	3.75E+01	2.37E-01	2.63E-02	9.01E-03
	54	3.58E+01	2.31E-01	2.20E-02	9.22E-03
	58	3.39E+01	2.25E-01	4.81E-02	9.47E-03
	62	3.26E+01	2.21E-01	6.99E-02	9.64E-03
	66	3.02E+01	2.12E-01	6.08E-02	1.00E-02
	70	2.86E+01	2.07E-01	4.56E-02	1.03E-02
	74	2.79E+01	2.04E-01	3.02E-02	1.04E-02
	78	2.66E+01	1.99E-01	3.68E-02	1.07E-02
	82	2.66E+01	1.99E-01	-4.95E-03	1.07E-02
	86	2.65E+01	1.99E-01	-4.68E-02	1.07E-02
	90	2.74E+01	2.02E-01	1.06E-01	1.05E-02
25	34	4.12E+01	2.16E-01	1.86E-02	7.76E-03
	38	3.86E+01	2.09E-01	3.32E-02	8.01E-03
	42	3.64E+01	2.03E-01	5.08E-02	8.25E-03
	46	3.42E+01	1.96E-01	3.67E-02	8.52E-03
	50	3.22E+01	1.91E-01	4.15E-02	8.79E-03
	54	3.03E+01	1.85E-01	3.10E-02	9.06E-03
	58	2.79E+01	1.77E-01	7.11E-02	9.42E-03
	62	2.58E+01	1.71E-01	5.35E-02	9.81E-03
	66	2.38E+01	1.64E-01	7.31E-02	1.02E-02
	70	2.17E+01	1.57E-01	8.66E-02	1.07E-02
	74	2.04E+01	1.52E-01	8.41E-02	1.10E-02

	78	1.83E+01	1.44E-01	9.07E-02	1.16E-02
	82	1.71E+01	1.39E-01	7.16E-02	1.21E-02
	86	1.69E+01	1.38E-01	1.13E-02	1.21E-02
	90	1.54E+01	1.32E-01	2.58E-01	1.25E-02
30	34	3.73E+01	1.95E-01	1.84E-02	7.76E-03
	38	3.39E+01	1.86E-01	3.52E-02	8.13E-03
	42	3.19E+01	1.80E-01	4.28E-02	8.39E-03
	46	2.91E+01	1.72E-01	3.91E-02	8.79E-03
	50	2.75E+01	1.67E-01	5.35E-02	9.04E-03
	54	2.50E+01	1.59E-01	5.78E-02	9.48E-03
	58	2.27E+01	1.52E-01	7.00E-02	9.94E-03
	62	2.06E+01	1.45E-01	9.38E-02	1.04E-02
	66	1.83E+01	1.37E-01	1.17E-01	1.10E-02
	70	1.60E+01	1.28E-01	1.28E-01	1.18E-02
	74	1.42E+01	1.20E-01	1.39E-01	1.25E-02
	78	1.24E+01	1.12E-01	1.61E-01	1.34E-02
	82	1.10E+01	1.06E-01	1.98E-01	1.42E-02
	86	9.92E+00	1.01E-01	1.30E-01	1.50E-02
	90	8.95E+00	9.55E-02	3.46E-01	1.54E-02
35	34	3.21E+01	1.74E-01	1.94E-02	7.44E-03
	38	2.96E+01	1.67E-01	2.57E-02	7.74E-03
	42	2.68E+01	1.59E-01	4.07E-02	8.14E-03
	46	2.49E+01	1.53E-01	5.63E-02	8.43E-03
	50	2.25E+01	1.46E-01	4.88E-02	8.89E-03
	54	1.99E+01	1.37E-01	5.87E-02	9.44E-03
	58	1.78E+01	1.30E-01	6.80E-02	9.98E-03
	62	1.58E+01	1.22E-01	9.72E-02	1.06E-02
	66	1.36E+01	1.13E-01	8.39E-02	1.14E-02
	70	1.18E+01	1.05E-01	1.39E-01	1.22E-02
	74	1.01E+01	9.76E-02	1.46E-01	1.32E-02
	78	8.30E+00	8.85E-02	1.85E-01	1.45E-02
	82	7.05E+00	8.16E-02	2.25E-01	1.57E-02
	86	5.76E+00	7.37E-02	3.08E-01	1.71E-02
	90	5.28E+00	7.06E-02	4.60E-01	1.73E-02
40	34	2.88E+01	1.80E-01	1.76E-02	8.59E-03
	38	2.61E+01	1.72E-01	3.83E-02	9.03E-03
	42	2.31E+01	1.62E-01	3.37E-02	9.59E-03
	46	2.07E+01	1.53E-01	5.70E-02	1.01E-02
	50	1.82E+01	1.44E-01	5.35E-02	1.08E-02
	54	1.60E+01	1.34E-01	8.30E-02	1.15E-02
	58	1.39E+01	1.25E-01	5.69E-02	1.23E-02
	62	1.20E+01	1.17E-01	7.93E-02	1.33E-02
	66	1.01E+01	1.07E-01	8.13E-02	1.45E-02
	70	8.46E+00	9.78E-02	1.24E-01	1.58E-02
	74	6.97E+00	8.87E-02	1.41E-01	1.74E-02
	78	5.57E+00	7.94E-02	1.81E-01	1.94E-02

	82	4.55E+00	7.17E-02	1.82E-01	2.14E-02
	86	3.50E+00	6.29E-02	2.84E-01	2.41E-02
	90	3.10E+00	5.92E-02	4.91E-01	2.45E-02
50	34	2.23E+01	8.01E-02	1.72E-02	5.47E-03
	38	1.93E+01	7.46E-02	2.64E-02	5.87E-03
	42	1.67E+01	6.93E-02	3.28E-02	6.32E-03
	46	1.45E+01	6.47E-02	3.13E-02	6.76E-03
	50	1.23E+01	5.96E-02	6.19E-02	7.35E-03
	54	1.03E+01	5.46E-02	5.34E-02	8.01E-03
	58	8.73E+00	5.02E-02	7.35E-02	8.72E-03
	62	7.38E+00	4.61E-02	6.88E-02	9.49E-03
	66	6.02E+00	4.17E-02	7.95E-02	1.05E-02
	70	4.91E+00	3.76E-02	1.21E-01	1.16E-02
	74	3.91E+00	3.36E-02	1.31E-01	1.30E-02
	78	2.95E+00	2.92E-02	1.61E-01	1.49E-02
	82	2.29E+00	2.57E-02	2.03E-01	1.69E-02
	86	1.63E+00	2.17E-02	2.55E-01	1.99E-02
	90	1.44E+00	2.04E-02	4.37E-01	2.06E-02
60	34	1.60E+01	5.06E-02	1.62E-02	4.81E-03
	38	1.33E+01	4.62E-02	1.91E-02	5.27E-03
	42	1.12E+01	4.23E-02	1.65E-02	5.76E-03
	46	9.21E+00	3.84E-02	4.65E-02	6.34E-03
	50	7.65E+00	3.50E-02	3.55E-02	6.95E-03
	54	6.27E+00	3.17E-02	3.75E-02	7.68E-03
	58	5.01E+00	2.83E-02	4.05E-02	8.59E-03
	62	4.03E+00	2.54E-02	4.33E-02	9.58E-03
	66	3.13E+00	2.24E-02	7.19E-02	1.09E-02
	70	2.46E+00	1.99E-02	5.80E-02	1.22E-02
	74	1.87E+00	1.73E-02	7.57E-02	1.41E-02
	78	1.35E+00	1.47E-02	8.29E-02	1.65E-02
	82	1.00E+00	1.27E-02	8.99E-02	1.92E-02
	86	6.91E-01	1.05E-02	1.83E-01	2.30E-02
	90	5.30E-01	9.21E-03	3.43E-01	2.58E-02
80	34	7.65E+00	2.31E-02	9.78E-03	4.58E-03
	38	5.88E+00	2.02E-02	1.55E-02	5.23E-03
	42	4.51E+00	1.77E-02	1.17E-02	5.97E-03
	46	3.47E+00	1.55E-02	1.26E-02	6.81E-03
	50	2.63E+00	1.35E-02	8.43E-03	7.82E-03
	54	1.97E+00	1.17E-02	6.92E-03	9.04E-03
	58	1.45E+00	1.01E-02	1.56E-02	1.05E-02
	62	1.06E+00	8.60E-03	2.02E-02	1.23E-02
	66	7.79E-01	7.36E-03	4.74E-03	1.44E-02
	70	5.61E-01	6.25E-03	1.44E-02	1.69E-02
	74	4.04E-01	5.30E-03	2.01E-02	2.00E-02
	78	2.80E-01	4.41E-03	-1.77E-02	2.40E-02
	82	1.91E-01	3.65E-03	6.39E-02	2.90E-02

	86	1.44E-01	3.17E-03	9.82E-02	3.34E-02
	90	8.71E-02	2.46E-03	2.04E-01	4.26E-02
100	34	3.29E+00	1.18E-02	1.43E-02	4.77E-03
	38	2.35E+00	9.97E-03	2.26E-02	5.64E-03
	42	1.68E+00	8.44E-03	2.87E-02	6.67E-03
	46	1.21E+00	7.17E-03	3.13E-02	7.86E-03
	50	8.75E-01	6.09E-03	3.63E-02	9.26E-03
	54	6.17E-01	5.11E-03	3.97E-02	1.10E-02
	58	4.38E-01	4.31E-03	3.17E-02	1.31E-02
	62	2.95E-01	3.54E-03	5.50E-02	1.60E-02
	66	2.10E-01	2.98E-03	5.35E-02	1.89E-02
	70	1.43E-01	2.46E-03	8.51E-02	2.29E-02
	74	1.01E-01	2.06E-03	1.10E-01	2.74E-02
	78	6.90E-02	1.71E-03	1.78E-01	3.30E-02
	82	4.76E-02	1.42E-03	8.70E-02	3.99E-02
	86	3.36E-02	1.19E-03	1.85E-01	4.71E-02
	90	2.25E-02	9.77E-04	1.54E-01	5.77E-02
120	34	1.88E+00	1.01E-02	4.62E-02	7.11E-03
	38	1.25E+00	8.21E-03	4.43E-02	8.72E-03
	42	8.38E-01	6.72E-03	7.92E-02	1.07E-02
	46	5.61E-01	5.50E-03	7.08E-02	1.30E-02
	50	3.70E-01	4.47E-03	1.06E-01	1.60E-02
	54	2.50E-01	3.67E-03	9.23E-02	1.95E-02
	58	1.60E-01	2.94E-03	9.12E-02	2.46E-02
	62	1.07E-01	2.40E-03	1.06E-01	3.00E-02
	66	6.64E-02	1.89E-03	9.76E-02	3.85E-02
	70	4.62E-02	1.58E-03	1.13E-01	4.56E-02
	74	2.98E-02	1.27E-03	1.66E-01	5.71E-02
	78	1.99E-02	1.04E-03	5.00E-02	7.12E-02
	82	1.40E-02	8.69E-04	4.14E-02	8.30E-02
	86	9.16E-03	7.02E-04	3.59E-01	1.02E-01
	90	5.60E-03	5.49E-04	2.10E-01	1.30E-01
140	34	1.37E+00	8.55E-03	5.07E-02	8.28E-03
	38	8.51E-01	6.73E-03	4.83E-02	1.05E-02
	42	5.45E-01	5.39E-03	8.83E-02	1.31E-02
	46	3.55E-01	4.35E-03	8.53E-02	1.63E-02
	50	2.30E-01	3.50E-03	7.13E-02	2.03E-02
	54	1.52E-01	2.85E-03	6.21E-02	2.49E-02
	58	1.01E-01	2.32E-03	9.32E-02	3.05E-02
	62	6.78E-02	1.90E-03	1.32E-01	3.71E-02
	66	4.64E-02	1.57E-03	1.12E-01	4.49E-02
	70	3.19E-02	1.30E-03	1.84E-01	5.42E-02
	74	2.46E-02	1.15E-03	1.89E-01	6.18E-02
	78	1.81E-02	9.81E-04	1.25E-01	7.52E-02
	82	1.65E-02	9.38E-04	2.43E-01	7.70E-02
	86	1.36E-02	8.51E-04	3.71E-01	8.88E-02

A.5 Experimental data for $^{93}\text{Nb}(\bar{p}, ^3\text{He})$ at an incident energy of 130 MeV

Angle [Deg]	Energy [MeV]	Cross section (σ) [mb sr ⁻¹ MeV ⁻¹]	Statistical error on σ	Analysing power (A_y)	Statistical error on A_y
15	34	5.92E-02	2.37E-03	4.42E-02	1.45E-02
	38	5.13E-02	2.21E-03	-1.23E-03	1.54E-02
	42	4.96E-02	2.18E-03	1.12E-02	1.56E-02
	46	4.61E-02	2.10E-03	4.55E-02	1.62E-02
	50	4.25E-02	2.02E-03	1.84E-03	1.69E-02
	54	4.03E-02	1.96E-03	-1.80E-02	1.73E-02
	58	3.73E-02	1.89E-03	1.84E-02	1.79E-02
	62	3.66E-02	1.87E-03	1.19E-02	1.82E-02
	66	3.44E-02	1.81E-03	2.57E-02	1.87E-02
	70	3.30E-02	1.78E-03	1.97E-02	1.91E-02
	74	3.10E-02	1.72E-03	2.55E-02	1.96E-02
	78	3.02E-02	1.70E-03	3.71E-02	1.99E-02
	82	2.79E-02	1.63E-03	2.05E-02	2.08E-02
	86	2.69E-02	1.61E-03	2.95E-02	2.11E-02
	90	2.67E-02	1.60E-03	-3.07E-02	2.13E-02
	94	2.60E-02	1.58E-03	-1.77E-02	2.15E-02
	98	2.49E-02	1.55E-03	-4.34E-02	2.19E-02
	102	2.55E-02	1.56E-03	-7.85E-02	2.16E-02
	106	2.37E-02	1.51E-03	-1.13E-01	2.25E-02
	110	2.29E-02	1.48E-03	-1.13E-01	2.28E-02
	114	1.98E-02	1.38E-03	3.79E-02	2.46E-02
20	34	4.53E-02	2.33E-03	3.11E-02	1.85E-02
	38	3.93E-02	2.17E-03	6.94E-02	1.97E-02
	42	3.69E-02	2.11E-03	2.22E-02	2.03E-02
	46	3.50E-02	2.05E-03	2.02E-02	2.09E-02
	50	3.32E-02	2.00E-03	1.59E-02	2.15E-02
	54	2.87E-02	1.86E-03	8.03E-02	2.30E-02
	58	2.85E-02	1.85E-03	3.20E-02	2.30E-02
	62	2.80E-02	1.83E-03	3.65E-02	2.34E-02
	66	2.55E-02	1.75E-03	-3.09E-02	2.43E-02
	70	2.35E-02	1.68E-03	5.23E-02	2.54E-02
	74	2.16E-02	1.61E-03	8.59E-02	2.65E-02
	78	2.07E-02	1.58E-03	5.44E-02	2.71E-02
	82	1.92E-02	1.52E-03	5.51E-02	2.80E-02
	86	1.74E-02	1.45E-03	3.66E-02	2.94E-02
	90	1.68E-02	1.42E-03	1.34E-01	3.00E-02
	94	1.44E-02	1.32E-03	4.03E-02	3.23E-02
	98	1.53E-02	1.36E-03	3.00E-02	3.15E-02
	102	1.24E-02	1.22E-03	-3.58E-02	3.47E-02
	106	1.28E-02	1.24E-03	3.20E-02	3.43E-02
	110	1.13E-02	1.17E-03	-6.48E-02	3.67E-02
	114	9.46E-03	1.07E-03	5.44E-02	4.00E-02

25	34	5.90E-02	1.76E-03	8.13E-04	1.05E-02
	38	9.83E-02	2.22E-03	7.97E-03	8.87E-03
	42	8.08E-02	2.03E-03	2.07E-02	9.54E-03
	46	7.13E-02	1.91E-03	1.28E-02	9.99E-03
	50	6.27E-02	1.80E-03	2.41E-02	1.06E-02
	54	5.63E-02	1.71E-03	2.56E-02	1.11E-02
	58	5.18E-02	1.64E-03	5.09E-02	1.14E-02
	62	4.64E-02	1.56E-03	2.91E-02	1.20E-02
	66	4.25E-02	1.49E-03	6.60E-02	1.26E-02
	70	3.76E-02	1.40E-03	3.15E-02	1.33E-02
	74	3.50E-02	1.35E-03	5.69E-02	1.37E-02
	78	3.15E-02	1.28E-03	6.40E-02	1.45E-02
	82	2.88E-02	1.23E-03	9.77E-02	1.52E-02
	86	2.47E-02	1.13E-03	7.23E-02	1.65E-02
	90	2.20E-02	1.07E-03	1.14E-01	1.74E-02
	94	1.90E-02	9.97E-04	6.66E-02	1.86E-02
	98	1.68E-02	9.36E-04	1.74E-01	1.98E-02
	102	1.42E-02	8.62E-04	1.52E-01	2.14E-02
	106	1.22E-02	8.00E-04	1.16E-01	2.32E-02
	110	1.03E-02	7.35E-04	4.28E-02	2.53E-02
	114	7.54E-03	6.29E-04	2.53E-01	2.90E-02
	118	4.44E-03	4.82E-04	3.74E-01	3.69E-02
35	34	3.82E-02	1.50E-03	-3.98E-03	1.43E-02
	38	3.26E-02	1.39E-03	1.98E-02	1.53E-02
	42	2.86E-02	1.30E-03	2.89E-02	1.62E-02
	46	2.51E-02	1.22E-03	6.15E-02	1.73E-02
	50	2.32E-02	1.17E-03	4.53E-02	1.80E-02
	54	2.07E-02	1.11E-03	5.96E-02	1.90E-02
	58	1.90E-02	1.06E-03	8.72E-02	1.98E-02
	62	1.65E-02	9.87E-04	2.32E-02	2.14E-02
	66	1.44E-02	9.24E-04	5.47E-02	2.27E-02
	70	1.27E-02	8.69E-04	1.71E-03	2.42E-02
	74	1.05E-02	7.88E-04	-1.22E-02	2.67E-02
	78	9.47E-03	7.50E-04	4.80E-02	2.81E-02
	82	7.97E-03	6.88E-04	4.26E-02	3.05E-02
	86	7.15E-03	6.52E-04	5.17E-03	3.22E-02
	90	5.39E-03	5.65E-04	9.89E-02	3.72E-02
	94	4.85E-03	5.36E-04	7.44E-02	3.91E-02
	98	3.78E-03	4.73E-04	9.88E-02	4.44E-02
	102	2.92E-03	4.17E-04	6.52E-02	5.03E-02
	106	2.29E-03	3.69E-04	1.89E-01	5.66E-02
	110	1.59E-03	3.07E-04	6.32E-02	6.83E-02
	114	1.16E-03	2.62E-04	5.31E-01	7.47E-02
40	34	2.76E-02	8.54E-04	-8.39E-03	1.09E-02
	38	4.36E-02	1.05E-03	-8.88E-03	9.70E-03
	42	3.48E-02	9.42E-04	3.76E-02	1.05E-02

	46	2.95E-02	8.72E-04	2.91E-02	1.11E-02
	50	2.51E-02	8.06E-04	1.49E-02	1.20E-02
	54	2.15E-02	7.49E-04	5.57E-03	1.27E-02
	58	1.87E-02	6.98E-04	-6.64E-03	1.36E-02
	62	1.61E-02	6.48E-04	1.38E-02	1.46E-02
	66	1.37E-02	6.00E-04	1.60E-02	1.58E-02
	70	1.19E-02	5.58E-04	3.92E-02	1.71E-02
	74	9.82E-03	5.08E-04	3.53E-02	1.86E-02
	78	8.41E-03	4.70E-04	4.78E-02	2.01E-02
	82	6.79E-03	4.22E-04	3.94E-02	2.23E-02
	86	5.81E-03	3.91E-04	1.00E-01	2.41E-02
	90	4.32E-03	3.37E-04	1.20E-01	2.78E-02
	94	3.66E-03	3.11E-04	9.85E-02	3.01E-02
	98	2.81E-03	2.72E-04	1.23E-01	3.42E-02
	102	2.24E-03	2.43E-04	1.98E-01	3.81E-02
	106	1.45E-03	1.96E-04	9.42E-02	4.74E-02
	110	9.94E-04	1.62E-04	1.77E-01	5.66E-02
	114	7.00E-04	1.36E-04	5.75E-01	6.23E-02
	118	2.48E-04	8.07E-05	4.48E-01	1.11E-01
50	34	3.09E-02	5.18E-04	-7.82E-03	8.46E-03
	38	4.07E-02	6.52E-04	6.43E-03	7.91E-03
	42	3.12E-02	5.72E-04	5.40E-03	8.39E-03
	46	2.47E-02	5.08E-04	2.43E-03	8.86E-03
	50	1.89E-02	4.43E-04	1.76E-02	9.38E-03
	54	1.52E-02	3.97E-04	1.41E-02	9.91E-03
	58	1.21E-02	3.52E-04	1.77E-02	1.04E-02
	62	9.31E-03	3.08E-04	4.03E-02	1.12E-02
	66	7.21E-03	2.68E-04	8.47E-03	1.19E-02
	70	6.01E-03	2.45E-04	2.19E-02	1.28E-02
	74	4.81E-03	2.18E-04	4.98E-02	1.38E-02
	78	3.84E-03	1.94E-04	-1.88E-03	1.48E-02
	82	2.93E-03	1.68E-04	1.50E-02	1.62E-02
	86	2.25E-03	1.48E-04	1.23E-02	1.80E-02
	90	1.67E-03	1.27E-04	1.38E-02	2.00E-02
	94	1.20E-03	1.07E-04	-2.35E-02	2.28E-02
	98	8.49E-04	9.02E-05	3.65E-04	2.58E-02
	102	5.80E-04	7.45E-05	3.28E-02	3.12E-02
	106	3.96E-04	6.16E-05	-4.98E-02	3.64E-02
	110	2.47E-04	5.03E-05	6.80E-02	4.92E-02
	114	1.47E-04	3.81E-05	4.39E-02	5.98E-02
60	34	2.07E-02	5.17E-04	2.05E-02	9.26E-03
	38	1.64E-02	4.62E-04	7.65E-03	1.02E-02
	42	1.35E-02	4.21E-04	2.79E-02	1.12E-02
	46	1.13E-02	3.84E-04	9.40E-03	1.22E-02
	50	9.24E-03	3.48E-04	-6.02E-03	1.34E-02
	54	7.41E-03	3.12E-04	7.32E-03	1.50E-02
	58	6.30E-03	2.88E-04	4.03E-02	1.62E-02

	62	5.06E-03	2.58E-04	2.91E-02	1.81E-02
	66	4.19E-03	2.35E-04	4.36E-02	1.98E-02
	70	3.27E-03	2.08E-04	-7.50E-03	2.25E-02
	74	2.66E-03	1.87E-04	9.18E-02	2.49E-02
	78	1.98E-03	1.61E-04	-1.24E-02	2.89E-02
	82	1.69E-03	1.49E-04	-3.67E-02	3.12E-02
	86	1.22E-03	1.27E-04	-1.13E-01	3.67E-02
	90	8.66E-04	1.07E-04	-4.36E-02	4.38E-02
	94	5.63E-04	8.61E-05	-2.58E-01	5.33E-02
	98	3.74E-04	7.02E-05	-2.05E-01	6.58E-02
	102	2.31E-04	5.49E-05	1.30E-01	8.64E-02
	106	1.58E-04	4.55E-05	-4.50E-02	1.04E-01
80	34	1.09E-02	2.25E-04	2.35E-02	7.83E-03
	38	7.96E-03	1.94E-04	2.72E-02	8.91E-03
	42	5.93E-03	1.68E-04	2.58E-02	1.02E-02
	46	4.56E-03	1.47E-04	2.10E-02	1.16E-02
	50	3.52E-03	1.29E-04	-2.87E-02	1.32E-02
	54	2.62E-03	1.12E-04	3.98E-02	1.52E-02
	58	1.95E-03	9.64E-05	-2.32E-02	1.76E-02
	62	1.49E-03	8.43E-05	-3.04E-02	2.01E-02
	66	1.09E-03	7.22E-05	3.03E-02	2.35E-02
	70	7.98E-04	6.18E-05	-5.99E-02	2.74E-02
	74	5.92E-04	5.32E-05	-1.14E-03	3.19E-02
	78	4.09E-04	4.42E-05	2.37E-03	3.83E-02
	82	2.86E-04	3.70E-05	9.05E-03	4.56E-02
	86	1.91E-04	3.02E-05	-9.13E-02	5.59E-02
	90	1.12E-04	2.30E-05	9.75E-02	7.40E-02
100	34	5.06E-03	9.19E-05	1.79E-02	7.05E-03
	38	3.29E-03	7.48E-05	3.46E-02	8.44E-03
	42	2.27E-03	6.23E-05	2.19E-02	1.00E-02
	46	1.60E-03	5.24E-05	4.20E-02	1.19E-02
	50	1.11E-03	4.38E-05	5.46E-02	1.41E-02
	54	8.06E-04	3.73E-05	8.29E-02	1.65E-02
	58	5.54E-04	3.10E-05	5.29E-02	1.98E-02
	62	3.90E-04	2.60E-05	9.99E-02	2.36E-02
	66	2.69E-04	2.16E-05	1.56E-01	2.82E-02
	70	1.83E-04	1.78E-05	4.66E-02	3.43E-02
	74	1.18E-04	1.43E-05	-9.28E-03	4.32E-02
	78	8.69E-05	1.23E-05	6.92E-02	5.00E-02
	82	5.66E-05	9.90E-06	1.84E-01	6.20E-02
	86	3.08E-05	7.30E-06	4.99E-03	8.43E-02
	90	1.91E-05	5.75E-06	1.93E-02	1.08E-01
120	34	2.57E-03	1.55E-04	3.34E-02	2.34E-02
	38	1.64E-03	1.24E-04	9.58E-02	2.87E-02
	42	1.06E-03	1.00E-04	5.05E-02	3.52E-02
	46	6.42E-04	7.82E-05	7.49E-02	4.46E-02

	50	4.31E-04	6.40E-05	8.78E-02	5.47E-02
	54	3.09E-04	5.45E-05	1.47E-01	6.30E-02
	58	1.96E-04	4.34E-05	-1.66E-01	7.92E-02
	62	1.22E-04	3.43E-05	9.61E-02	9.99E-02
	66	9.54E-05	3.02E-05	2.91E-01	1.13E-01

REFERENCES

- [Agr96] An Introduction to Categorical Data
A Agresti
John Wiley & Sons (1996)
- [Are94] Pre-equilibrium excitation of nuclei in (p,α) and $(p,^3\text{He})$ reactions induced by
120, 160 and 200 MeV protons
G J Arendse
MSc Thesis (1994)
University of Stellenbosch
- [Are97] Nuclear distortions in the $(p,2p)$ knockout reaction on ^{208}Pb at an incident
energy of 200 MeV
G J Arendse
PhD Thesis (1997)
University of Stellenbosch
- [Bar71] Proceedings of the Third International Symposium on Polarization Phenomena
in Nuclear Reactions, Madison (1970)
H H Barschall and W Haeberli (1971)
- [Bis79] $^{17}\text{O}(^3\text{He},p)^{19}\text{Fe}$ and structure of ^{19}Fe
J N Bishop, L R Medsker and H T Fortune
Physical Review C 20 (1979) 1221
- [Ber77] Interactions for inelastic scattering derived from realistic potentials
G Bertsch, J Borysowicz, H McManus and W G Love
Nuclear Physics A284 (1977) 399

- [Bez00] Cross sections and analyzing power energy-sharing distributions of valence $(p,2p)$ -knockout from ^{208}Pb with a projectile of 200 MeV
J Bezuidenhout
MSc Thesis (2000)
University of Stellenbosch
- [Bon81] Analysis of precompound processes in (p,n) reactions with the statistical multistep direct emission theory
R Bonetti, M Camnasio, L Colli Milazzo and P E Hodgson
Physical Review C 24 (1981) 71
- [Bon89] The $^{58}\text{Ni}(p, \alpha)$ reaction mechanism through a study of the analyzing power
R Bonetti, F Crepsi and K I Kubo
Nuclear Physics A499 (1989) 381
- [Cha94] Continuum angular distributions in preequilibrium nuclear reactions: Physical basis for Kalbach systematic
M B Chadwick and P Obložinsky
Physical Review C 50 (1994) 2490
- [Coo81] Folding Model Analysis of triton and ^3He elastic scattering
J Cook and R J Griffiths
Nuclear Physics A366 (1981) 27-37
- [Coo87] Microscopic spin-orbit potentials for polarized ^3He elastic scattering
J Cook
Nuclear Physics A465 (1987) 207-220

- [Cow00] Multistep direct mechanism in ($\bar{p}, {}^3\text{He}$) inclusive reaction on ${}^{59}\text{Co}$ and ${}^{93}\text{Nb}$ at an incident energy of 100 MeV
A A Cowley, G F Steyn, S S Dimitrova, P E Hodgson, G J Arendse,
S V Förtsch, G C Hillhouse, J J Lawrie, R Neveling, W A Richer, J A Stander
and S M Wyngaardt
Physical Review C 62 (2000) 064605/1-6
- [Cow00a] Inclusive reaction ${}^{40}\text{Ca}(p, p'x)$ at an incident energy of 392 MeV
A A Cowley, G F Steyn, Y Watanabe, T Noro, K Tamura, M Kawabata,
K Hatanaka, H Sakaguchi, H Takeda and M Itoh
Physical Review C 62 (2000) 064604/1-5
- [Cow90] Continuum protons from the inclusive reaction ${}^{197}\text{Au}(p, p')$ at incident energies between of 100 and 200 MeV
A A Cowley, S V Förtsch, J J Lawrie, D M Whittal, J V Pilcher and
F D Smit
Z. Phys. A 336 (1990) 189-195
- [Cow91] Preequilibrium proton emission induced by 80 and 120 MeV protons incident on ${}^{90}\text{Zr}$
A A Cowley, A van Kent, J J Lawrie, S V Förtsch, D M Whittal, J V Pilcher,
F D Smit, W A Richter, R Lindsay, I J van Heerden, R Bonetti and
P E Hodgson
Physical Review C 43 (1991) 678
- [Cow96] Inclusive (\bar{p}, α) reactions on ${}^{27}\text{Al}$, ${}^{59}\text{Co}$ and ${}^{197}\text{Au}$ at incident energies of 120, 160 and 200 MeV
A A Cowley, G J Arendse, J W Koen, W A Richer, J A Stander, G F Steyn,
P Demetriou, P E Hodgson and Y Watanabe
Physical Review C 54 (1996) 778

- [Cow97] Inclusive (\bar{p} , ^3He) reactions on ^{59}Co and ^{197}Au at incident energies of 120, 160 and 200 MeV
A A Cowley, G J Arendse, G F Steyn, J A Stander, W A Richer,
S S Dimitrova, P Demetriou and P E Hodgson
Physical Review C 55 (1997) 1843
- [Cow98] Rescattering in knockout reactions as manifested in $^{40}\text{Ca}(p, p', p'')$ at an incident energy of 392 MeV
A A Cowley, J Arendse, R F Visser, G F Steyn, S V Förtsch, J J Lawrie,
J V Pilcher, T Noro, T Baba, K Hatanaka, M Kawabata, N Matsuoka,
Y Mizuno, M Nomachi, K Takahisa, K Tamura, Y Yuasa, H Sakaguchi,
M Itoh, H Takeda and Y Watanabe
Physical Review C 57 (1998) 3185
- [Dem96] Code to calculate multistep cross-sections for ($p, ^3\text{He}$)
P Demetriou
Private communication
- [Dim96] Tables and code for the calculation of multistep cross-sections for ($p, ^3\text{He}$)
S S Dimitrova
Private communication
- [Eng74] Techniques in Nuclear Structure Physics
J B A England
John Wiley & Sons (1974)
- [Fes80] The statistical theory of multi-step compound and direct reactions
H Feshbach, A Kerman and S Koonin
Annals of Physics 125, 429 (1980)

- [För91] Continuum protons from $^{58}\text{Ni}(p,p')$ at incident energies between of 100 and 200 MeV
S V Förtsch, A A Cowley, J J Lawrie, D M Whittal, J V Pilcher and F D Smit
Physical Review C 43 (1991) 239
- [För92] Proton emission in pre-equilibrium reactions induced by incident protons of 100 and 200 MeV
S V Förtsch
PhD Thesis (1992)
University of Pretoria
- [Gle65] Nuclear spectroscopy with two-nucleon transfer reactions
N K Glendenning
Physical Review 137 (1965) B102
- [Gle83] Direct nuclear reactions
N K Glendenning
Academic Press (1983)
- [Hae74] Polarization experiments; Polarized Beams,
edited by J Cerny (California 1974), p151
W Haeberli
Nuclear spectroscopy and reactions (Part A)
- [Hil90] Nuclear reactions with polarized spin- $\frac{1}{2}$ beams
G C Hillhouse
MSc Thesis (1990)
Stellenbosch University
- [Hod97] Introductory Nuclear Physics
P E Hodgson, E Gadioli, E Gadioli Erba
Oxford Science Publication (1997)

- [Hub61] Proceedings of the First International Symposium on Polarization Phenomena of Nucleons, Basal (1960)
P Huber and K P Meyer (1961)
- [Jac05] Proton reaction cross sections on ^{12}C , ^{40}Ca , ^{90}Zr and ^{208}Pb at energies between 80 and 180 MeV
N M Jacobs
PhD Thesis (2005)
Stellenbosch University
- [Kat98] Microscopic Optical Potential for $^3\text{He} + A$ by Double Folding model
M Katsuma and Y Sakuragi
Private communication
- [Kun93] DWUCK4
P D Kunz and R Rost
Computational Nuclear Physics
Edition K Langanke *et al.* (Berlin: Springer) p88 (1993)
- [Kal88] Systematics of continuum angular distributions: Extensions to higher energies
C Kalbach
Physical Review C 37 (1988) 2350
- [Kno89] Radiation Detection and Measurement
G L Knoll
John Wiley & Sons (1989)
- [Kra88] Introductory Nuclear Physics
K S Krane
John Wiley & Sons (1988)

- [Kob82] Folding model analysis of α -particle elastic scattering with a semirealistic density-dependent effective interaction
A M Kobos, B A Brown, P E Hodgson, G R Satchler and A Budzanowski
Nuclear Physics A384 (1982) 65
- [Kob84] Folding model analysis of elastic and inelastic α -particle scattering using a density-dependant force
A M Kobos, B A Brown, R Lindsay and G R Satchler
Nuclear Physics A425 (1984) 205
- [Kon93] Computational comparison of quantum-mechanical models for multistep direct reactions
A J Koning and J M Akkermans
Physical Review C 47 (1993) 724
- [LAB05] Layout of the cyclotron facility at iThemba LABS
Available at website
<http://www.tlabs.ac.za/public/default.htm>
- [Leo94] Techniques for Nuclear and Particle Physics Experiments
W R Leo
Springer Verlag (1994)
- [Lew82] Analyzing power in the continuum of the $(\bar{p}, \alpha x)$ and $(\bar{p}, \tau x)$ reactions on ^{12}C , ^{27}Al , ^{58}Ni , ^{90}Zr , ^{209}Bi at $E_p = 72$ MeV
Z Lewandowski, E Loeffler, R Wagner, H H Meuller, W Reichart and P Schober
Nuclear Physics A389 (1982) 247

- [Mad88] Recent Results in the Development of a Global Medium-Energy Nucleon-Nucleus Optical-Model Potential
D G Madland
Proceedings of a Specialists' Meeting on Pre-equilibrium Reactions, Semmering, Austria, 1988 edited by B Strohmaier (OECD, Paris, 1988) p103
International Atomic Energy Agency
Report No. IAEA-TECDOC-483 (1988) p80 (Unpublished)
- [May92] Kernphysik
T Mayer-Kuckuk
B G Teubner Stuttgart (1992)
- [Mea69] Loss of charged particles by nuclear interactions in scintillators
D F Measday and R J Schneider
Nuclear Instruments and Methods 42 (1966) 26
- [Mey83] Proton scattering from ^{12}C between 120 and 200 MeV and the optical potential
H O Meyer, P Schwandt, W W Jacobs and J R Hall
Physical Review C 27 (1983) 459
- [Nan74] $(p, ^3\text{He})$ and (p, t) reactions on ^{29}Si
H Nann, W Benenson, W A Lanford and B H Wildenthal
Physical Review C10 (1974) 1001
- [Nev98] A Study of $^{208}\text{Pb}(p, 2p)^{207}\text{Tl}$ Reaction with a Magnetic Spectrometer at an Incident Energy of 200MeV
R Neveling
MSc Thesis (1998)
University of Stellenbosch

- [Nev01] Nuclear medium effects on analyzing power investigated with a proton knockout reaction
R Neveling
PhD Thesis (2001)
University of Stellenbosch
- [Nis88] Statistical theory of precompound reactions: The multistep direct process
H Nishioka, H A Weidenmüller and S Yoshida
Annals of Physics 183, 166 (1988)
- [Pea86] Nuclear Physics
J M Pearson
Adam Hilger Ltd (1986)
- [Pil89] Coincident Proton Decay of Continuum Induced by 200 MeV Protons on ^{12}C
J V Pilcher
PhD Thesis (1989)
University of Cape Town
- [Pil96] The NAC MBD to VME Conversion Guide
J V Pilcher
National Accelerator Center (1996) (Unpublished)
- [Ren91] Analyzing powers and isotope ratios for the
 $^{\text{nat}}\text{Ag}(\bar{p}, \text{intermediate-mass fragment})$ reaction at 200 MeV
E Renshaw, S J Yennello, K Kwiatkowski, R Planeta, L W Woo and
V E Viola
Physical Review C 44 (1991) 2618

- [Ric92] Statistical multistep direct calculations for (p,p') continuum spectra up to 200 MeV
W A Richter, A A Cowley, R Lindsay, J J Lawrie, S V Förtsch, J V Pilcher, R Bonetti and P E Hodgson
Physical Review C 46 (1992) 1030
- [Ric94] Preequilibrium (p,p') measurements and calculations for ^{90}Zr and neighboring nuclei for incident energies up to 200 MeV
W A Richter, A A Cowley, G C Hillhouse, J A Stander, J W Koen, S W Steyn, R Lindsay, R E Julies, J J Lawrie, J V Pilcher and P E Hodgson
Physical Review C 49 (1994) 1001
- [Ric96] Inclusive (p,p') reactions on nuclei in the mass range 115 to 181 at incident energies from 120 to 200 MeV
W A Richter, S W Steyn, A A Cowley, J A Stander, J W Koen, R Lindsay, G C Hillhouse, R E Julies, J J Lawrie, J V Pilcher, and P E Hodgson
Physical Review C 54 (1996) 1756
- [Sak80] Analyzing powers of the continuum spectra: 65 MeV polarized protons on ^{12}C , ^{28}Si , ^{45}Sc , ^{58}Ni , ^{93}Nb , ^{165}Ho , ^{166}Er and ^{209}Bi
H Sakai, K Hosono, N Matsuoka, S Nagamachi, K Okada, K Maeda and H Shimizu
Nuclear Physics A344 (1980) 41
- [Sak98] Spin-orbit interactions of ^3He -nucleon scattering at intermediate energies
Y Sakuragi and M Katsuma
Nuclear Instruments and Methods in Physics Research 402 (1998) 347
- [Sat79] Folding model potentials from realistic interactions for heavy-ion scattering
G R Satchler and W G Love
Physics Reports 55 (1979) 207
North-Holland Publishing Company – Amsterdam (1979)

- [Sat83] Direct nuclear reactions
G R Satchler
Oxford University Press (1983)
- [Sch82] Analyzing power of proton-nucleus elastic scattering between 80 and 180 MeV
P. Schwandt, H.O. Meyer, W.W. Jacobs, A.D. Bacher, S.E. Vigdor, M.D. Kaitchuck and T.R. Donoghue
Physical Review C 26 (1982) 55
- [Seg82] Inclusive proton reactions at 164 MeV
R E Segel, T Chen, L L Rutledge (Jr), J V Maher, J Wiggins, P P Singh and P T Dedevec
Physical Review C 26 (1982) 2424
- [Sen83] Structure information on ^{38}K obtained from a microscopic and macroscopic DWBA analysis of the $^{40}\text{Ca}(p, ^3\text{He})^{38}\text{K}$ reaction.
J C Sens and R J Meijer
Nuclear Physics A 407 (1983) 45
- [Spa00] The analysing power ($p, ^3\text{He}$) reactions
K Spasova, S S Dimitrova, P E Hodgson
Journal of Physics G: Nuclear 26 (2000) 1489
- [Ste97] Multistep direct reactions in nuclei
S W Steyn
PhD Thesis (1997)
Stellenbosch University
- [Sto04] Private Communication
From M V Stoitsov via S S Dimitrova
Institute of Nuclear Research and Nuclear Energy
Bulgarian Academy of Sciences (2004)

- [Tam82] Multistep direct reaction analysis of continuum spectra in reactions induced by light ions
T Tamura, T Udagawa and H Lenske
Physical Review C 26 (1982) 379
- [Wal86] A Global Optical Model for Neutron Scattering for $A > 53$ and $10 \text{ MeV} < E < 80 \text{ MeV}$
Proceedings of the International Conference on Nuclear Data of Basic and Applied Science, Santa Fe, N.M. 1985
R L Walter and P P Guss
Gordon and Breach Science Publications, Inc. New York (1986) p1079
- [Whi89] Quasifree Knockout of Charged Particles from ^4He with 100 MeV Protons
D M Whittal
PhD Thesis (1989)
University of Cape Town
- [Whi90] Quasifree knockout of charged particles from ^4He with 100 MeV Protons
D M Whittal, A A Cowley, J V Pilcher, S V Förtsch, F D Smit and J J Lawrie
Physical Review C 42 (1990) 309
- [Yod94] IUCF VME Data Acquisition System User Information
N R Yoder
Indiana University Cyclotron Facility (1994) (Unpublished)